Resul ÖZDEMİR

DESIGN, SYNTHESIS, AND CHARACTERIZATION OF *N*-TYPE AND AMBIPOLAR SMALL MOLECULAR SEMICONDUCTROS

AGU 2016

DESIGN, SYNTHESIS, AND CHARACTERIZATION OF *N*-TYPE AND AMBIPOLAR SMALL MOLECULES AS AIR-STABLE AND SOLUTION-PROCESSABLE SEMICONDUCTORS IN OFETs

A Master's Thesis

By
Resul ÖZDEMİR
December 2016

ABDULLAH GÜL
UNIVERSITY

DESIGN, SYNTHESIS, AND CHARACTERIZATION OF *N*-TYPE AND AMBIPOLAR SMALL MOLECULES AS AIR-STABLE AND SOLUTION-PROCESSABLE SEMICONDUCTORS IN OFETs

A THESIS
SUBMITTED TO THE DEPARTMENT OF ADVANCED MATERIALS AND NANOTECHNOLOGY AND THE GRADUATE SCHOOL OF ENGINEERING AND SCIENCES OF ABDULLAH GÜL UNIVERSITY
IN PARTIAL FULFILLMENT OF THE REQUIREMENTS
FOR THE DEGREE OF
MASTER OF SCIENCE

By
Resul ÖZDEMİR
December 2016

SCIENTIFIC ETHICS COMPLIANCE

I hereby declare that all information in this document has been obtained in accordance with academic rules and ethical conduct. I also declare that, as required by these rules and conduct, I have fully cited and referenced all materials and results that are not original to this work.

Resul ÖZDEMİR

REGULATORY COMPLIANCE

M.Sc. thesis titled "Design, Synthesis, and Characterization of *N*-Type and Ambipolar Small Molecules as Air-Stable and Solution-Processable Semiconductors in OFETs" has been prepared in accordance with the Thesis Writing Guidelines of the Abdullah Gül University, Graduate School of Engineering and Science.

Prepared By	Advisor
Resul ÖZDEMİR	Assoc. Prof. Hakan USTA

Head of the Advanced Materials and Nanotechnology Program
Assoc. Prof. Murat DURANDURDU

ACCEPTANCE AND APPROVAL

M.Sc. thesis titled “Design, Synthesis, and Characterization of *N*-Type and Ambipolar Small Molecules as Air-Stable and Solution-Processable Semiconductors in OFETs” was prepared by Resul ÖZDEMİR, which has been accepted by the jury in the Advanced Materials and Nanotechnology Graduate Program at Abdullah Gül University, Graduate School of Engineering and Science.

28/12/2016

JURY:

Advisor : Assoc. Prof. Hakan USTA

Member : Assist. Prof. Evren MUTLUGÜN

Member : Assoc. Prof. M. Serdar ÖNSES

APPROVAL:

The acceptance of this M.Sc. thesis has been approved by the decision of the Abdullah Gül University, Graduate School of Engineering and Science, Executive Board dated ….. /….. / ……….. and numbered ………….…….. .

Graduate School Dean
Prof. İrfan ALAN

ABSTRACT

DESIGN, SYNTHESIS, AND CHARACTERIZATION OF *N*-TYPE AND AMBIPOLAR SMALL MOLECULES AS AIR-STABLE AND SOLUTION-PROCESSABLE SEMICONDUCTORS IN OFETs

Resul ÖZDEMİR
M.Sc. in Advanced Materials and Nanotechnology
Supervisor: Assoc. Prof. Hakan USTA

December 2016

The design and development of novel ambipolar and n-channel semiconductors is very crucial to advance various optoelectronic technologies including organic field-effect transistors (OFETs) and complementary (CMOS) integrated circuits. Although numerous ambipolar and n-channel polymers have been realized to date, small molecules have been unable to provide high device performance in combination with ambient-stability and solution-processibility.

In the first part of this thesis, two novel small molecules, 2OD-TTIFDK and 2OD-TTIFDM, were designed, synthesized and characterized in order to achieve ultralow band-gap (1.21-1.65 eV) semiconductors with sufficiently balanced molecular energetics for ambipolarity. Bottom-gate/top-contact OFETs fabricated via solution-shearing of 2OD-TTIFDM yield perfectly ambient stable ambipolar devices with reasonably balanced electron and hole mobilities of 0.13 $cm^2/V\cdot s$ and 0.01 $cm^2/V\cdot s$, respectively with I_{on}/I_{off} ratios of ~10^3-10^4, and 2OD-TTIFDK-based OFETs exhibit ambipolarity under vacuum with highly balanced ($\mu e/\mu h \sim 2$) electron and hole mobilities of 0.02 $cm^2/V\cdot s$ and 0.01 $cm^2/V\cdot s$, respectively with I_{on}/I_{off} ratios of ~10^5-10^6. Furthermore, complementary-like inverter circuits were demonstrated with the current ambipolar semiconductors resulting in high voltage gains of up to 80. Our findings clearly indicate that ambient-stability of ambipolar semiconductors is a function of molecular orbital energetics without being directly related to bulk π-backbone structure. To the best of our knowledge, considering the processing, charge-transport and inverter characteristics, the current semiconductors stand out among the best performing ambipolar small molecules in the OFET and CMOS-like circuit literature. Our results provide an efficient approach in designing ultralow band-gap ambipolar small molecules with good solution-processibility and ambient-stability for various optoelectronic technologies including CMOS-like integrated circuits.

In the second part of this thesis, a new solution-processable and air-stable liquid-crystalline n-channel organic semiconductor (α,ω-2OD-TIFDMT) was designed, synthesized, and characterized. The new semiconductor exhibits a low LUMO energy level (-4.19 eV) and a narrow optical band gap (1.35 eV). Typical pseudo focal-conic fan-shaped texture of a hexagonal columnar liquid crystalline (LC) phase was observed over a wide temperature range from melting point at 139 °C to isotropic transition point at 232 °C. The semiconductor thin-films prepared by spin-coating α,ω-2OD-TIFDMT shows the formation of large (~0.5-1 μm sizes) and highly crystalline plate-like grains with good interconnectivity. The molecules were found to adopt edge-on orientation on the dielectric surface resulting in favorable charge-transporting networks of π-π stacking along the dielectric-semiconductor interface. Top-contact/bottom-gate organic field-effect transistors fabricated by using the spin-coated semiconductor films, which were annealed at a low temperature ($T_{annealing}$ = 50 °C), have yielded good electron mobilities as high as 0.11 $cm^2/V \cdot s$ and high I_{on}/I_{off} ratios of 10^7-10^8 with excellent ambient stability. This indicates two orders of magnitude (100×) enhancement in OFET mobility when compared with a low-temperature annealed well-known semiconductor, β-DD-TIFDMT. Side-chain engineering in the new semiconductor structure offers great advantage for the D-A-D π-core co-planarity while maintaining a good solubility in organic solvents, and leads to favorable optoelectronic and physicochemical characteristics for better OFET performance. Thermal annealing at LC phase results in significant deterioration in charge-transport with much lower (10,000×) electron mobility. These remarkable findings demonstrate that this new small molecule is a promising semiconductor material for the development of *n*-channel OFETs on flexible plastic substrates and LC-state annealing in columnar liquid crystals can be deteriorating for transistor-type charge transport.

Keywords: Solution-Processable, Air-Stable, Ambipolar, N-channel, Organic Semiconductor

ÖZET

OFET'LER İÇİN HAVADA KARARLI VE ÇÖZÜCÜDE İŞLENEBİLEN *N*-TİPİ VE AMBİPOLAR KÜÇÜK MOLEKÜLLERİN DİZAYNI, SENTEZİ VE KARAKTERİZASYONU

Resul ÖZDEMİR
İleri Malzemeler ve Nanoteknoloji Anabilim Dalı Yüksek Lisans
Tez Yöneticisi: Doç. Dr. Hakan USTA

Aralık 2016

Yeni ambipolar ve n-tipi yarı iletkenlerin dizaynı ve geliştirilmesi organik alan etkili transistörler (OFETs) ve bütünleyici entegre devreler (CMOS) gibi farklı ileri optoelektronik teknolojiler için son derece önemlidir. Bugüne kadar literatürde çok sayıda ambipolar ve n-tipi polimerik yarı iletken ile karşılaşılmasına rağmen, havada kararlılık ve çözücüden proses edilebilme özelliklerine sahip yüksek cihaz performansı gösterebilen küçük moleküllere rastlanmamıştır.

Bu tezin ilk bölümünde, ambipolarlık için yeterli moleküler enerji seviyelerine sahip, çok düşük band aralıklı (1.21-1.65 eV) iki yeni küçük molekül (2OD-TTIFDK ve 2OD-TTIFDM) tasarlanmış, sentezlenmiş ve yapıları aydınlatılmıştır. 2OD-TTIFDM molekülü kullanılarak çözücüden kesme (solution-shearing) yöntemi ile üretilen alt kapı üst temas organik alan etkili transistör, 0.13 $cm^2/V{\cdot}s$ elektron, 0.01 $cm^2/V{\cdot}s$ boşluk (hole) hareketliliği ve ~10^3-10^4 I_{on}/I_{off} oranı ile havada son derece kararlı ambipolar cihaz performansı ortaya koymuştur. Diğer taraftan 2OD-TTIFDK molekülü tabanlı OFET ise, vakum altında 0.02 $cm^2/V{\cdot}s$ elektron ve 0.01 $cm^2/V{\cdot}s$ boşluk hareketliliği ile son derece dengeli ($\mu e/\mu h \sim 2$) ambipolarite ve ~10^5-10^6 I_{on}/I_{off} oranı sergilemiştir. Ayrıca söz konusu yarı iletkenler kullanılarak 80V a kadar yüksek gerilim kazancı gösteren bütünleyici dönüştürücülere benzer devreler (CMOS-like inverter circuit) üretilmiştir. Elde edilen sonuçlarla, ambipolar yarı iletkenlerin havada kararlılığının hacimsel π-omurga yapısından çok moleküler orbital enerji seviyelerine bağlı olduğu ortaya çıkarılmıştır. Bu malzemeler, yük taşıma, dönüştürücü özellikleri ve proses açısından bakıldığında literatürde yer alan en iyi performansa sahip ambipolar yarı iletkenler arasında kendine yer bulmaktadır. Bu sonuçlar, çözücüde proses edilebilen ve havada kararlılık gösteren çok düşük band aralıklı ambipolar küçük moleküllerin farklı optoelektronik uygulamalar için tasarlanması konusunda büyük önem arz etmektedir.

Bu tezin ikinci bölümünde ise, çözücüde proses edilebilen havada kararlı sıvı kristal yeni *n*-tipi organik yarı iletken (α,ω-2OD-TIFDMT) tasarlanmış, sentezlenmiş ve yapısı aydınlatılmıştır. Yeni yarı iletkenin düşük LUMO enerji seviyesine (-4.19 eV) ve dar optik band aralığına (1.35 eV) sahiptir. 139 °C ile 232 °C (izotropik erime noktası) arasındaki geniş sıcaklık bölgesinde tipik yelpaze şeklinde yapıya sahip hegzagonal sıvı kristal faz gözlemlenmiştir. Yarı iletken ince-film, döndürme kaplama yöntemi ile elde edilmiştir. Bu filmlerde, birbirleriyle yüksek derecede bağlantılı, büyük boyutlu (~0.5-1 μm) plaka formunda kristaller gözlemlenmiştir. Dielektrik yüzeyde molekülün kenarı üzerinde (edge-on) yönelme göstermesinin, dielektrik yarı iletken ara yüzü boyunca yük taşınımına olumlu yansıdığı tespit edilmiştir. Söz konusu yarı-iletkenden döndürme kaplama yöntemi ve düşük sıcaklıklarda tavlama ($T_{annealing}$ = 50 °C) ile alt kapı üst temas organik alan etkili transistör üretilmiştir. Havada son derece kararlı olan bu cihaz ile maksimum 0.11 $cm^2/V{\cdot}s$ elektron hareketliliği, 10^7-10^8 I_{on}/I_{off} oranı elde edilmiştir. Bu durum, yüksek sıcaklık da tavlanan β-DD-TIFDMT yarı iletkeni ile kıyaslandığında OFET yük hareketliliğinin 100 kat arttığını göstermektedir. Yeni yarı iletkendeki alkil zincirlerinin pozisyonu ve dallanmış olması, D-A-D π-merkezin düzlemselliğine müthiş katkı yaparken organik çözücülerdeki çözünürlüğü korumuştur. Bu sayede daha iyi OFET performansı sergilenmesi için uygun optoelektronik ve fizikokimyasal özellikler yapıya kazandırılmıştır. Sıvı kristal fazda yapılan tavlama sonrası, elektron hareketliliğinin 10000 kat azaldığı tespit edilmiştir. Bu sonuçlar, yeni n-tipi küçük yarı iletken molekülün, esnek plastik altlıklar ile OFET uygulamalarında kullanımının umut vadettiğini göstermektedir.

Anahtar kelimeler: Çözücüde Proses Edilebilen, Havada Kararlı, Ambipolar, N-tipi, Organik Yarı İletken, Organik Alan Etkili Transistörler (OFETs)

Acknowledgements

At first, I would like to express my deepest appreciation to my advisor, Assoc. Prof. Hakan Usta. His support and encouragement gave me strength and assurance. Prof. Usta's assiduousness, deep knowledge, and enthusiasm for science has had such an intense impact on me and my career. My research would not have been possible without his guidance and efforts.

I am also appreciated to my lab-mate Mehmet Özdemir for his support and gentleness during my research.

I would like to acknowledge that this study was supported by Research Fund of Abdullah Gül University (AGU-BAP), Project No: FYL-2016-65, Turkish Academy of Sciences, The Young Scientists Award Program (TUBA-GEBIP 2015) and The Science Academy, Young Scientist Award Program (BAGEP 2014).

Finally, I would like to thank my family with my all heart; my precious parents Osman and Fatma, my dear brothers İsa, İbrahim and Bilal. I am also grateful to my wife, Fundagül for her endless love, patience and infinite supports for every step in my life. Thanks to my lovely baby girl, Zeynep Serra. You make my life colorful and your smiling face give me strong motivation and joie de vivre.

Table of Contents

List of Figures

List of Tables

Chapter 1

Introduction

1.1 Organic Thin-Film Transistors

Conventional inorganic semiconductors such as Si, Ge, and GaAs have been widely used in the fabrication of field-effect transistors (FETs); especially in metal-oxide-semiconductor field-effect transistors (MOSFETs). Si based materials have become the main character of today's semiconducting devices. Specifically, FET is one of the crucial components of modern microelectronics technology thanks to its extensive usage in computers and communication technologies. However heat sensitive materials including plastics substrates could not be used in the manufacturing of FETs due to high temperature requirement of the processes.[1] At this point, organic thin film transistors (OTFTs) stepped in as a new player of semiconductor based devices. OFET fabrication processes are based deposition of multilayers including dielectric and semiconducting layers. Hydrogen ended α–Si is the most common semiconductor which has been used in the LCD technology due to its compatibility with different substances. However, α–Si is not suitable for the fabrication of flexible electronics on plastic substrates.

Organic field-effect transistors (OFETs) have drawn scientists' attention owing to their unique optoelectronical and physical properties. This new field was promising to combine plastics with efficient electro-active materials which enable the production of low-cost, light-weight, and flexible displays.[2] Hence, OFETs have already find place in a broad range of applications including logic circuits, displays, sensors and RFIDs. Charge carrier mobility is one of the crucial parameter in the OFET devices, as well as in organic light emitting transistors (OLETs) and organic photovoltaics (OPVs).[3] Thus

OFET study is expressive for both practical applications and further understanding of the charge carrier transport mechanism.

Figure 1.1.1 Examples of organic semiconductor based prototype.[4–6]

OFET is a three electrodes device based on source (S), drain (D) and gate (Figure 1.2). The direction of charge carrier movement in the semiconducting layer is parallel to substrate surface from source to the drain. Therefore, the relation between three electrodes is that the gate controls the charge carrier density through the channel. When there is no gate voltage, no charge carrier transport occurs through channel, and no current is observed between source and drain. By applying a voltage on the gate electrode, due to polarization in the dielectric layer, we can induce charge carriers in the semiconducting layer (Figure 1.2) OFET devices can be categorized based on the charge carrier type as *p*-channel (hole-conducting), *n*-channel (electron-conducting) and ambipolar. When positive and negative voltages are applied into an ambipolar device, both holes and electrons can be induced simultaneously through the channel.

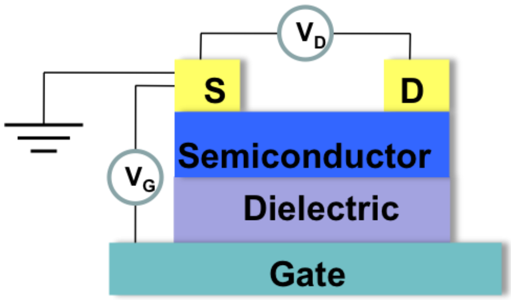

Figure 1.1.2 Schematic diagram of an OFET device structure.

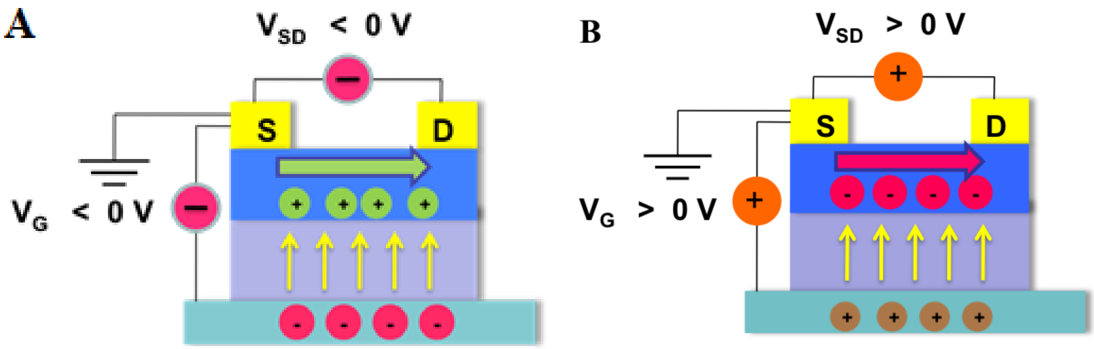

Figure 1.1.3 Schematic diagram of *p*-channel OFET (a) and *n*-channel OFET (b).

Three figure of merits in the OFET devices are charge carrier mobility (μ), current on/off ratio (I_{ON}/I_{OFF}), and threshold voltage (V_T). OFET electrical characteristics such as charge carrier mobilities (μ) and threshold voltages (V_T) can be extracted from the saturation region, by using the following equation:

$$\mu_{sat} = (2I_{DS}L)/[WC_i(V_G - V_T)^2]$$

where I_{DS} is the drain current, L and W are the channel length and width, respectively, C_i is the areal capacitance of the gate dielectric, V_G is the gate voltage, and V_T is the threshold voltage.

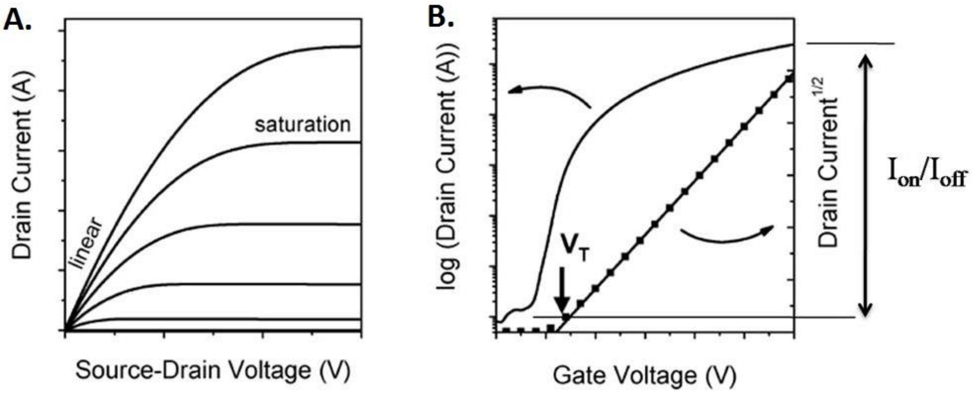

Figure 1.1.4 Typical OFET transfer (a) and output (b) curve.

Organic materials which will be used in plastic electronics must possess two crucial properties. The first one is π-conjugation along whole molecular or polymeric backbone. The extension of π-conjugation directly affects the optoelectronical properties. The second one is solubility, organic materials might be a good candidate for large area displays thanks to their processability in organic solvents via ink-jet printing, spin coating, etc. There are several advantages of using π-conjugated small molecules instead of polymers, which are enhanced solubility, higher crystallinity, better synthetic reproducibility, and higher degree of purity. [7–10] In contrast, when compared with molecular π-conjugated systems, polymers offer special properties as enhanced mechanical and thermal stability.

Nobel Prize in Chemistry 2000 was given to three scientists due to their great achievements in the field of conductive polymers.[11] Twelve orders of magnitude increase in the conductivity was achieved via oxidative doping with iodine.[12] Doped polyacetylene showed electrical conductivity 10^5 Sm^{-1}, but it was very sensitive against oxygen and the polymer was insoluble in organic solvents. So, new semiconductors such as polythiophene (PT) and polyphenylenevinylene (PPV) has revealed better performances for real applications.[13]

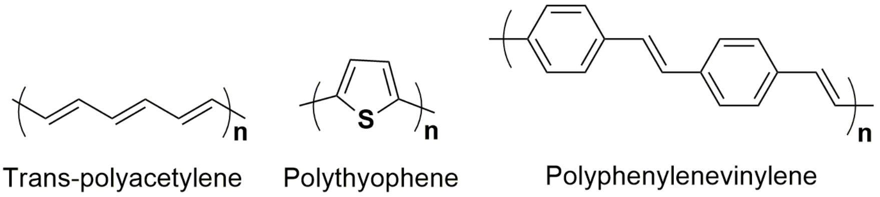

Figure 1.1.5 Chemical structures of three conjugated polymers.

There are two figures of merits for conjugated systems. The first one is the existence of "conjugated double bonds" through the backbone. The second one is mobility; charge carriers (electrons and holes) must move along with the molecular structures to enhance conductivity.

Conjugated double bond comprises a σ-bond and a π-bond. σ-bond is a very strong covalent bond. Carbon atoms share electrons which are based on atomic the s orbitals. Therefore, electrons in the σ-bond are strongly attached to nuclei and they are highly localized. On the other hand, π-bond is relatively weaker due to specific band geometry. Normally π-bond electrons tent to be localized, but in conjugated systems thanks to overlapping between neighboring π-bonds electrons are highly delocalized. Therefore, charge carrier transport can be achieved via continuous overlapping of π-orbitals.[13]

The alternation of single and double bonds enables the separation of bonding and anti-bonding states which forms energy gap between these states. The highest occupied molecular orbital (HOMO) is equivalent to valance band, and the lowest unoccupied molecular orbital (LUMO) is equivalent to the conduction band in inorganic semiconductors. The band gap energy between HOMO and LUMO levels is related to the length of the π-conjugation.

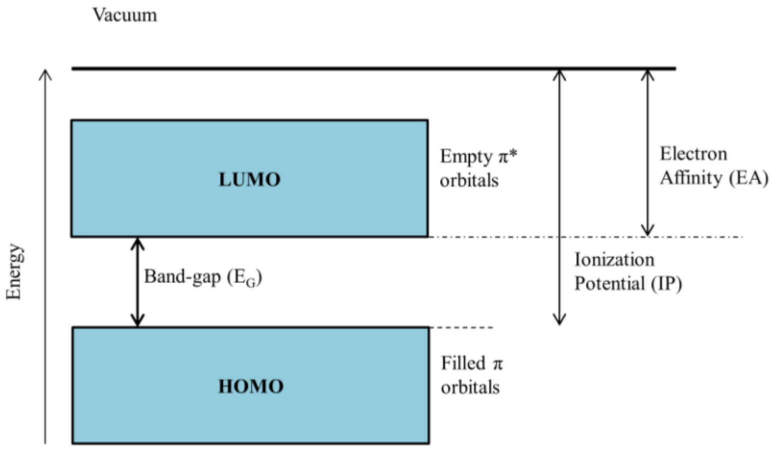

Figure 1.1.6 Organic semiconductors' energy band diagram.

Organic materials are known as insulators because of their initial neutral state and wide band gap energy. To cope with this problem, oxidation and reduction reactions are used to achieve *p*-channel (hole conducting), and *n*-channel (electron conducting) operation. These charge carriers move through conjugated backbone in an electric field. Most of the organic-based materials in the literature are *p*-channel polymers.

Organic based conjugated systems can be used as semiconductors due to strong π-π overlap. When extra charge is added on the system, this charge will become delocalized among the whole molecule/polymer. In semiconductors, injected charges act as carriers. This type of devices is called as "*organic thin film transistors"*.

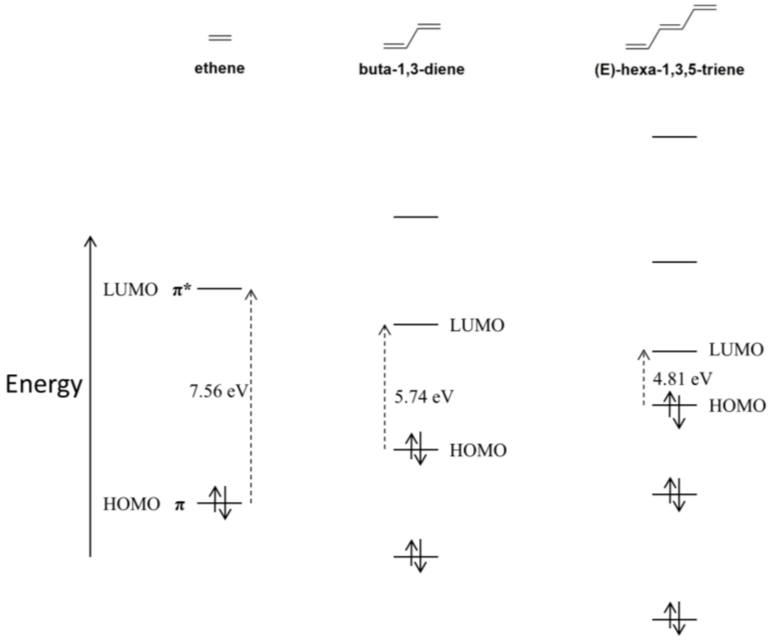

Figure 1.1.7 Relation between conjugation length and band gap energy.

Charge transport in organic based materials depends on π-orbital overlapping through conjugated backbone. However, in some certain cases including amorphous polymeric materials charge carrier mobility can be poor because of weak π-π interactions. In general, polymers contain polycrystalline phases, this disorder tends to hinder the charge carrier mobility. Typical charge carrier mechanism is explained as a thermally activated tunneling of charge carriers, which is also known as ''*hopping*''.[14,15] Charge carrier hopping takes place between the localized states. The reason behind the low charge mobility in organic semiconductors originates from poor crystallinity and morphology. In crystalline inorganic based materials, charge transport is restricted by phonon scattering.[14] In additional, the charge carrier mobility of crystalline inorganic based materials decrease with temperature. But temperature and charge carrier mobility has a reverse relationship in organic based materials.[14] There is a linkage between crystallinity and mobility. Highly ordered molecular crystals can achieve mobilities over 1 $\mathrm{cm^2\ V^{-1}\ s^{-1}}$, which is considered as a starting point of good OFET performance. In high electric field, the charge carrier mobility of organic semiconductors becomes field-dependent.[14] Gate voltage dependent mobility is often detected in organic based materials. This dependence is due to the fact that as the gate voltage increases, injected charge-carriers are in tendency to fill the traps, consequently trapping becomes less efficient and charge transport increases. Surprisingly, as the quality of OTFT devices increases, gate bias dependence and thermally activated mobility tend to be less met.[16] The charge transport and mobility in organic semiconductors are also limited by macroscopic features such as poor contacts between different crystalline domains or disorder in the material.[17] Hence, molecular ordering and alignment of the conjugated units in the solid state play crucial roles in achieving efficient charge transport.

1.1.1 Microstructure and Molecular Alignment

Organic semiconductor thin films comprise a mixture of polycrystalline and amorphous phases. So, hopping charge transportation mechanism does not work very well between these two phases due to limited charge carrier mobility. Therefore proper packing in the solid state is crucial to achieve efficient charge transport.[17] Organic molecules are likely to exhibit low self-organization because of their weak intermolecular interactions of Van der Waals and London forces. Hence, molecular engineering comes into prominence in achieving well-packed and well-ordered thin films in the solid state.[13]

The characterization of organic thin films can be performed via X-ray diffraction (XRD) and atomic force microscope (AFM). Molecular parameters such as π-π stacking structures and interlayer distances (intermolecular spacing along the lamellar π-π stacking direction) might be obtained by using these techniques.

Additionally, alignment of small molecules or polymer chains has important effect on transistor device performance. Based on process conditions and dielectric surface properties, poly(3-hexylthiophene) demonstrates two different type of orientations.[18] In edge-on orientation, π-π stacking alignment is parallel to the charge carrier movement direction. But, in face-on orientation π-π stacking alignment is perpendicular to the charge carrier movement direction. Mobility dramatically changed by more than 100 times by changing the molecular orientation from face-on to edge-on.

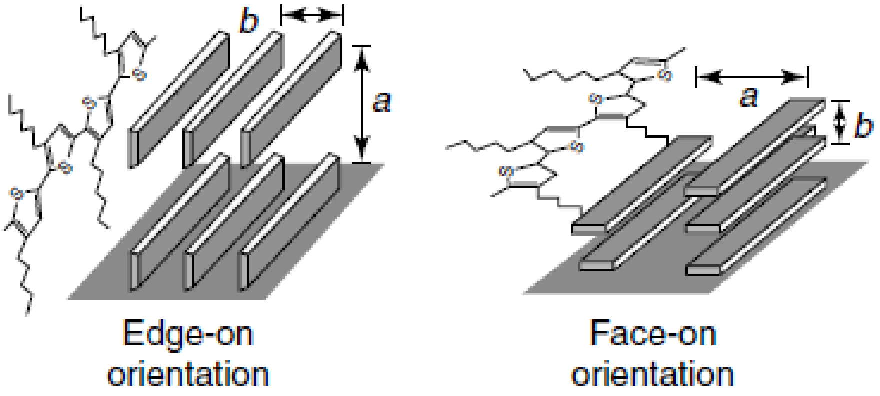

Figure 1.1.1.1 Edge-on and face-on orientations of ordered P3HT domains according to the FET substrate.[18]

Dielectric surface modification is one of the most important steps in OTFT device fabrication process. Prior to organic semiconductor deposition, functionalization of the dielectric surface is crucial to achieve high device performance. Dielectric surface conditions have great impact on electrical properties of OFET device.[13]

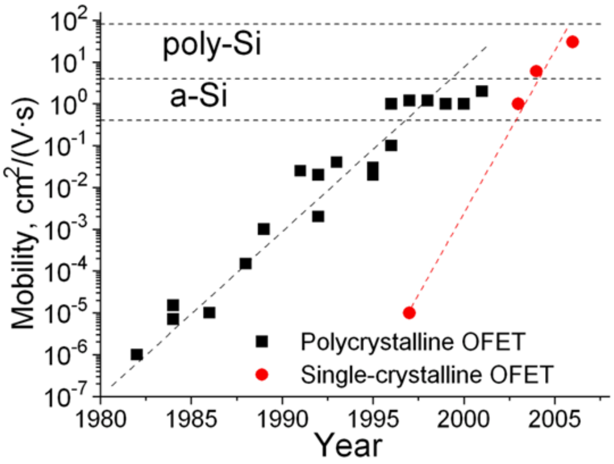

Figure 1.1.1.2 Progress in the performance of organic semiconductor.[16]

1.1.2 Material Development and Classification

1.1.2.1 Polymeric and Small-Molecule *p*-Channel Semiconductors for OFETs

By the invention of polythiophene (PT) in 1986, thiophene based materials become the most studied molecule/polymer for organic optoelectronic applications. [19] PT exhibited very low mobility (≈10^{-5} cm^2/Vs) and poor π-π stacking in the solid state. Therefore many scientists worked on to improve new π-conjugated building blocks with good mobility (≈ 1 cm^2/Vs) and thin-film quality.

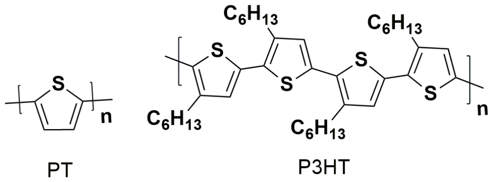

Figure 1.1.2.1.1 Chemical structures of polythiophene and poly(3 hexylthiophene).

The presence of 3-substituents considerably increase the solubility and the thin-film quality, regioregular poly(3-hexylthiophene) (P3HT) with edge-on packing has demonstrated hole mobility of up to 0.1 cm^2/Vs.[18]

Recently, different types of molecular and polymeric semiconductors have been developed apart from PT and P3HT. Takimiya *et al*. reported P1 which is based on [1]Benzothieno[3,2-b][1]benzothiophene(BTBT)-thiophene copolymer (PBTBT).[20] Highly twisted backbone hindered the TFT performance, further studies approved that BTBT shows better outputs in the small molecule systems.

Isoindigo based molecules have been widely used in semiconductor design due to its strong electron-withdrawing character. Pei *et al*. developed a novel semiconducting polymer P2 with high hole mobility of 3.62 cm^2/Vs.[21] Alkyl side chain molecular engineering effects the solubility, but its effects on charge carriers mobility has been discovered by this study.

Diketopyrrolopyrrole (DPP) based semiconductors exhibit high charge-carrier mobility, mostly around 1 cm^2/Vs. The first DPP based polymer was reported in 2008.[22] In a recent study by Wudl *et al.*, new polymer P3 exhibited high mobility (2.5 cm^2/Vs) thanks to short π-π stacking of 3.5Å in the solid state which causes π conjugation extension and highly ordered crystals.[23] Thieno[3,4-c]pyrrole-4,6-dione (TPD) based copolymers synthesized by Li et al.[24] In this study, highest reported mobility (1.29 cm^2/Vs) achieved for TPD based semiconductors due to alkyl substituent crucial position on the π-backbone. The orientation of alkyl substituent directly affects the packing pattern, thin film morphology and OFET device performance, which provoke to raise charge-carrier mobilities.

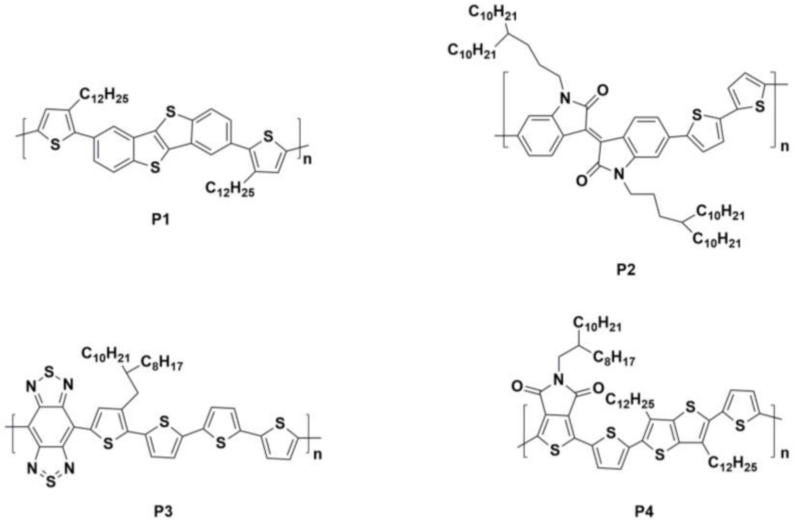

Figure 1.1.2.1.2 Chemical structures of *p*-channel polymeric semiconductors.

Oligothiophene-based small molecules for optoelectronic application have been widely studied. Four (α4T, M1), five (α5T), six (α6T, M2) and eight (α8T) thiophene rings have been extensively investigated in OFETs. [25,26]

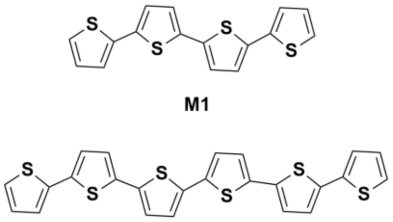

M1

M2

Figure 1.1.2.1.3 Chemical structures of small molecular oligothiophenes.

Recently, heteroacene-based novel small molecular semiconductors have been developed for OFET application. The architecture of these systems are basically like a ladder and consist of one or more benzene rings substitution with heterocyclic aromatic unit through acene backbone. The idea of combining molecular shape of pentacene and thiophene end groups, exhibited very good results because of increased stability and favorable crystal packing. These type of chemical structures are called as “anthradithiophene”. Anthony *et al.* developed a novel anthradithiophene based semiconductor M3, which showed 1.00 cm^2/Vs hole mobility and $\approx 10^7$ I_{on}/I_{off} ratio thanks to close π-π stacked interactions in the solid state.[27]

Takimiya and coworkers proposed a new design strategy; in contrast to traditional semiconductor molecule architecture they used heterocycles in the centre and benzenes at the end of the core. This approach cause much higher mobilities compared to other semiconductor small molecules in which thiophene and heterocycles are located vice versa.[20,28] M4 showed ambient stable character via low lying HOMO energy level with 2.00 cm^2/Vs hole mobility and I_{on}/I_{off} ratio of 10^7. Pyrene based organic semiconductors have been rarely studied in comparison with oligothiophene and heteroacene small molecules. Lee *et al.* synthesized a new pyrene based liquid crystalline semiconductor M5 with 2.1 cm^2/Vs hole mobility and I_{on}/I_{off} ratio of 10^7. This results approved that pyrene based materials hold great promise for high performance OTFTs.[29]

Lastly, styrylacenes have been used as a new *p*-channel semiconducting small molecule for OFETs. Acene core stability has been increased by π conjugation extension within a styrene group. Perecichka *et al.* reported a new styrylacene based semiconductor M6 which exhibited 1.5 cm^2/Vs hole mobility in thin-films and 2.6 cm^2/Vs in single crystals.[30]

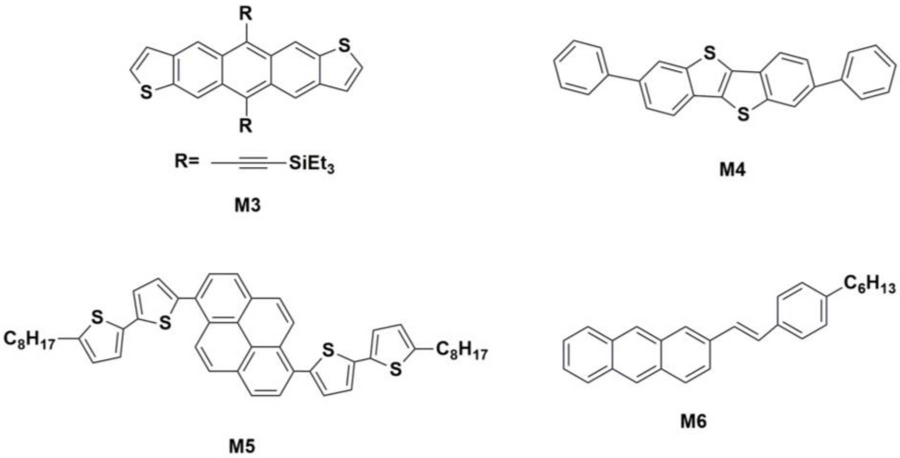

Figure 1.1.2.1.4 Chemical structures of p-channel small molecule semiconductors.

1.1.2.2 Polymeric and Small-Molecule *n*- Channel Semiconductors for OFETs

The majority of organic semiconductors demonstrate *p*-type characteristics, so charge-carrier transportation is based on holes. The injection of holes through semiconducting layer is easier than electrons due to the strong electron trapping. Therefore *n*-channel molecular systems underdeveloped compared to *p*-channel semiconductors. Most of *n*-channel semiconductors exhibit air sensitivity, low charge-carrier mobility and insolubility. The first reported *n*-channel polymeric semiconductor was poly(benzobisimidazo-benzophenanthroline) (BBL) P5, which was synthesized by Babel and coworkers.[31] Solution processable *n*-channel polymeric semiconductor P(DTI) P6 was explored by Letizia *et al.*, and it has electron mobility >0.01 cm^2/Vs.[32] P7 is the first perylenediimide-based *n*-channel semiconductor which was reported by Zhan and coworkers. P7-based OTFT device showed 0.01 cm^2/Vs electron mobility and $> 10^4$ I_{on}/I_{off} ratio under nitrogen.[33] Instead of bithiophene, selenophene based donor unit was used in the synthesis of new naphthalene diimide based polymer P8 which is reported by Jenekhe *et al*. OFET device performance of P8 was in the average of 0.24 cm^2/Vs for electron mobility and I_{on}/I_{off} ratio of $10^4 – 10^6$.[34]

Pei and coworkers reported a new benzodifurandione based *n*-channel polymeric semiconductor which contains a highly electron deficient group. One of the highest *n*-channel OFET device performance is achieved by using this polymer under ambient conditions. It exhibited e$^-$ mobility of 1.1 cm^2/Vs.[35] Patil *et al.* have used DPP-based polymers for *n*-channel device operations. DPP core has special properties such as strong electron deficiency, highly planar backbone and good inter-molecular π-π interactions. Therefore P10 showed very good e$^-$ mobility of 3 cm^2/Vs.[36]

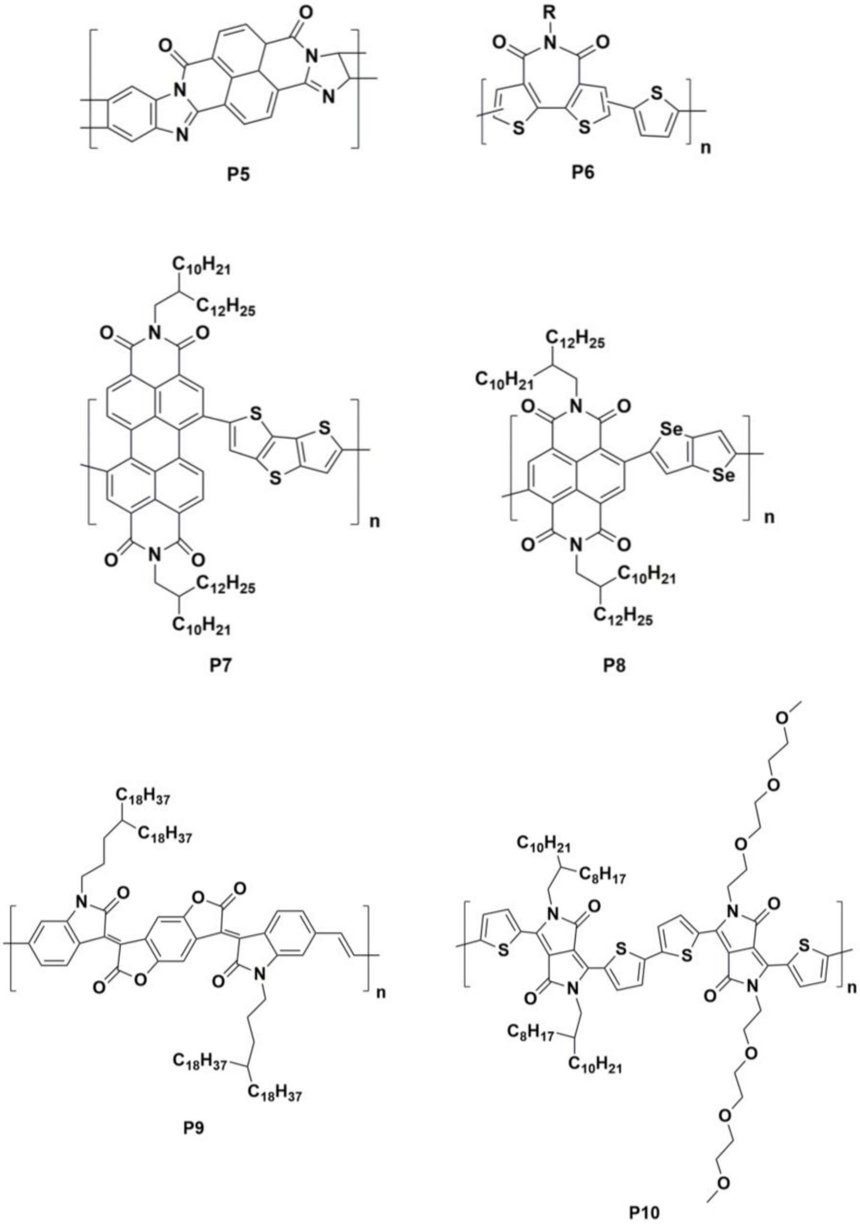

Figure 1.1.2.2.1 Chemical structures of *n*-channel polymeric semiconductors.

Guillaud and coworkers reported the first small molecule *n*-channel OFET in the literature.[37] M7 is the first air-stable small molecule *n*-channel OFET, and it was synthesized by Bao *et al.* which presented electron mobility of 0.03 cm^2/Vs under ambient conditions.[38]

The first oligothiophene small molecules (M8) were introduced in 2000 by Facchetti and coworkers, which includes perfluorohexyl chains.[39] In spite of low electron mobility of DFH-nT based devices, this study guided the development of air stability in *n*-channel OFET device literature.

Currently, fullerene (C60) derivates have the highest e^- mobility of up to 0.5 cm^2/Vs. One of the best value in the *n*-channel OFET literature to date was achieved by [60]PCBM-M9 ([6,6]-phenyl-C61-butyric acid methyl ester) which is soluble in common organic solvents.[40]

Rylene diimide based small molecule *n*-channel OFET was fabricated by Katz *et al.*, and M10 molecule exhibited 0.16 cm^2/Vs e^- mobility under vacuum.[41]

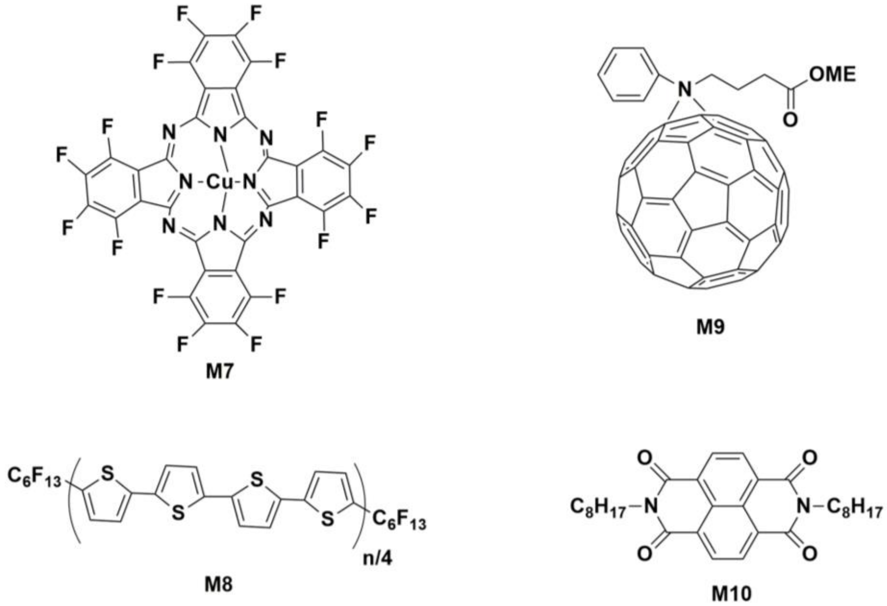

Figure 1.1.2.2.2 Chemical structures of *n*-channel small molecule semiconductors.

1.1.2.3 Polymeric and Small-Molecule Ambipolar Semiconductors for OFETs

Today OTFTs are mainly unipolar devices due to fact that injection of electrons (*n*-type) or holes (*p*-type) through semiconducting layer. But, recently, ambipolar organic semiconductors have drawn attention due to their distinctive properties which enable the injection of electrons and holes simultaneously within the channel. Ambipolar semiconductors can be used in organic light emitting transistors (OLETs), light-sensing organic thin-film transistors (LS-OTFTs) and single-component CMOS-type organic logic circuits applications.[42–46]

Intrinsic ambipolar materials exhibit typical donor-acceptor relation, which is based on electron rich, and electron poor units' interaction. Furthermore, commonly they have lower band gap (<2ev) compared to unipolar systems.

Sirringhaus and coworkers have synthesized polyselenophenes as an alternative to polythiophenes.[47,48] P11 based OTFTs presented good ambipolarity with balanced mobility (>0.01 cm^2/Vs) and effective complementary-like inverters performance.

Napthalenebiscarboximide-bithiophene based ambipolar semiconductors have been reported by Watson *et al*. They used dialkoxybithiophene as a electron donor, and naphthalene bisimide as an electron acceptor unit. P12 based OTFT device exhibited e^- mobility of 0.04 cm^2/Vs, h^+ mobility of 0.003 cm^2/Vs, and output voltage gains of 30.[49]

DPP based ambipolar polymer was synthesized by Winnewisser and coworkers, which has low band-gap, solution processability and good ambipolar charge transfer feature. P13-based OTFT device showed 0.09 cm^2/Vs e^- mobility and 0.1 cm^2/Vs h^+ mobility.[22]

Reynolds *et al*. used dithienopyrole (DTP) as an electron donor and benzobisthiadiazole (BBT) as an electron acceptor, which enable to obtain low band gap and the injection of both charge carriers at the same time (ambipolarity). DTP-BBT systems displayed one of the smallest optical band gap (0.5-0.6 eV) among the other soluble polymers in the literature. However, OTFT device performance of P14 was poor with 5.8×10^{-4} cm^2/Vs e^- and 1.2×10^{-3} cm^2/Vs h^+ mobility.[50]

Isoindigo based ambipolar polymers was synthesized by Pei *et al*. for the first time. They used isoindigo as an electron acceptor and bithiophene as an electron donor. This group achieved to lower LUMO energy level thanks to fluorination and escalates electron mobility in air. In additional, hole mobility (1.85 cm^2/Vs) of P15-based device was very good under ambient conditions.[51]

Benzobisthiadiazole (BBT) used in ambipolar polymeric device fabrication because of its high electron affinity. BBT based polymers with different donor units have been synthesized by Wudl and coworkers, which has low band gap. Thanks to the proper alignment of HOMO and LUMO around the working electrode Fermi level, P16 based device showed outstanding ambipolarity with mobility of electrons and holes over 1 cm^2/Vs.[52,53]

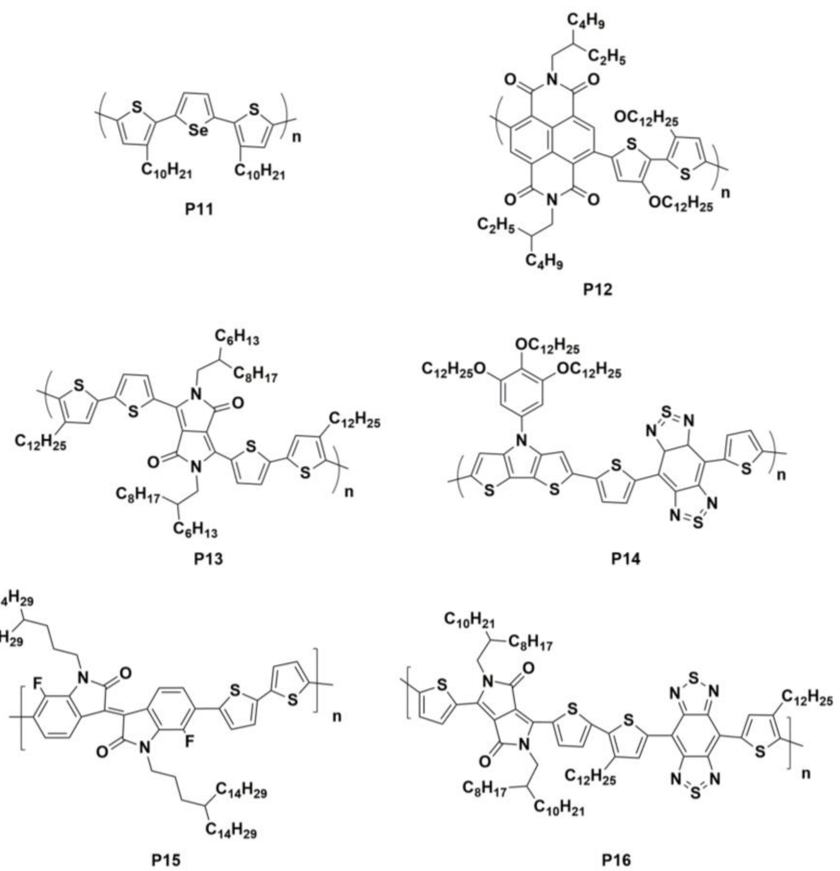

Figure 1.1.2.3.1 Chemical structures of ambipolar polymeric semiconductors.

Acene based small molecular ambipolar semiconductor was synthesized by Bao *et al*. M11 molecule exhibited balanced ambipolar character with e$^-$ and h$^+$ mobility of 0.133 and ~ 0.1 cm^2/Vs.[54] Nakanotani and coworkers reported the phenylenevinylene based ambipolar semiconductors. Highly balanced ambipolar device character was shown by M12 molecule which exhibited electron and hole mobilities both greater than 0.1 cm^2/Vs.[55] DPP based semiconductors with cyano functional groups was used by Wang *et al*. Solution processable, low band gap small molecule (1.48 eV) M13 displayed h$^+$ and e$^-$ mobilities of 0.07 and 0.03 cm^2/Vs ^{1} under ambient conditions.[56] Sulfur bridged tetrathienylene semiconductor was synthesized by Nishinaga and coworkers in which ambipolarity was achieved via antiaromaticity. OTFT device based on M14 molecule showed 0.18 cm^2/Vs electron and 0.40 cm^2/Vs hole mobility.[57] Aoyama *et al*. used quinoidal based small molecule in the OTFTs which was crucial for the next generation devices due to its promising outputs. The reason behind was ultra-low band gap of this molecule (~ 0.9 eV), which opens the door of dual charge injection in the solid state. OTFT based on M15 molecule displayed h$^+$ and e$^-$ mobilities of 0.1 and 0.006 cm^2/Vs respectively.[58] Quaterrylenediimide based ambipolar semiconductor was produced by Mullen and coworkers. Thanks to π-conjugation extension, HOMO energy level was increased while LUMO staying the same. Solution processed OTFT based on M16 molecule displayed both h^+ and e^- mobilities of ~10^{-3} cm^2/Vs. The main point in this work was, disappearing of ambipolarity with thermal annealing which shows that there is a linkage between morphology and device performance.[59]

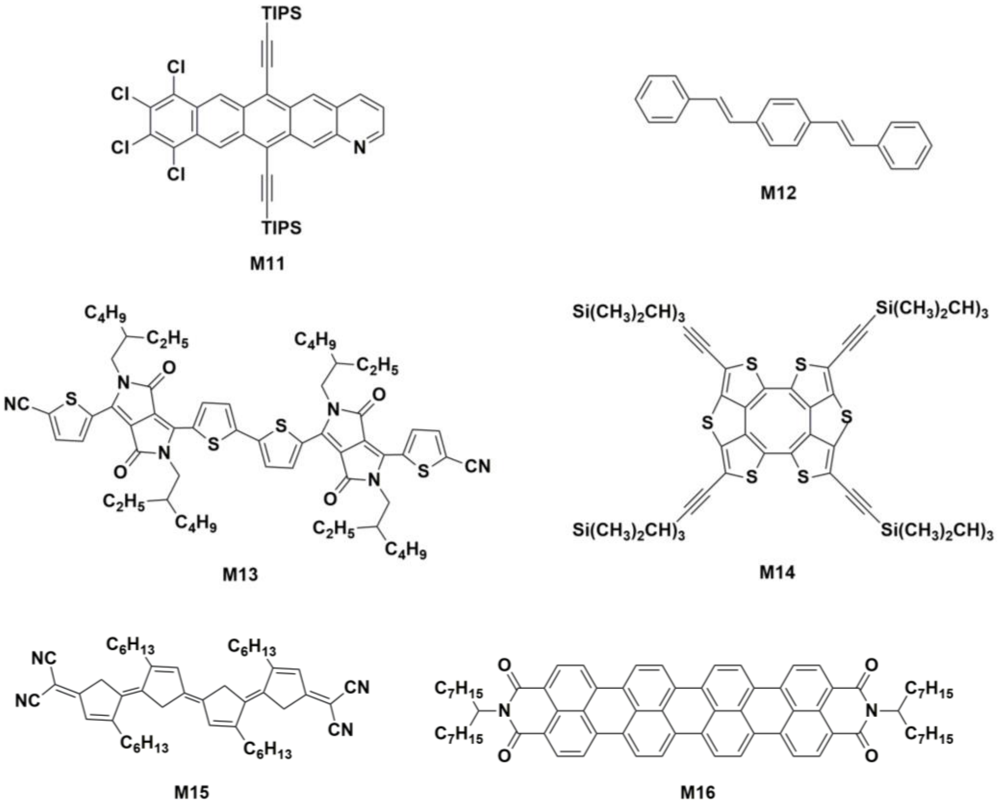

Figure 1.1.2.3.2 Chemical structures of ambipolar small molecule semiconductors.

1.2 Research Strategy and Overview of This Thesis

Ambipolar organic semiconductors constitute an important class of semiconductor materials that have recently attracted widespread scientific and technological interest to realize low-cost, mechanically flexible, large-area, and printed optoelectronic devices such as single-component CMOS (complementary metal-oxide semiconductor)-type transistor circuits and light-emitting transistors (OLETs). To date, ambient-stable and solution-processable ambipolar semiconductors have been mainly reported with donor-acceptor (D-A) type π-conjugated polymers, and charge carrier mobilities exceeding those of amorphous silicon ($\mu_{e,h} > 0.5$ $cm^2/V \cdot s$) have been achieved in polymeric organic field-effect transistors

(OFETs). Most of these polymers have highly extended π-cores resulting in small HOMO-LUMO energy gaps (< 2.0 eV) to facilitate charge injection/transport of both electrons and holes under ambient conditions.

Nevertheless, very few solution-processed small molecules with ambipolar charge-transport are known to operate in ambient. This is mainly due to the difficulty of achieving such low HOMO-LUMO energy gaps (<2.0 eV) and sufficiently low LUMOs (<-4.1 eV) within a limited molecular π-conjugation length. To date, although many high mobility (>30 $cm^2/V·s$) unipolar (p-channel or *n*-channel) molecular semiconductors have been developed with good solution-processibility and ambient stability, there are very few ambipolar small molecules exhibiting these characteristics. Therefore, the continued efforts to design and develop ambipolar small molecules are crucial to fully reveal their technological potential and to study the fundamentals of electron vs. hole charge transport processes in molecular solids.

In chapter two, our efforts on designing, synthesizing and characterizing of two new ladder-type solution-processable and air stable ambipolar small molecules, 2OD-TTIFDK and 2OD-TTIFDM are described. Based on novel semiconductors, fabrication and performance analysis of organic field effect transistors are exhibited. Also the applications of the new ambipolar transistors to complementary-like inverters are demonstrated.

Among the molecular semiconductors studied to date, small molecules with electron-deficient π-architectures and low LUMO energy levels constitute an important class of materials for air-stable electron transport in p-n junctions, bipolar transistors, and organic complementary-like circuitry (CMOS). In addition, π-deficient small molecules can function as non-fullerene electron acceptors for use in bulk-heterojunction organic solar cells. However, among the molecular semiconductors developed to date, air-stable and solution-processable *n*-channel molecular semiconductors are still scarce. Therefore, the continued research efforts to this end are very important to enhance structural variety and device performances, and to better understand structure-property-device relationships.

In chapter three, our efforts on designing, synthesizing and characterizing of two new highly electron-deficient D-A-D type solution-processable and air-stable *n*-type small molecules α,ω-2EH-TIFDMT and α,ω-2OD-TIFDMT are described. Based on novel semiconductors, fabrication and performance analysis of organic field effect transistors are demonstrated.

Chapter 2

Design, Synthesis, and Characterization of Ultralow Bandgap Molecular Semiconductors for Ambient-Stable and Solution-Processable Ambipolar Organic Field-Effect Transistors

2.1 Introduction

Ambipolar organic semiconductors are attractive functional materials as potential alternatives to conventional inorganic semiconductors (i.e., Si, Ge, GaAs, etc.) both for fundamental research and for the fabrication of flexible, low-cost, and light-weight optoelectronic devices such as single-component CMOS (complementary metal-oxide semiconductor)-type transistor circuits and light-emitting transistors (OLETs).[1–8] Device optimizations such as dielectric surface treatments,[9] electrode surface modifications,[10] and using non-symmetric work-function electrodes,[11] or depositing bilayer/blend semiconductor films[12–14] have been successfully employed to realize ambipolar charge-transport in organic field-effect transistors (OFETs). However, the most ideal approach would be to have an intrinsically ambipolar π-system, regardless of the device architecture.[1,15] The ability of an intrinsic ambipolar semiconductor to transport both electrons and holes, as an initial approximation, usually requires energetically close HOMO and LUMO frontier orbitals (energy gap < 2.0 eV), which are symmetrically positioned around the metal electrode fermi level, and also requires good solid-state orbital overlaps between neighboring π-systems.[12,16,17] In order to utilize ambipolar semiconductors in ideal optoelectronic applications, charge transport of electrons and holes should be balanced ($\mu_e/\mu_h \approx 1$) with good mobility and ambient-stability. This is particularly important to achieve maximum gains in logic circuits and light-emission efficiencies in OLETs. In addition, in order to enable low-cost, facile device fabrications via spin-coating, solution-shearing, and printing, the semiconductors should exhibit good solubilities in common organic solvents.

To date, ambient-stable and solution-processable ambipolar semiconductors have been mainly reported with π-conjugated polymers, and charge carrier mobilities exceeding those of amorphous silicon ($\mu_{e,h} > 0.5$ $cm^2/V{\cdot}s$) have been achieved in polymer-based organic field-effect transistors (OFETs).[18–20] Most of these polymers have highly extended donor-acceptor (D-A) type π-backbones, which leads to π-electronic structures with small HOMO-LUMO energy gaps (< 2.0 eV) and low LUMO energies (<-4.0 eV) to facilitate charge injection/transport of both electrons and holes under ambient conditions.[21–23] Nevertheless, very few solution-processed small molecules with ambipolar charge-transport are known to operate in ambient.[24–26] This is mainly due to the difficulty of achieving such low HOMO-LUMO energy gaps and sufficiently low LUMOs within a limited π-extension of a molecular backbone. When compared with polymers, small molecular π-conjugated systems offer advantageous properties including enhanced solubility, higher crystallinity, better synthetic reproducibility, and higher degree of purity.[27–31] Since the early studies on hole-transporting thiophene-based small molecules in OFETs,[32] the design and development of novel molecular π-architectures with solution-processibility and ambient-stability have been quite important for the realization of printed electronic circuits which can operate in ambient.[33–37] To date, many high mobility (>1.0 $cm^2/V{\cdot}s$) unipolar (*p*-channel or *n*-channel) molecular semiconductors have been developed,[38,39] however, there are very few ambipolar small molecules exhibiting good solution-processibility and ambient stability.[40–42] In addition, the majority of these ambipolar small molecules are based on diketopyrrolopyrrole (DPP) acceptor core, and they typically have electron/hole mobilities in the range of ~0.001-0.1 $cm^2/V{\cdot}s$.[43,44] To the best of our knowledge, the highest ambient-stable electron mobility reported to date was for an ambipolar DPP-based small molecule with μ_e = 0.6-0.8 $cm^2/V{\cdot}s$; however, this molecule exhibited much lower hole mobility of ~10^{-3} $cm^2/V{\cdot}s$ for the same device.[45] Therefore, the continued research efforts to design and develop new ambipolar small molecules are crucial to realize high and balanced charge carrier mobilities, to fully reveal their technological potential and to elucidate the fundamentals of electron *vs.* hole transport processes in novel molecular solids.

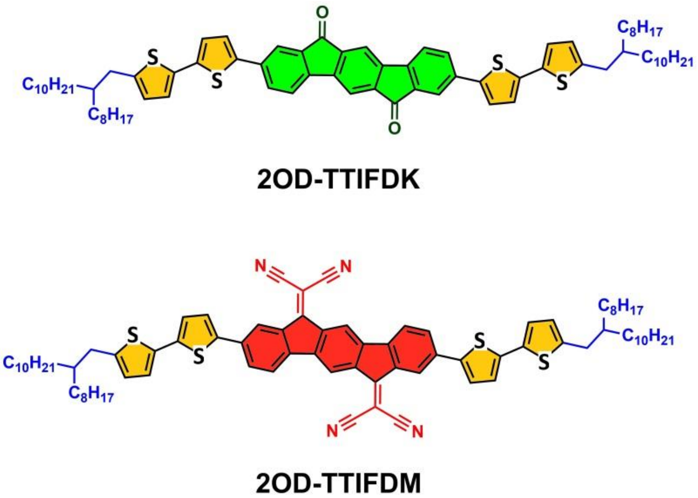

Figure 2.1.1 The chemical structures of **2OD-TTIFDK** and **2OD-TTIFDM** showing the α-substituted bithiophene donor units in yellow, indeno[1,2-b]fluorene-6,12-dione (IFDK) acceptor unit in green, and indeno[1,2-b]fluorene-6,12-diylidene) dimalononitrile (IFDM) acceptor unit in red.

To achieve reasonably balanced ambipolarity in a small molecular backbone, we utilized the strategy of building very strong D-A-D π-architecture using ladder-type indeno[1,2-b]fluorene-6,12-dione (**IFDK**) and indeno[1,2-b]fluorene-6,12-diylidene)dimalononitrile (**IFDM**) π-acceptors and α-substituted bithiophene terminal π-donor units.[46] This approach can yield very small HOMO-LUMO gaps since HOMO is dominated by π-donor unit while LUMO is dominated by π-acceptor unit. In addition, structural and electronic properties of cyclopenta-fused scaffolds can be favorable to stabilize both positive and negative charges on these new molecular backbones.[47] Specifically, **IFDM** was used due to its great coplanarity and extremely strong electron-accepting ability in a proper sized π-core.[48] Swallow-tailed alkyl substitutents, 2-octyldodecyl (2-OD), are placed at molecular termini (α,ω-positions) to ensure good solubility while minimizing inter-ring twists.[49] Here, two new ladder-type small molecules, 2,8-bis(5'-(2-octyldodecyl)-2,2'-bithiophen-5-yl)indeno[1,2-b]fluorene-6,12-dione (**2OD-TTIFDK**) and 2,2'-(2,8-bis(5'-(2-octyldodecyl)-2,2'-bithiophen-5-yl)indeno[1,2-b]fluorene-6,12 diylidene)dimalononitrile (**2OD-TTIFDM**) were designed, synthesized and characterized (Figure 2.1.1.). The chemical structures, physicochemical and optoelectronic properties of new compounds were characterized by ^{1}H/^{13}C NMR, TGA, DSC, UV-Vis and CV. Our design yields ultra-low solid-state band gaps of 1.65 eV for **2OD-TTIFDK** and 1.21 eV for **2OD-TTIFDM** with favorable HOMO/LUMO energy levels of -5.47/-3.61 eV and -5.49/-4.23 eV, respectively, for balanced ambipolarity. Specifically, the sufficiently low LUMO of dicyanovinylene-functionalized molecule, **2OD-TTIFDM**, enables ambient-stable electron-transport, while properly aligned HOMO level facilitates hole injection/transport. Top-contact/bottom-gate OFETs fabricated via solution-shearing of **2OD-TTIFDM** yield perfectly ambient-stable ambipolar devices with relatively balanced electron and hole mobilities of 0.13 $cm^2/V\cdot s$ and 0.01 $cm^2/V\cdot s$, respectively, and I_{on}/I_{off} ratios of $10^3 – 10^4$. On the other hand, the carbonyl-functionalized molecule, **2OD-TTIFDK**, exhibits highly balanced ambipolarity (μ_e/μ_h ~ 2) under vacuum with electron and hole mobilities of 0.02 $cm^2/V\cdot s$ and 0.01 $cm^2/V\cdot s$, respectively and I_{on}/I_{off} ratios of $10^5 – 10^6$. We have also successfully demonstrated the application of the new ambipolar transistors to complementary-like inverters, which is the building block of integrated circuits for data processing. The new inverters exhibit high voltage gains of 30 in ambient for **2OD-TTIFDM** and 223 in vacuum for **2OD-TTIFDK**. Our findings indicate that although D-A-D π-skeleton stays the same for both small molecules, energetic stabilization of LUMO (-3.61 eV → -4.23 eV) as a result of functional group modification is key to the ambient stability of the corresponding OFETs. The theoretical calculations explain the differences in molecular energetics and provide insights into the current functionalization strategies. Our results clearly indicate that **IFDM** π-core is a proper-sized, favorable acceptor unit for building efficient, soluble ambipolar small molecules to operate in ambient. Considering the processing, charge-transport and inverter characteristics, the current molecular semiconductors are among the best performing ambipolar small molecules in the OFET and CMOS-like inverter literature.

2.2 Experimental

2.2.1 Materials and Methods

The chemicals and reagents were purchased from commercial suppliers and used directly unless otherwise noted. Traditional vacuum/nitrogen manifold system was managed, and all the reactions were performed under N_2. By using Bruker 400 spectrometer (^{1}H, 400 MHz; ^{13}C, 100 MHz), ^{1}H/^{13}C NMR spectra were obtained. Elemental analyses were carried out via Leco Truspec Micro. TGA and DSC analysis were recorded under nitrogen atmosphere via Perkin Elmer Diamond with 10 °C/min heating rate. C3 Cell Stand equipped Epsilon potentiostat/galvanostat was used for cyclic voltammetry measurements. Shimadzu UV-1800 spectrophotometer was used for UV-vis absorption measurements. By using BrukerMicroflex LT MALDI-TOF-MS device, MALDI-TOF measurements were recorded. Through Gaussian 09, the calculations of total energy and molecular geometry were performed via density functional theory (DFT) at the B3LYP/6-31G** basis set.[50] The synthesis of 2-octyldodecylbromide and 2,8-dibromoindeno[1,2-b]fluorene-6,12-dione (**IFDK-Br$_2$**) were performed according to previously reported procedure.[49]

2.2.2 Synthesis and Characterization

2.2.2.1 5-(2-octyldodecyl)-2,2'-bithiophene (1)

To a solution of 2,2’-bithiophene (1.353 g, 8.14 mmol) and 25 mL of THF, *n*-butyllithium (3.41 mL, 8.52 mmol) was added dropwise at −78 °C under nitrogen. The reaction was carried out by stirring at −78 °C for 30 min and then at room temperature for 1 h, which was followed by 2-octyldodecylbromide (3.11 g, 8.95 mmol) adding at −78 °C. Afterwards, the reaction mixture was refluxed for 12 h. After the reaction was finished, the reaction mixture was quenched with water and the product was extracted into an organic phase by using chloroform. Then crude product was obtained after evaporation until dryness, which was purified through flash chromatography with hexane to give the final product. (1.415 g, 38.8% yield). ^{1}H NMR (400 MHz, $CDCl_3$): δ 0.89 (m, 6H), 1.27-1.35 (m, 33H), 2.72 (d, 2H, J = 6.8 Hz), 6.66 (d, 1H, J = 3.2 Hz), 6.99 (m, 2H), 7.11 (d, 1H, J = 3.2 Hz), 7.17 (d, 1H, J = 5.2 Hz).

2.2.2.2 Trimethyl(5'-(2-octyldodecyl)-[2,2'-bithiophen]-5-yl)stannane (2)

To a solution of 5-(2-octyldodecyl)-2,2'-bithiophene (**1**) (1.415 g, 3.17 mmol) and 30 mL of THF, *n*-butyllithium (1.33 mL, 3.33 mmol) was added dropwise at −78 °C under nitrogen. The reaction was carried out by stirring at −78 °C for 30 min and then at room temperature for 1 h, which was followed by trimethyltin chloride (0.695 g, 3.49 mmol) adding gradually at −78 °C. Afterwards, the resulting mixture was refluxed during the night. After the reaction was finished, the reaction mixture was quenched with water. The organic phase separated by using hexane. After the solvent was evaporated, the final product was obtained (1.889 g, 97.7% yield). ^{1}H NMR ($CDCl_3$, 400 MHz): δ 0.39 (s, 9H), 0.89 (m, 6H), 1.27-1.35 (m, 33H), 2.72 (d, 2H, J = 6.4 Hz), 6.65 (d, 1H, J = 3.2 Hz), 6.98 (d, 1H, J = 3.2 Hz), 7.07 (d, 1H, J = 3.6 Hz), 7.22 (d, 1H, J = 3.6 Hz).

2.2.2.3 2,8-bis(5'-(2-octyldodecyl)-2,2'-bithiophen-5-yl)indeno[1,2-b]fluorene-6,12-dione (2OD-TTIFDK).

To a solution of 2,8-dibromo-indeno[1,2-b]fluorene-6,12-dione(**IFDK-Br$_2$**) (0.282 g, 0.641 mmol), and trimethyl(5'-(2-octyldodecyl)-[2,2'-bithiophen]-5-yl)stannane (**2**) (0.860 g, 1.41 mmol) in DMF (40mL), $Pd(PPh_3)_2Cl_2$ (45.0 mg, 0.0641 mmol) was added. The reaction mixture was heated at 125 °C under nitrogen for 2 days. After the reaction was completed, the reaction mixture was quenched with water. The organic phase separated by using chloroform. After the solvent was evaporated, the residue was purified through flash column chromatography with chloroform to give the final product. (0.230 g, 30.6% yield). m.p. 217-218 °C. ^{1}H NMR (400 MHz, $CDCl_3$): δ

0.90 (m, 6H), 1.28-1.32 (m, 33H), 2.72 (d, 2H, J = 6.4 Hz), 6.64 (d, 1H, J = 3.6 Hz), 6.98 (m, 2H), 7.18 (d, 1H, J = 3.6 Hz), 7.41 (d, 1H, J = 7.6 Hz), 7.62 (d, 1H, J = 8.5 Hz), 7.64 (s, 1H), 7.73 (s, 1H). ^{13}C NMR (100 MHz, $CDCl_3$): δ 14.1, 22.7, 26.6, 29.4, 29.5, 29.6, 29.7, 30.0, 31.9, 33.2, 34.6, 40.0, 115.6, 120.5, 120.8, 123.5, 123.7, 124.4, 125.9, 130.9, 134.4, 134.6, 135.3, 138.2, 139.2, 140.2, 141.3, 144.4, 145.2, 192.1. MS (MALDI-TOF) *m/z* (M^+): calculated. for $C_{76}H_{98}O_2S_4$: 1170.64, found: 1171.74 $[M+H]^+$. Anal. calculated for $C_{76}H_{98}O_2S_4$: C, 77.90; H, 8.43, found: C, 77.98; H, 8.64.

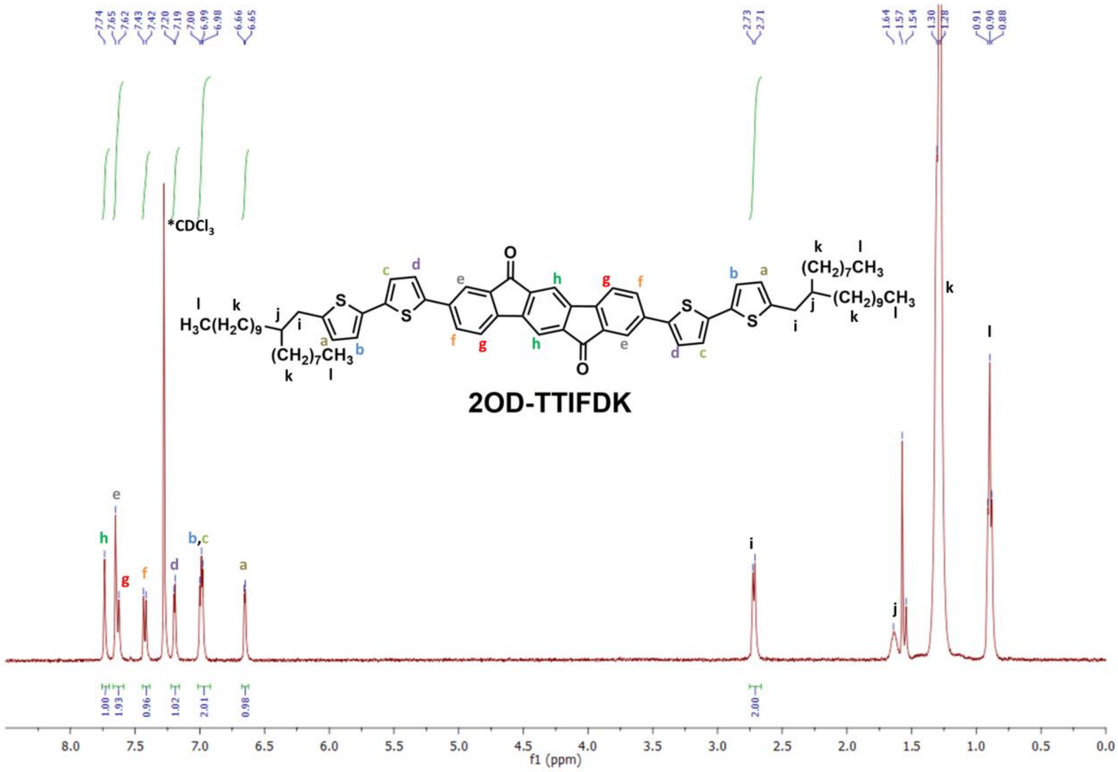

Figure 2.2.2.3.1 ^{1}H NMR spectra of **2OD-TTIFDK** measured in $CDCl_3$.

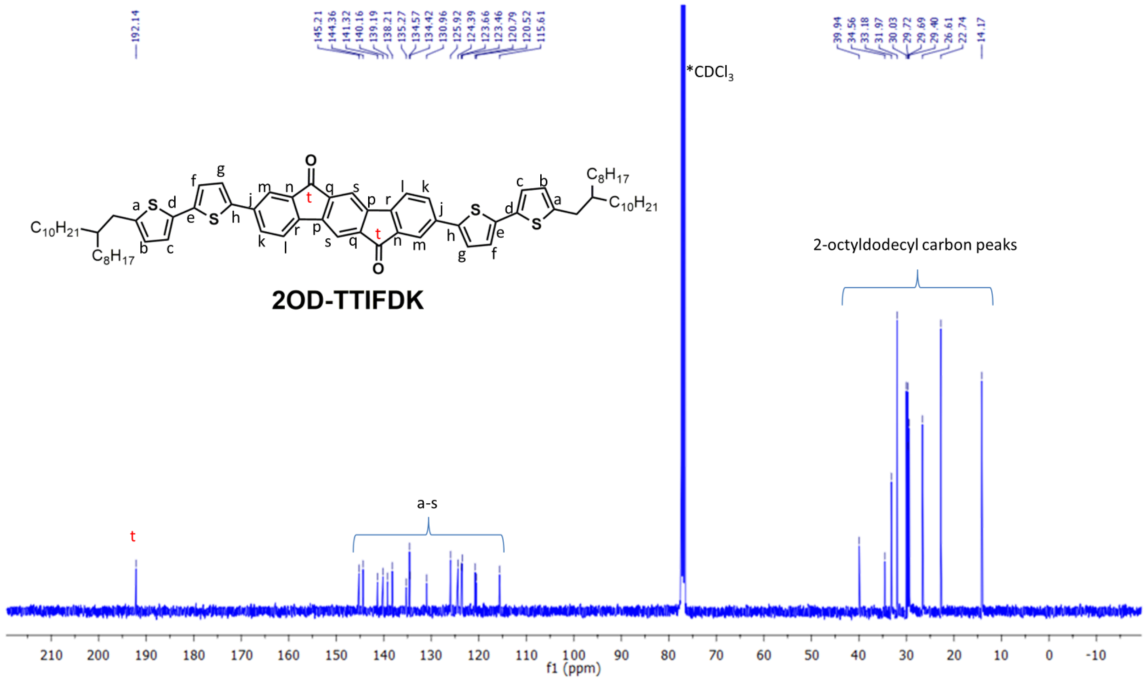

Figure 2.2.2.3.2 ^{13}C NMR spectra of **2OD-TTIFDK** measured in $CDCl_3$.

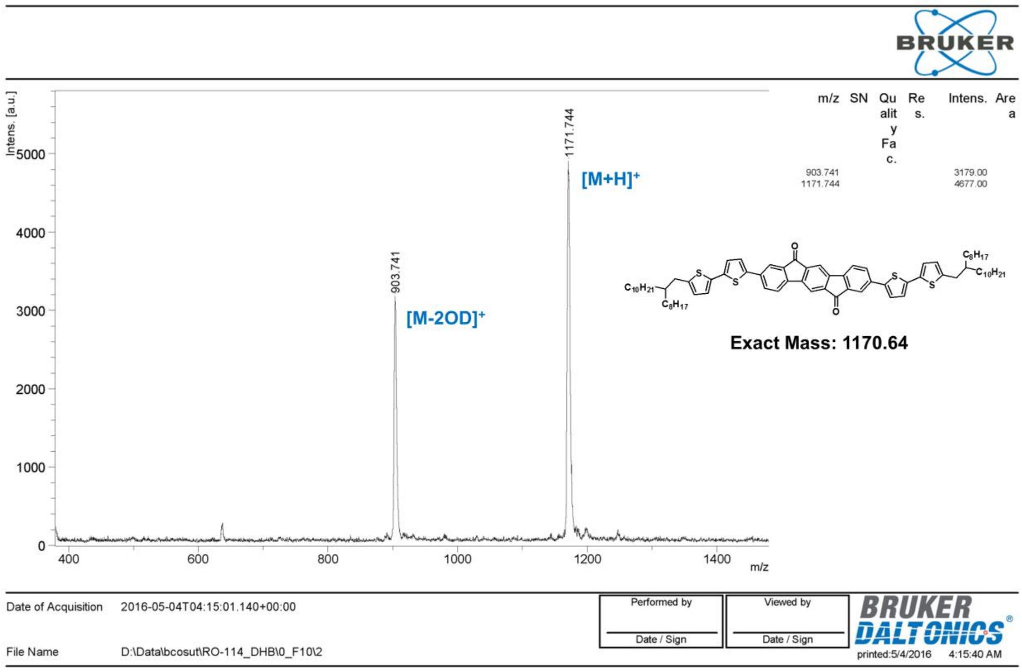

m/z	SN	Quality Fac.	Res.	Intens.	Area
903.741				3179.00	
1171.744				4677.00	

Date of Acquisition 2016-05-04T04:15:01.140+00:00

File Name D:\Data\bcosut\RO-114_DHB\0_F10\2

Performed by

Date / Sign

Viewed by

Date / Sign

printed:5/4/2016 4:15:40 AM

Figure 2.2.2.3.3 Positive ion and linear mode MALDI TOF-MS spectrum of **2OD-TTIFDK**

2.2.2.4 2,2'-(2,8-bis(5'-(2-octyldodecyl)-2,2'-bithiophen-5-yl)indeno[1,2-b]fluorene-6,12-diylidene)dimalononitrile (2OD-TTIFDM).

To a solution of 2,8-bis(5'-(2-octyldodecyl)-2,2'-bithiophen-5-yl)indeno[1,2-b]fluorene-6,12-dione (**2OD-TTIFDKTT**) (0.100 g, 0.085 mmol), dicyanomethane (79 mg, 1.19 mmol) and chlorobenzene (12 mL), pyridine (0.131 mL, 1.62 mmol) and $TiCl_4$ (0.094 mL, 0.853 mmol) were added under nitrogen. Next, the resulting reaction mixture was heated at 110 °C for 5 h. After the reaction was completed, the reaction mixture was quenched with water. The organic phase separated by using chloroform. After the solvent was evaporated, the residue was purified through flash column chromatography with chloroform to give the final product. (63 mg, 58.8% yield). m.p. 320-321 °C. ^{1}H NMR (400 MHz, $CDCl_3$): δ 0.90 (m, 6H), 1.27-1.35 (m, 33H), 2.57 (d, 2H, J = 6.0 Hz), 6.50 (d, 1H, J = 3.6 Hz), 6.81 (m, 2H), 7.01 (d, 1H, J = 3.6 Hz), 7.24 (d, 1H, J = 8.0 Hz), 7.42 (d, 1H, J = 8.0 Hz), 8.02 (s, 1H), 8.04 (s, 1H). ^{13}C NMR (100 MHz, $CDCl_3$): δ 14.2, 22.7, 26.5, 29.3, 29.4, 29.6, 29.7, 29.8, 30.0, 32.0, 33.1, 34.5, 39.9, 112.6, 112.7, 117.4, 121.1, 122.3, 123.6, 123.9, 124.8, 126.0, 129.9, 130.2, 134.0, 134.4, 135.4, 138.4, 138.5, 138.9, 139.1, 142.4, 145.0, 158.5. MS (MALDI-TOF) *m/z* (M^+): calculated for $C_{82}H_{98}N_4S_4$: 1266.67, found: 1267.19 $[M+H]^+$. Anal. calculated for $C_{82}H_{98}N_4S_4$: C, 77.68; H, 7.79; N, 4.42, found: C, 77.96; H, 7.95; N, 4.56.

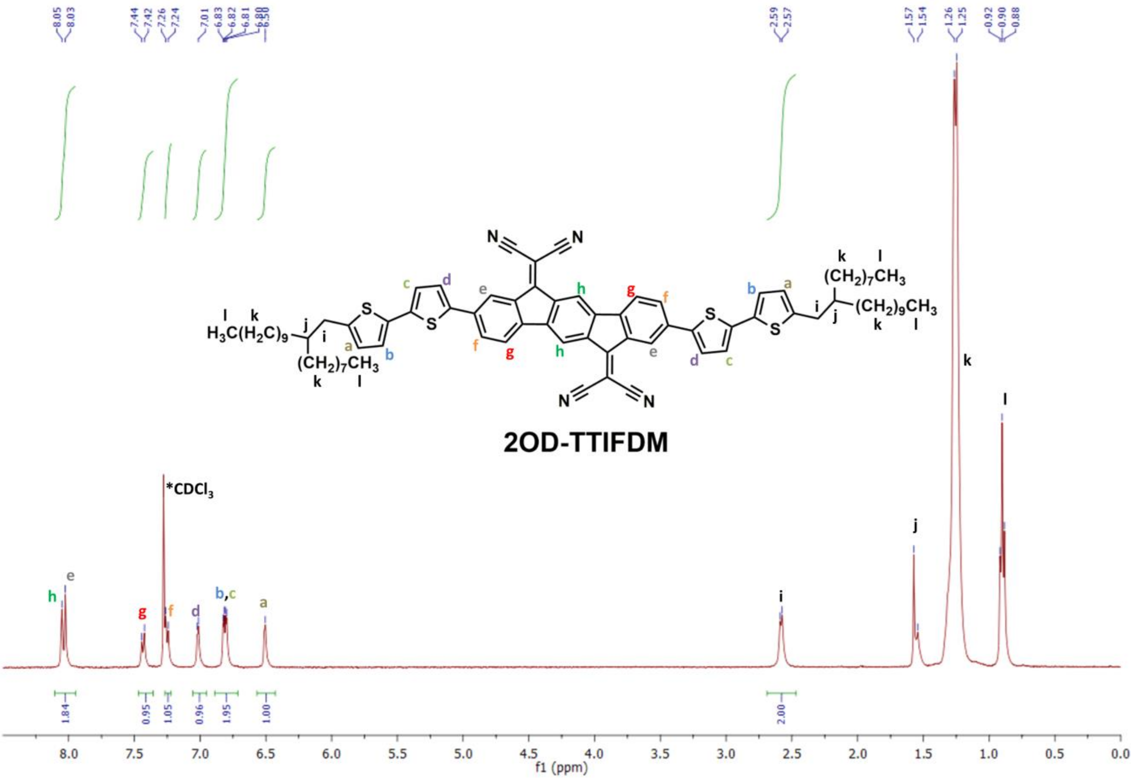

Figure 2.2.2.4.1 ^{1}H NMR spectra of 2OD-TTIFDM measured in $CDCl_3$.

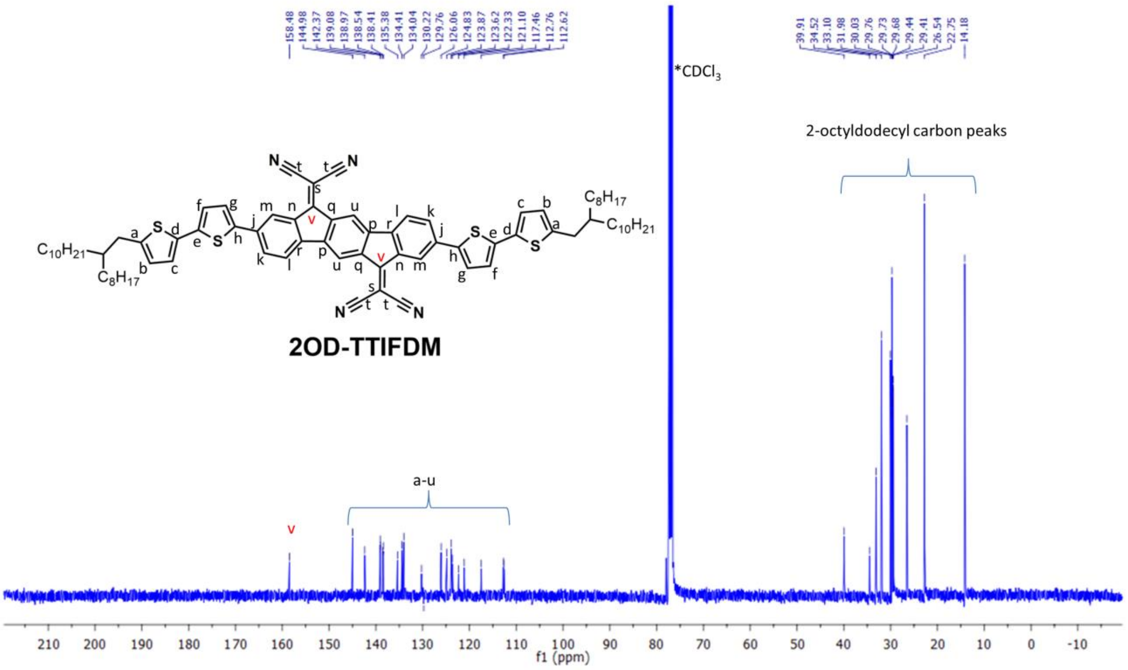

Figure 2.2.2.4.2 ^{13}C NMR spectra of **2OD-TTIFDM** measured in $CDCl_3$.

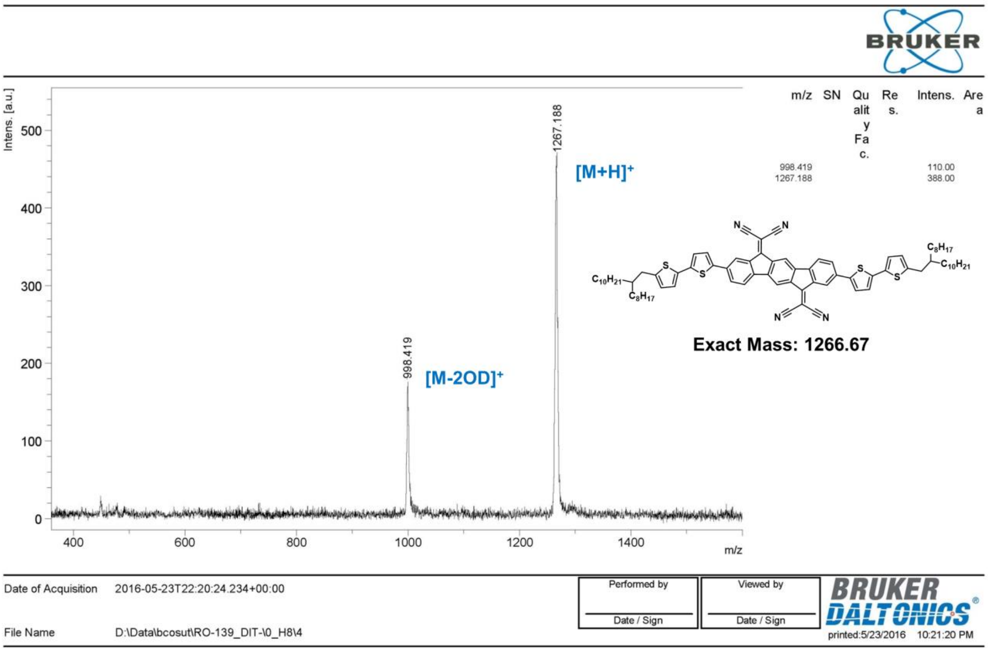

m/z	SN	Quality Fac.	Res.	Intens.	Area
998.419				110.00	
1267.188				388.00	

Date of Acquisition 2016-05-23T22:20:24.234+00:00

File Name D:\Data\bcosut\RO-139_DIT-\0_H8\4

printed:5/23/2016 10:21:20 PM

Figure 2.2.2.4.3 Positive ion and linear mode MALDI TOF-MS spectrum of **2OD-TTIFDM.**

2.2.3 OFET Device Fabrication and Characterization

All OFETs were fabricated on highly *n*-doped silicon wafers having thermally oxidized 300 nm SiO_2 dielectric (capacitance per unit area C_i =11.4 nF/cm^2) by adopting the top-contact/bottom-gate (TC/BG) device architecture. The substrates were cleaned by sonication of acetone during 10 min, cleaning of oxygen plasma during 5 min (Harrick plasma, PDC-32G, 18 W), respectively. The PS (polystyrene)-brush treatment was performed in accordance with the reported procedures (M_w = 1.7 – 10 kg/mol) to achieve favorable dielectric-semiconductor interfaces.[51–53] The organic semiconductor layers (**2OD-TTIFDK** and **2OD-TTIFDM**) were deposited via solution-shearing method on PS-brush-treated substrates. The solution-shearing method was performed based on the reported procedure, and the conditions were optimized with respect to solvent, solution concentration, substrate temperature, speed of shearing, and temperature of thermal annealing.[54] The substrates which is fabricated via solution-shearing method were kept under vacuum at 150 °C for 30 min, and then placed in a desiccator for 24 h to remove the residual solvent. The profilometer (DEKTAK-XT, Brucker) was used to measure the OSC film thicknesses (30 – 60 nm). The top electrodes were thermally evaporated (deposition rate = 0.2 Å/s) as Au layers (50 nm) with various channel widths (W; 1000 and 500 µm) and lengths (L; 100 and 50 µm). Keithley 4200-SCS was used to characterize the electronic performances of OFETs in ambient or in a vacuum probe station (< 10^{-2} Torr) at room temperature. The electronic performance in the saturation region such as charge carrier mobilities (µ) and threshold voltages (V_T) were extracted from the equation:

$$\mu_{sat} = (2I_{DS}L)/[WC_i(V_G - V_T)^2]$$

where I_{DS} is the drain current, L and W are the channel length and width, respectively, C_i is the areal capacitance of the gate dielectric, V_G is the gate voltage, and V_T is the threshold voltage. The reported OFET characteristics are the average of 10 different devices with standard deviations of less than 5-10%.The surface morphology and microstructure of thin-films were measured by atomic force microscopy (AFM, NX10, Park systems) and X-ray diffraction (XRD, Smartlab, Rigaku), respectively.

2.2.4 Fabrication and Characterization of Complementary-like Inverters

The complementary-like inverters were fabricated on the PS-brush treated n^{++}-Si/SiO_2 gate-dielectric substrate using two identical ambipolar OFETs based on **2OD-TTIFDK** or **2OD-TTIFDM** with a common gate as the input voltage (V_{IN}). The top electrodes with various channel widths (W; 2000, 1000, and 500 µm) and lengths (L; 100 and 50 µm) were deposited through shadow mask to define the electrode of supply bias (V_{DD}), the common electrode of output voltage (V_{OUT}), and the ground electrode. The channel dimensions for the two ambipolar OFETs were identical. The complementary-like inverters were characterized with the Keithley 4200-SCS instrument in ambient or under vacuum (< 10^{-2} Torr).

2.3 RESULTS AND DISCUSSIONS

2.3.1 Computational Modeling, Synthesis and Characterizations

Density-Functional Theory (DFT) study was performed on the model compounds **M1** and **M2** prior to the synthesis to gain initial insights into the molecular and electronic structures of the new molecules (Figure 2.3.1.1.). In these model compounds, shorter chains (isobutyl) were employed instead of longer alkyl chains (2-octyldodecyl) to ease the calculations by reducing degrees of freedom. Based on the energy-minimized geometries, **IFDK** and **IFDM** π-cores are found to adopt high co-planarity while some degree of acceptable inter-ring twists exist between these cores and outer thiophene units ($\theta < 22^\circ$). For both compounds, HOMO is highly delocalized along the molecular backbone and LUMO is more localized on the acceptor cores. However, the proper size of the acceptor unit may still ensure efficient intra-/inter-molecular π-delocalization and therefore good electron transport. The theoretical HOMO-LUMO energy gaps are estimated as 2.27 eV for **M1** and 1.45 eV for **M2**. The large reduction in the energy gap originates mainly from the LUMO level reduction (-2.90 eV → - 3.87 eV) as a result of functional group modification from carbonyl to dicyanovinylene. The origin of this reduction is a result of favorable inductive and mesomeric effects of dicyanovinylene *vs.* carbonyl ensuring very low LUMO level with minimal influences on HOMO energy level. The low LUMO energy level of **M2** is ideal for air-stable electron transport, which, when combined with its still relatively high HOMO, should enable ambipolarity in ambient. It is noteworthy that although ambipolarity may also be expected from **M1**, based on its relatively high LUMO, the electron-transport is not expected to be stable in ambient.

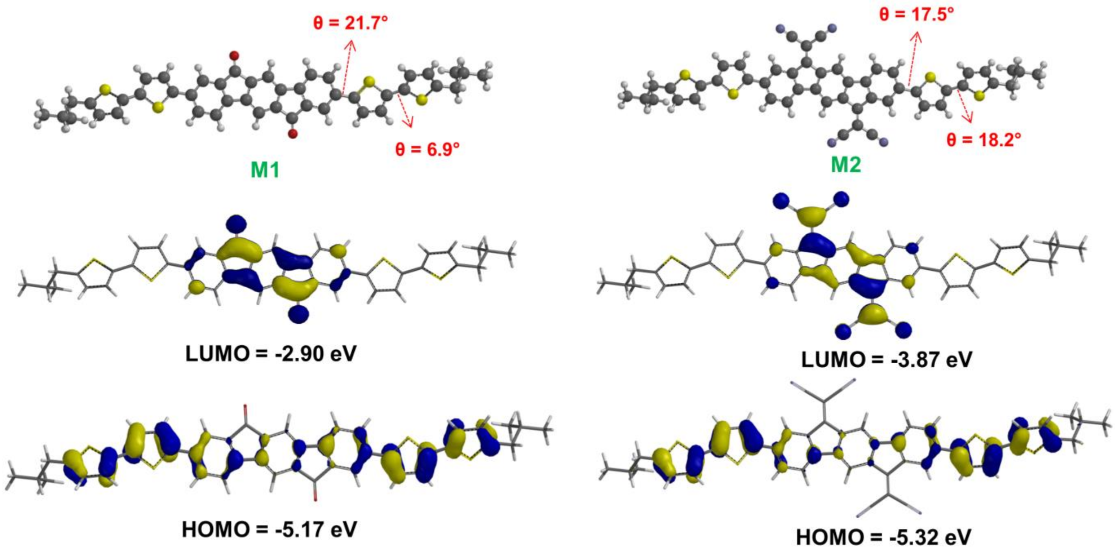

Figure 2.3.1.1 Molecular structures of **M1** and **M2** model compounds. Inter-ring dihedral angles were determined via optimized molecular geometries, calculated energy levels of HOMO/ LUMO, and representations of topographical orbitals at B3LYP/6-31G**basis set.

Figure 2.3.1.5. shows the synthesis of the stannylated π-donor moiety, trimethyl(5'-(2-octyldodecyl)-[2,2'-bithiophen]-5-yl)stannane (**2**) and the corresponding α,ω-disubstituted molecules **2OD-TTIFDK** and **2OD-TTIFDM**. The synthesis of the ladder-type acceptor core **IFDK-Br2** was carried out via Suzuki cross-coupling and intramolecular Friedel-Crafts acylation reactions in accordance with the established procedure by our group. Donor unit, **2**, was prepared from bithiophene in two steps: in the first step, bithiophene was monolithiated and capped with 2-octyldodecylbromide to yield **1** in 39% yield, and subsequently, **2** was synthesized from **1** in 98% yield via a conventional lithiation/stannylation reaction. The synthesis of the new carbonyl functionalized ladder type compound **2OD-TTIFDK** was carried out via conventional Stille cross-coupling reaction by reacting **IFDK-Br2** and **2** in DMF using $Pd(PPh_3)_2Cl_2$ catalyst in 31% yield. Since the solubility of **IFDK-Br2** was very low in common organic solvents, the success of this reaction relies on using highly polar solvent (DMF) at high temperature (125 °C). During the course of this reaction, the coupling of the first π-donor moiety having 2-OD chain enhances the solubility of the mono-coupled adduct significantly so that the second coupling proceeds more easily. Dicyanovinylene functionalized molecule, **2OD-TTIFDM**, was synthesized via Knoevenagel condensation between **2OD-TTIFDK** and malononitrile in the presence of pyridine and $TiCl_4$ in 59% yield. Thanks to the presence of swallow-tailed 2-OD alkyl substituents,

novel D-A-D molecules were purified by using flash column chromatography with chloroform because of their high solubility ($CHCl_3$, THF, Toluene, etc.). The good solubilites of the new molecules also enable the fabrication of OFETs via solution-processing. The intermediate's and final products' chemical structures and degree of purities were confirmed via $^1H/^{13}C$ NMR (Figures 2.2.2.3.1–2 and 2.2.2.4.1–2), mass spectroscopy (MALDI-TOF) (Figures 2.2.2.3.3–2.2.2.4.3), elemental analysis, and ATR-FTIR (Figure 2.3.1.2). Based on thermogravimetric analysis (TGA), both compounds exhibited good thermal stabilities with onset decomposition temperatures over 350 ˚C (Figure 2.3.1.3). Differential scanning calorimetry (DSC) measurements of **2OD-TTIFDK** and **2OD-TTIFDM** exhibited high-temperature endotherms at 218 ˚C and 320 ˚C, respectively, which are in accord with the conventional melting temperature measurements (Figure 2.3.1.3-B). Surprisingly, higher-energy endothermic thermal transitions (179/208 ˚C for **2OD-TTIFDK** and 209 ˚C for **2OD-TTIFDM**) were observed for both compounds prior to the major melting process, which is typical characteristics of liquid-crystalline materials.[55] On cooling, the DSC traces of both compounds displayed the same behavior of their heating cycle. Although the π-skeleton remains the same for both compounds, the melting temperature significantly increases (ΔT_m = +102 ˚C) when the functional group is changed from carbonyl ("C=O" in **2OD-TTIFDK**) to dicyanovinylene ("$C=C(CN)_2$" in **2OD-TTIFDM**). This indicates more effective cohesive forces in the solid-state packing for the latter molecule, which is likely a combined result of larger local/molecular dipole moments and enhanced dipole-dipole/π-π interactions as a result of stronger donor-acceptor characteristics. When compared with our previously reported compound, **2OD-TIFDKT** (Figure 2.3.1.4.),[49] the introduction of additional thiophenes at molecular termini significantly increased T_m by ~80 ˚C in **2OD-TTIFDK** as a result of enhanced π-core rigidity.

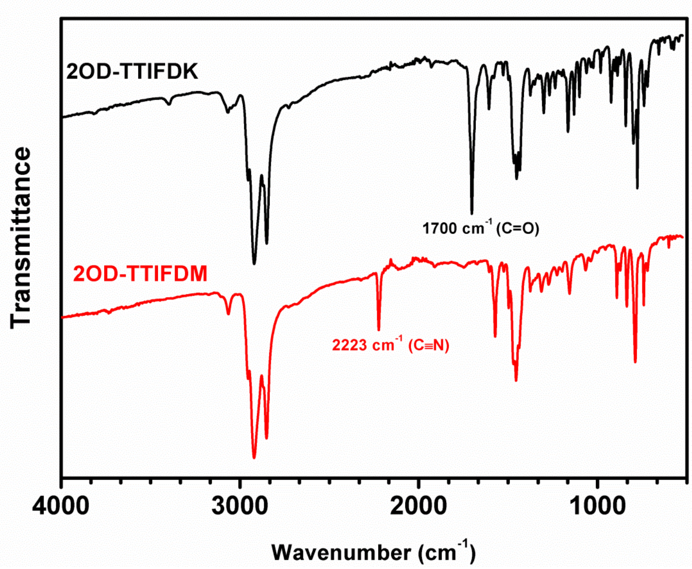

Figure 2.3.1.2 FT-IR Spectra of the semiconductors **2OD-TTIFDK** and **2OD-TTIFDM** showing C=O (1700 cm^{-1}) and C≡N (2223 cm^{-1}) stretching vibrational peaks.

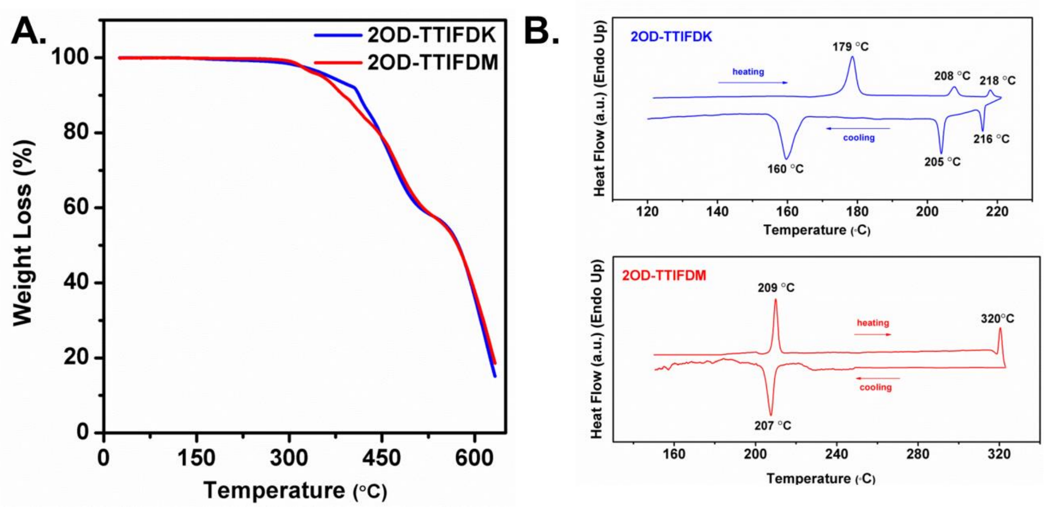

Figure 2.3.1.3 Thermogravimetry(TGA) and differential scanning calorimetry (DSC) measurements of **2OD-TTIFDK** and **2OD-TTIFDM** semiconductors with 10°C/min heating rate under N$_2$.

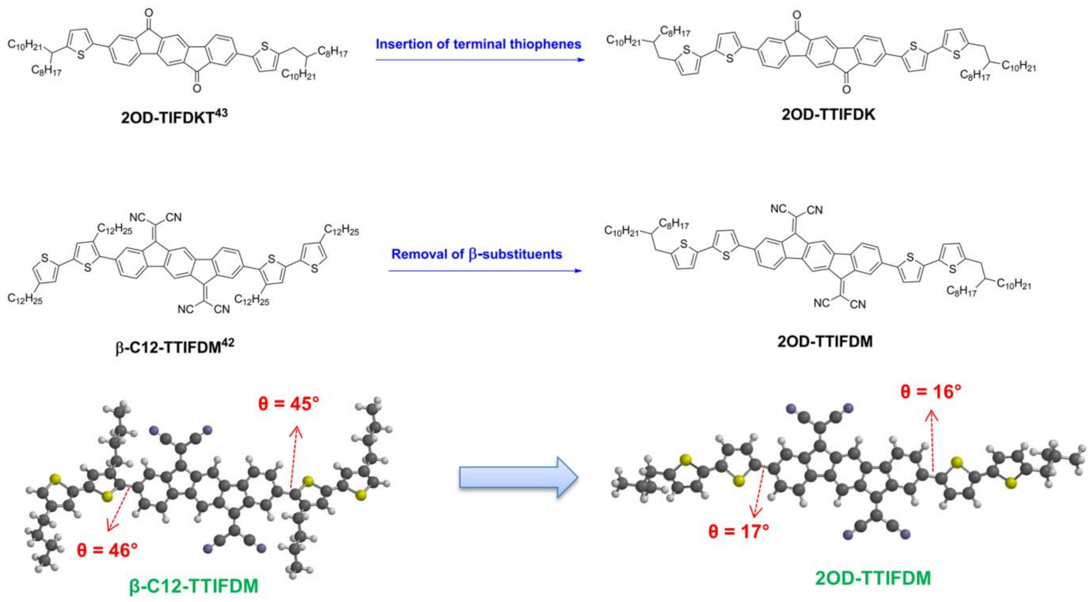

Figure 2.3.1.4 The chemical structures of **β-C12-TTIFDM**[42] and **2OD-TIFDKT**[43].

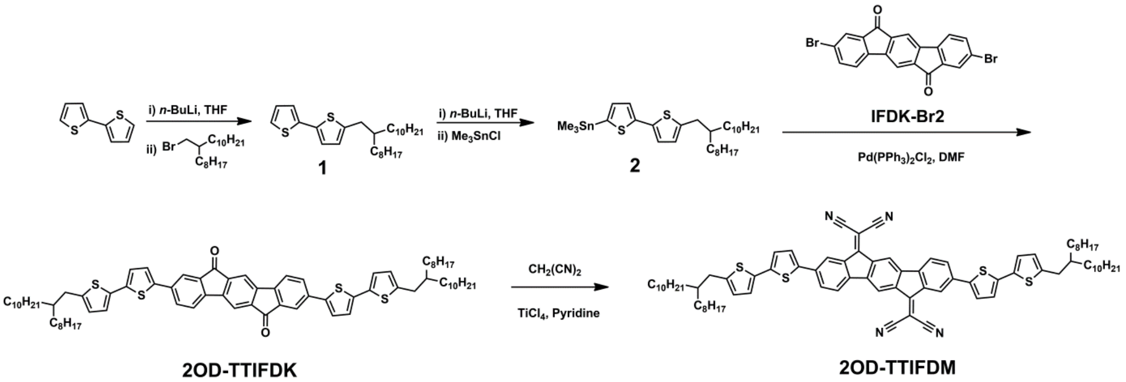

Figure 2.3.1.5 Synthesis of **2OD-TTIFDK** and **2OD-TTIFDM**.

As shown in Figure 2.3.1.6, when the concentrations of **2OD-TTIFDK** and **2OD-TTIFDM** in $CDCl_3$ increased from 1.0 mg/mL to 16.0 mg/mL, the chemical shifts of the aromatic and α-aliphatic protons moved upfield ($-\Delta\delta = 0.1–0.4$ ppm), indicating the presence of shielding effect. This shielding is due to enhanced electron-density on individual protons in consequence of molecular packing in organic solvents by intermolecular π-π stacking and van der Waals interactions. The aromatic protons that show chemical shifts originated both from **IFDK/IFDM** π-cores and bithiophene units, as well as the *alpha*-methylene proton (Ar-$\underline{\mathbf{CH_2}}$-$CH(C_8H_{17})C_{10}H_{21}$) adjacent to the thiophenes, indicating that all these protons are involved in the intermolecular interactions in the molecular stacks. The aromatic peaks were broadened with increasing concentration, which further supports the stacking model since intermolecular attractions widen the local electronic profile around each proton. Similar stacking behaviors were observed for a number of π-conjugated small molecules in the literature.[56–58] This indicates the existence of favorable intermolecular interactions for the present D-A-D π-cores even in the solution-phase, which may potentially render the formation of favorable supramolecular architecture after solvent removal in the solid-state (*vide infra*).

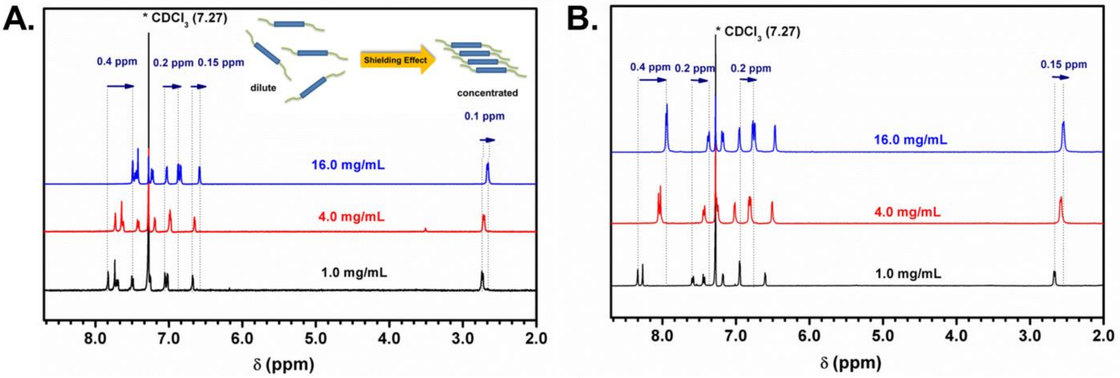

Figure 2.3.1.6 The concentration dependent ^{1}H NMR spectra of **2OD-TTIFDK** (A) and **2OD-TTIFDM** (B) in $CDCl_3$. Inset is the schematic model of molecular stacking in solution as a result of concentration. (The blue and green units represent π-backbone and flexible hydrocarbon chains, respectively.)

2.3.2 Optical and Electrochemical Properties

UV-vis absorption spectra (Figure 2.3.2.1 A and B) of **2OD-TTIFDK** and **2OD-TTIFDM** in dichloromethane solutions exhibit similar higher energy maxima at 410 nm and 400 nm, respectively, corresponding to π-π* transitions of the bithiophene-indeno[1,2-b]fluorene core, which remains the same for both compounds although the functional groups are different. However, lower-energy peaks appear at 568 nm and 740 nm for **2OD-TTIFDK** and **2OD-TTIFDM**, respectively, reflecting the differences in the chemical nature of carbonyl *vs.* dicyanovinylene functional groups. Therefore, these relatively weaker lower-energy transitions are most likely to be governed by the functional groups and originates from symmetry forbidden n-π* transitions.[59,60] By using the low-energy absorption edges, the optical energy gaps in solution were determined which was 1.89 eV for **2OD-TTIFDK** and 1.31 eV for **2OD-TTIFDKM**. From dilute solution to thin-film, both compounds exhibit significant bathochromic shifts (Δλ = 16–216 nm) and reductions in optical band gaps which reveals planarization of molecule backbone and improved interactions of π-π stacking/donor-acceptor in the solid-state. The solid-state optical band gaps are estimated as 1.65 eV for **2OD-TTIFDK** and 1.21 eV for **2OD-TTIFDM**, which are, to the best of our knowledge, among the lowest in the literature for π-conjugated small molecules. It is noteworthy that the optical band-gap and absorption maxima observed for the present compound, **2OD-TTIFDM**, is ~0.15 eV smaller and ~30 nm red-shifted, respectively, compared to those of structurally related compound, **β-C12-TTIFDM** (1.44 eV; λ_{max} = 410, 711 nm).[48] This is due to repositioning of the hydrocarbon chains from *β*- to *α,ω*-positions (Figure 2.3.1.4.) in the new semiconductor, which minimizes the inter-ring twists between donor and acceptor units ($\theta_{Ph\text{-}Th}$ = 45-46° → 16-17°) and further extends the π-conjugation on the present compound. This is found to be very advantageous to the charge carrier mobilities in the corresponding OFET devices (*vide infra*).

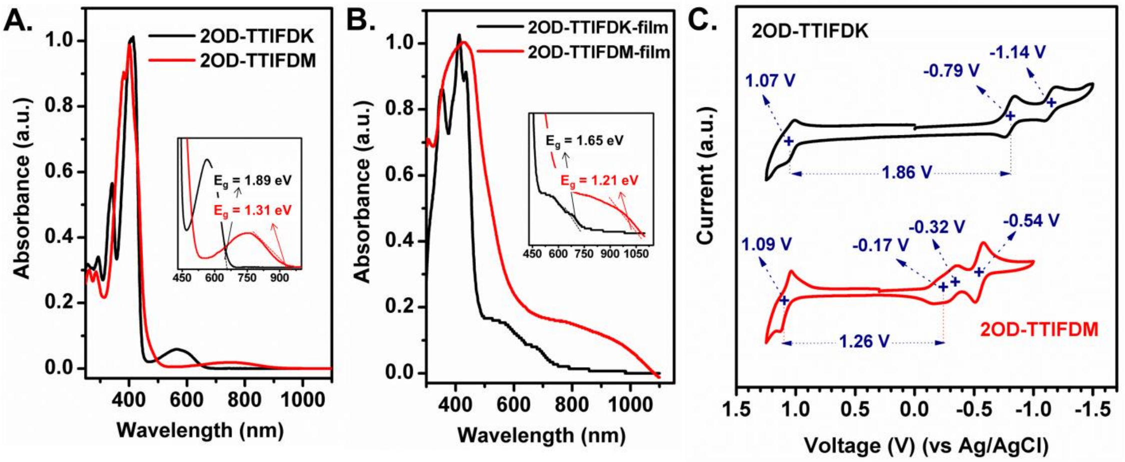

Figure 2.3.2.1 For **2OD-TTIFDK** and **2OD-TTIFDM** molecules, (A) Optical absorption in dichloromethane solution, (B) Optical absorption as thin-films, and (C) Cyclic voltammograms in dichloromethane (0.1M $Bu_4N^+PF_6^-$, scan rate = 50 mV·s^{-1}).

As shown in Figure 2.3.2.1-C, cyclic voltammetry (CV) measurements of **2OD-TTIFDK** and **2OD-TTIFDM** in dichloromethane solutions exhibit reversible oxidation and reduction peaks with the first half-wave potentials located at 1.07 V/-0.79 V and 1.09 V/-0.17 V, respectively. The existence of both oxidative and reductive electrochemical processes with good reversibility indicates the intrinsic redox-stable ambipolar nature of the present compounds. Due to the stronger electron accepting nature of dicyanovinylene in **2OD-TTIFDM** compared to carbonyl in **2OD-TTIFDK**, reduction potential shows significant anodic shift (-0.79 V → -0.17 V) with minimal change on the oxidation potentials. The corresponding HOMO/LUMO energy levels are estimated as -5.47 eV/-3.61 eV for **2OD-TTIFDK** and -5.49 eV/-4.23 eV for **2OD-TTIFDM**, using Ag/AgCl (reference electrode)vacuum level energy as -4.40 eV. These observations are consistent with our theoretical findings (*vide supra*) that for both compounds, HOMOs are delocalized along the same molecular backbone and LUMOs are localized on the acceptor core functionalities. On the basis of the oxidation and reduction potentials, the electrochemical band gaps for **2OD-TTIFDK** and **2OD-TTIFDM** are estimated as 1.86 eV and 1.26 eV, respectively, which are in perfect agreement with the optical band gaps. Based on the molecular orbital energetics and low band gaps, the HOMO (-5.47- -5.49 eV) and LUMO (-3.61- -4.23 eV) energies of the current compounds should favor concurrent electron and hole injection/transport (ambipolarity) in the corresponding thin-films. Specifically, the LUMO level of **2OD-TTIFDM** is highly favorable for ambient-stable electron-transport.

2.3.3 Field-Effect Transistor and Complementary-like Inverter Fabrication and Characterization

Top-contact/bottom-gate (TC/BG) OFETs were fabricated by solution-shearing 30-60 nm thick films of **2OD-TTIFDK** and **2OD-TTIFDM** on PS-brush treated n^{++}-Si/SiO_2(300 nm) substrates to achieve favorable semiconductor-dielectric interfaces with higher semiconductor film quality and better control on the microstructure/morphology, as compared to conventional solution-based methods such as drop casting and spin coating.[61,62] For both semiconductors, the most ideal solution-shearing condition was identified as applying 1.0 mg/mL (in chlorobenzene) semiconductor formulations on substrates maintained at 50-60 ˚C at a shearing speed of ~1.0 mm/min. OFET devices were characterized under positive and negative gate biases in ambient and under vacuum to explore the ambipolarity, device performance, and ambient stability. Typical transfer and output curves are shown in Figures 2.3.3.1-5, and the corresponding OFET data are summarized in Table 2.3.3.1.

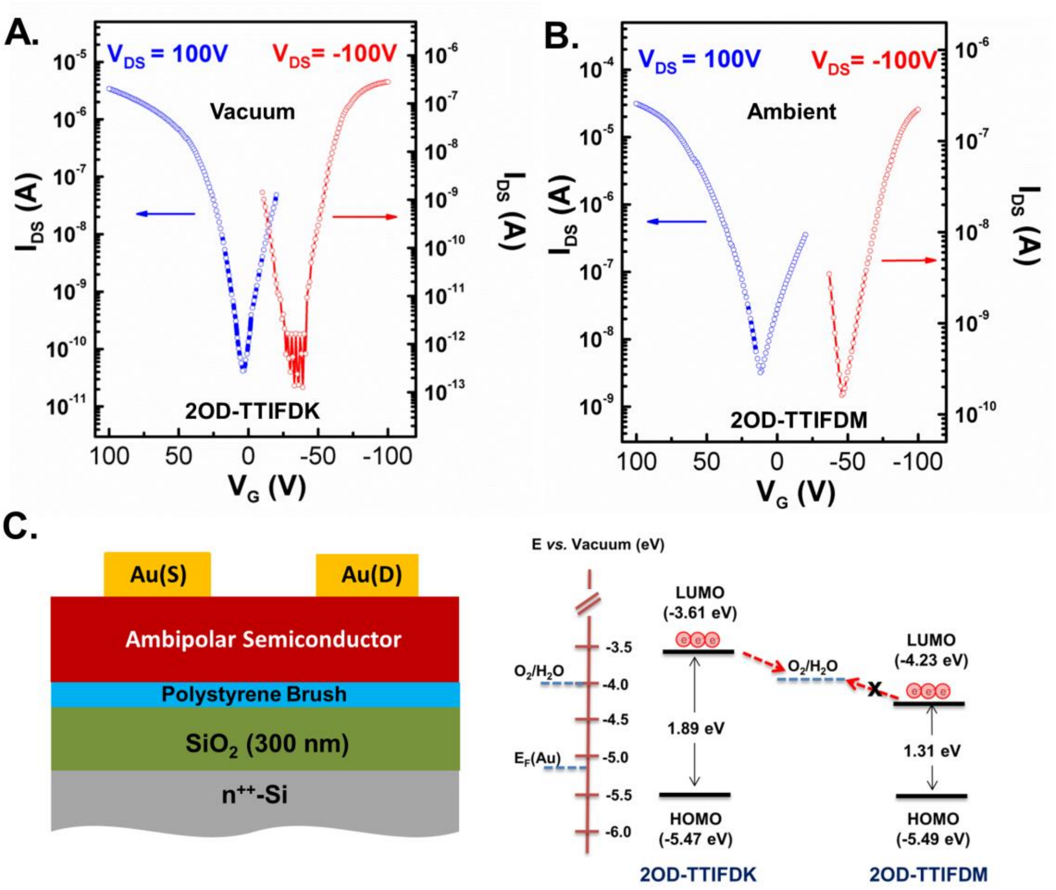

Figure 2.3.3.1 (A, B) Ambipolar (P-channel (in red) and N-Channel (in blue)) transfer curves of the OFET devices based on solution-sheared thin-films of **2OD-TTIFDK** and **2OD-TTIFDM**, and (C) Top-contact/bottom-gate OFET device structure and the band lineups of the molecular orbital energy levels with respect to O_2/H_2O electrochemical redox couple at the air-thin film interface.

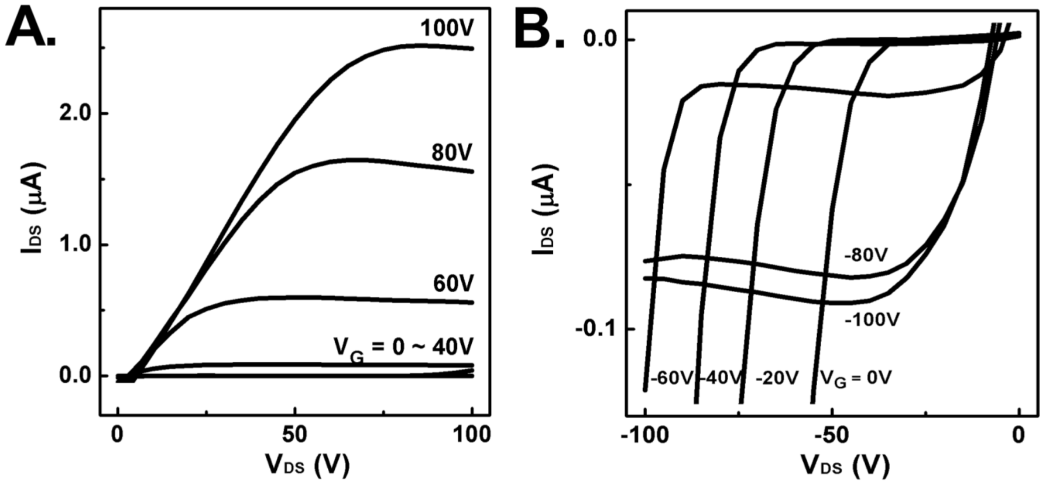

Figure 2.3.3.2 N-type (A) and P-type (B) output curves of the OFET devices fabricated with solution-sheared **2OD-TTIFDK**.

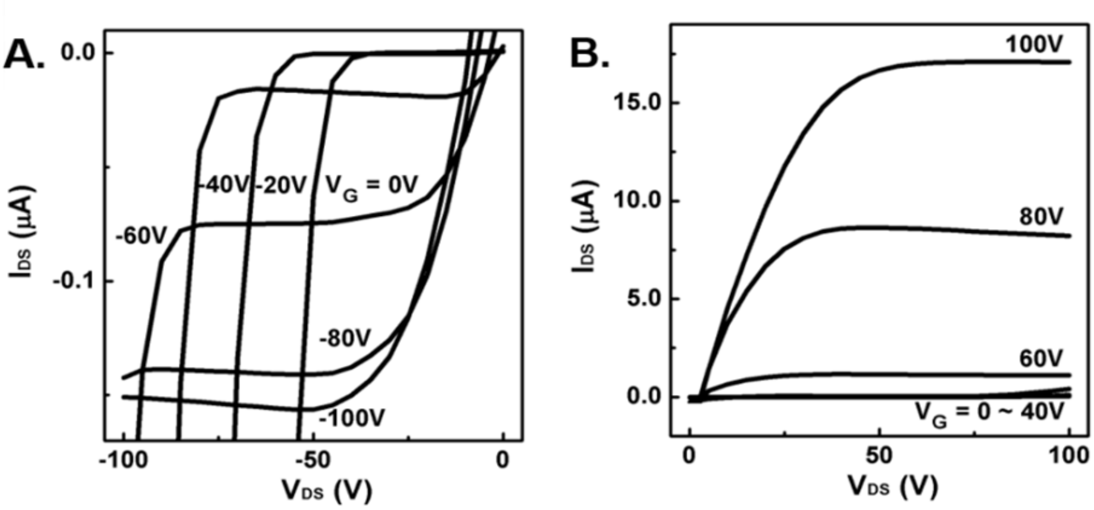

Figure 2.3.3.3 P-type (A) and N-type (B) output curves of the OFET devices fabricated with solution-sheared **2OD-TTIFDM**.

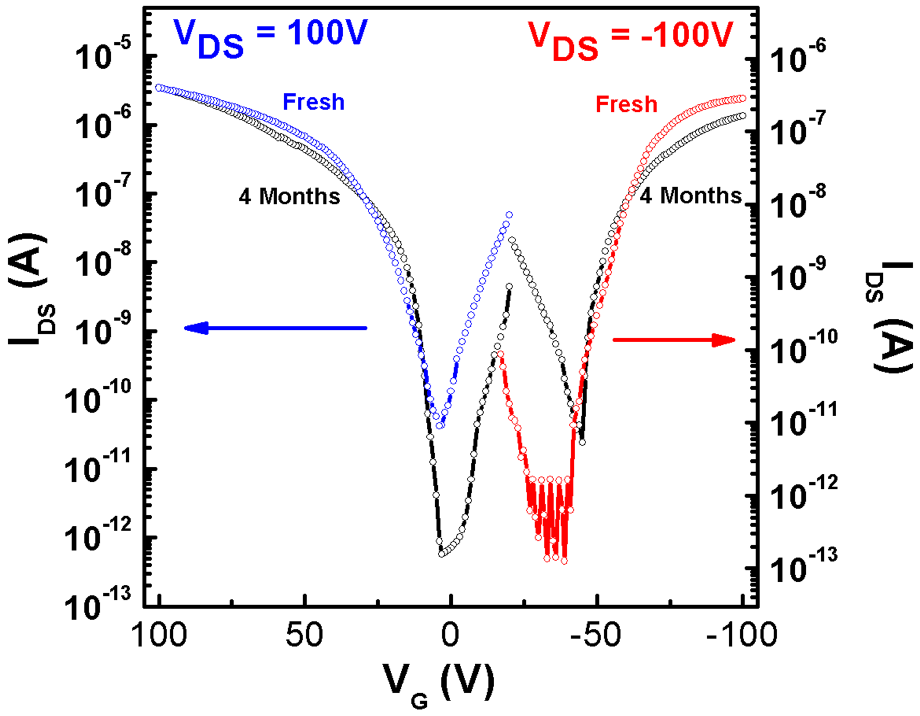

Figure 2.3.3.4 Transfer curves for fresh **2OD-TTIFDM**-based OFET devices (red and blue line) and after 4 months storage in ambient (black line).

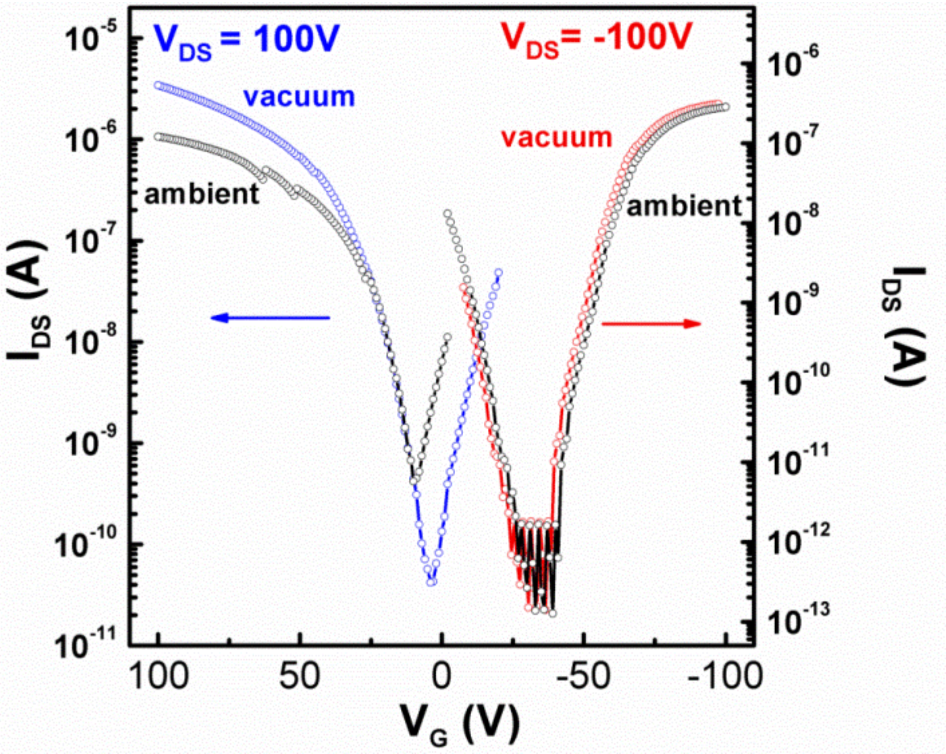

Figure 2.3.3.5 P-type and N-type transfer curves measured under vacuum (red and blue lines) and in ambient conditions (black lines) for the OFET devices fabricated with solution-sheared **2OD-TTIFDK**.

As expected from the optical/electrochemical and theoretical characterizations (*vide supra*), all OFET devices fabricated with the current semiconductors, **2OD-TTIFDM** and **2OD-TTIFDK**, were found to exhibit typical ambipolar characteristics. This indicates intrinsic ambipolar semiconducting nature of the present compounds and can be attributed to their low solid-state band gaps (1.21-1.65 eV), which render both HOMO and LUMO levels energetically accessible for hole and electron injection/transport, respectively. Consistent with its highly stabilized LUMO energy level of -4.23 eV, **2OD-TTIFDM** is found to be perfectly ambient-stable as semiconductor thin-film in OFETs with electron and hole mobilities of 0.13 $cm^2/V \cdot s$ and 0.01 $cm^2/V \cdot s$, respectively, and I_{on}/I_{off} ratios of ~10^3–10^4 in ambient conditions (Figure 2.3.3.1.). These devices are found to exhibit negligible variations in transistor characteristics after few months of storage in ambient, showing prolonged stability of the corresponding semiconductor thin-films (Figure 2.3.3.4.). When the semiconductor performance of **2OD-TTIFDM** is compared with that of structurally related **β-C12-TTIFDM**[48] (Figure 2.3.1.4.), which includes additional linear alkyl chains at thiophenes' β-positions, two orders of magnitude (×100) higher electron ($\mu_e = 1 \times 10^{-3}$

$cm^2/V\cdot s \rightarrow 0.13\ cm^2/V\cdot s$) and hole ($\mu_h = 1\times10^{-4}\ cm^2/V\cdot s \rightarrow 0.01\ cm^2/V\cdot s$) mobilities were achieved with the current semiconductor, **2OD-TTIFDM**. The substantial mobility improvements observed for the new semiconductor probably reflects a combination of D-A-D π-core planarization as a result of reducing inter-ring D-A twists (*vide supra*) and improved thin-film microstructure/morphology due to the solution-shearing process. From a structural design standpoint, in the development of ambipolar small molecules employing donor-acceptor linkages, we can suggest that it's important to minimize the inter-ring twists between donor and acceptor units. On the other hand, due to its relatively higher LUMO energy level of -3.61 eV, OFETs fabricated with **2OD-TTIFDK** were only active under vacuum; they exhibit highly balanced ($\mu_e/\mu_h \sim 2$) ambipolar behavior with mobilities of 0.02 $cm^2/V\cdot s$ (for *n*-channel) and 0.01 $cm^2/V\cdot s$ (for *p*-channel) with $I_{on/off}$ ratios of $\sim10^5$–10^6, respectively. When **2OD-TTIFDK**-based OFETs were measured in ambient conditions, although *p*-channel performance remained at the same level, *n*-channel performance showed significant initial drop (×100) and eventually became inactive (Figure 2.3.3.5.). The transition of electron transport from being unstable to ambient-stable was clearly observed for the present semiconductors when the functional group was changed from *carbonyl* to *dicyanovinylene*, even though the π-backbone (bithiophene-indeno[1,2-b]fluorene-bithiophene) remains the same. This indicates the importance of molecular orbital energetics stabilization for ambient-stable electron-transport in semiconductor thin-films and an electrochemical threshold exists between -3.6 eV and -4.2 eV. This is consistent with earlier reports, and corresponds to a required stabilization of LUMO energy level against electrochemical trapping by O_2-H_2O redox couple.[48,63] To the best our knowledge, the OFET characteristics of **2OD-TTIFDM** are among the best solution-processed, small molecular ambipolar performances in terms of reasonably balanced and ambient-stable charge carrier mobilities. It's noteworthy that further device structure optimizations such as using ferroelectric dielectrics[20] and adding graphene oxide (GO)[64] or single-walled carbon nanotube (SWNT)[65] interlayers can be employed to further balance electrical characteristics of hole- *vs* electron-transport with the current ambipolar semiconductors.

Table 2.3.3.1 Electrical Performance of OFETs based on **2OD-TTIFDK** and **2OD-TTIFDM** fabricated within the scope of this thesis.[a]

Material	***N*-channel**			***P*-channel**		
	μ_e (cm^2/V·s)	**V_T (V)**	**I_{on}/I_{off}**	**μ_h (cm^2/V·s)**	**V_T (V)**	**I_{on}/I_{off}**
2OD-TTIFDK	0.02±0.002	34±3	1.4×10^5	0.01±0.001	-55±4	2.2×10^6
2OD-TTIFDM	0.13±0.012	13±2	1.0×10^4	0.01±0.002	-33±2	1.1×10^3

[a] The OFETs based on **2OD-TTIFDK** and **2OD-TTIFDM** were measured under vacuum and in ambient, respectively.

Complementary-like inverter is an essential building block of integrated circuits for data processing, and it typically requires the fabrication of separate *p*- and *n*-channel transistors. However, when an ambipolar semiconducting material is used, only a single layer of organic semiconductor is required without the need for separate patterning of unipolar *p*- and *n*-channel semiconductors. Therefore, given the promising high-performance, well-balanced ambipolar OFET characteristics of the new semiconductors, complementary-like inverters were fabricated from **2OD-TTIFDK** or **2OD-TTIFDM** semiconductor solutions and characterized on single substrates using two identical ambipolar transistors with the shared gold electrode (Figure 2.3.3.6-inset). As shown in Figures 2.3.3.6 and 2.3.3.7, complementary-like inverters based on **2OD-TTIFDK** and **2OD-TTIFDM** operated well under vacuum and in ambient, respectively, in the first and third quadrants with sharp switchings of V_{OUT}'s at supplied voltages (V_{DD}) of +100 and -100 V, respectively. The voltage gain is calculated from $|dV_{OUT}/dV_{IN}|$, where V_{OUT} and V_{IN} are the output and input voltages, respectively. The ability of the current inverters to operate in both quadrants is the specific advantage of having ambipolar OFETs.[66,67] For **2OD-TTIFDK**-based inverters, very high voltage gain of 80 V/V was achieved at positive V_{IN} along with a maximum gain of 28 V/V at negative V_{IN}. To the best of our knowledge, the high voltage gain in the first quadrant is among the highest voltage gains achieved with a solution-processed, single-component ambipolar semiconductor.[68–70] High voltage gain from sharp voltage inversion demonstrates the reliability of the current inverter devices, and can be attributed to the highly balanced ambipolar charge-transport behavior of **2OD-TTIFDK** (*vide supra*)·[71] On the other hand, inverters based on ambient-stable semiconductor, **2OD-TTIFDM**, were characterized in ambient, and they exhibited good voltage gains of 30 V/V (Figure 2.3.3.7.). Our results show that the current solution-processable ambipolar small molecules are ideal semiconductors not only for ambipolar OFETs but also for single-component CMOS-like organic circuits. However, it's noteworthy that the observed Z-shaped voltage transfer characteristics (VTC) for both semiconductors are typical for unoptimized ambipolar transistor-based inverters, since both the pull-up (*p*-channel) and pull-down (*n*-channel) transistors cannot be completely switched off at low and high V_{IN}'s.[64] These features will cause limited noise margin and large static power consumption, and further inverter device optimizations such as semiconductor film doping or incorporating interlayers are needed to further match charge carrier mobilities (μ) and threshold voltages (V_T) in the *p*- and *n*-channel regions.[65]

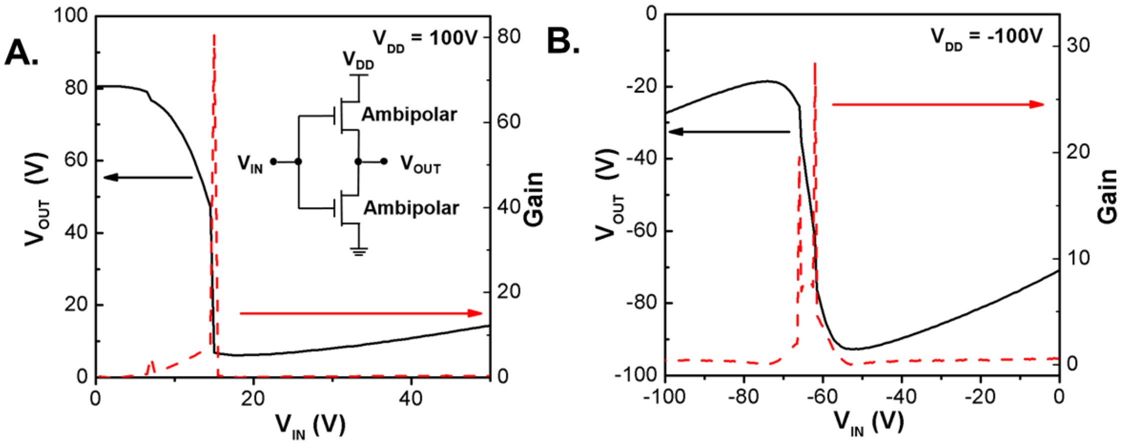

Figure 2.3.3.6 Voltage transfer characteristics (VTC) of a complementary-like inverter fabricated by two identical **2OD-TTIFDK**-based ambipolar transistors in first (A) and third (B) quadrants with supplied voltages of +100 V and -100 V. Inset shows the circuit diagram and the plots of gains ($-dV_{OUT}/dV_{IN}$) are given in red.

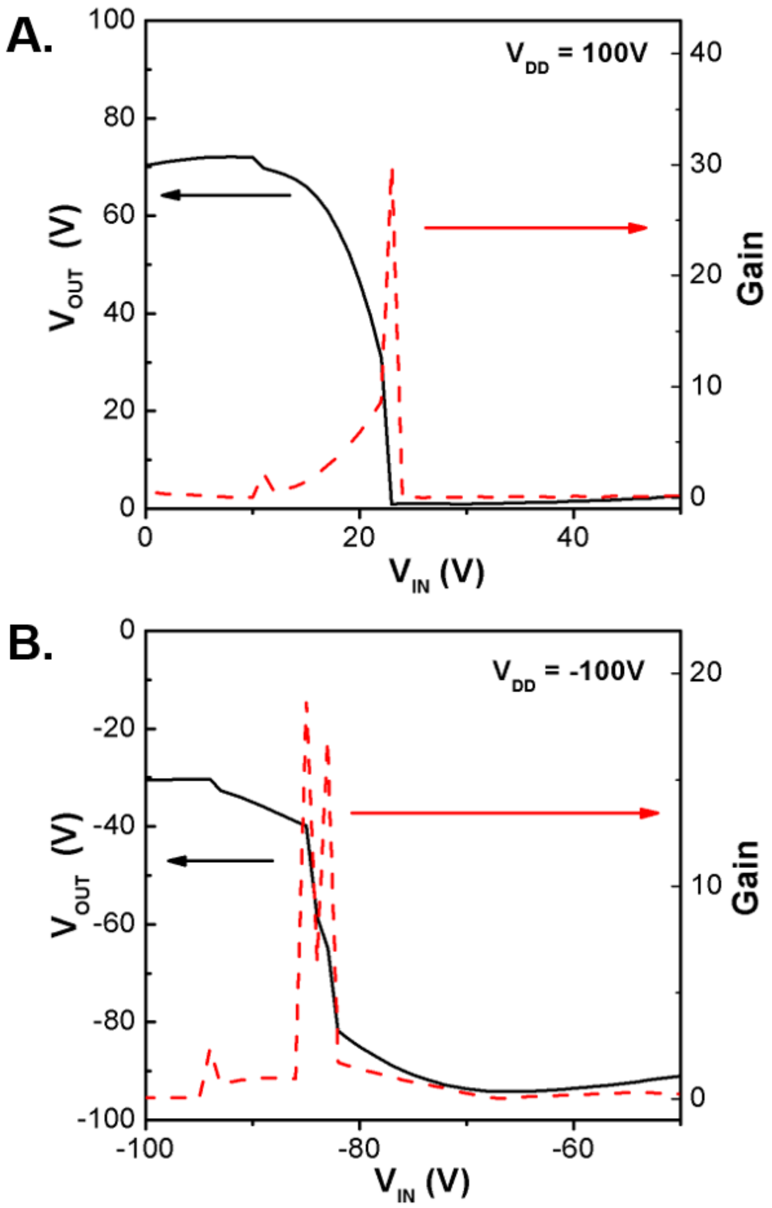

Figure 2.3.3.7 Voltage transfer curves of **2OD-TTIFDM** in first (A) and third (B) quadrants measured in ambient.

2.3.4 Thin-Film Microstructure and Morphology

The microstructural and morphological characteristics of the solution-sheared thin-films of the current semiconductors were investigated by out-of-plane θ-2θ X-ray diffraction (XRD) technique and atomic force microscopy (AFM). As shown in Figure 2.3.4.1., both semiconductor thin-films showed high crystallinity with distinct $(00l)$ peaks, till the third-order along with broad $(0k0)$ peaks. The first-order peak (001) was at $2\theta = 3.05°$ (*d*-spacing = 29.0 Å) for **2OD-TTIFDK** and at $2\theta = 2.37°$ (*d*-spacing = 37.2 Å) for **2OD-TTIFDM**, indicative of the formation of well-organized lamellar microstructure having molecular/alkyl-chain edge-on orientation relative to the dielectric surface. Further weak diffraction peaks were observed at $2\theta = 4.24°$ (001') and 5.34° (001'') for **2OD-TTIFDK**-based thin-film, which do not belong to the primary diffraction family, indicating the existence of additional minor crystalline phases.

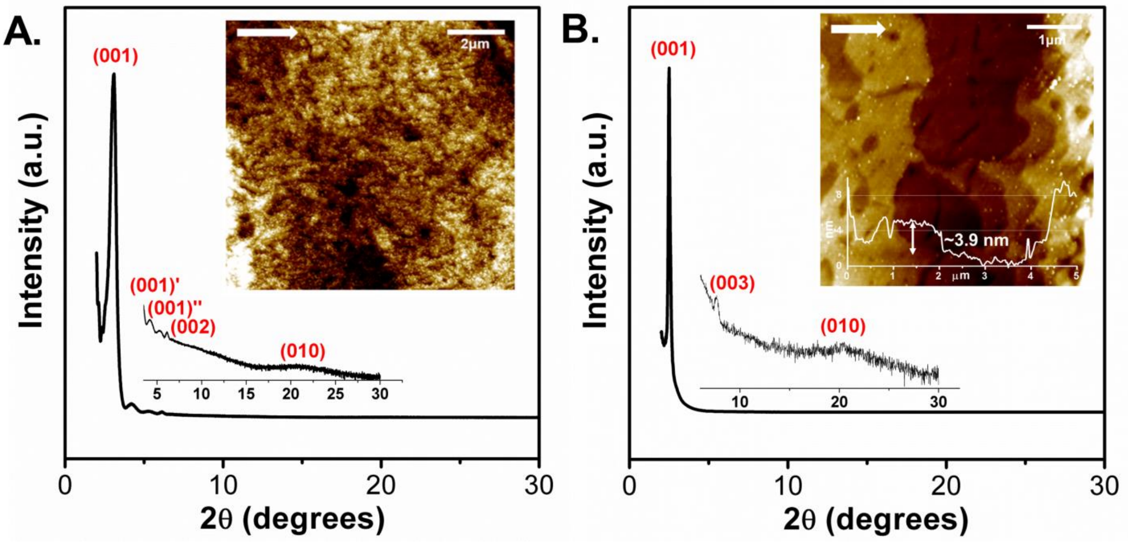

Figure 2.3.4.1 XRD patterns and AFM images (inset) of **2OD-TTIFDK** (A) and **2OD-TTIFDM** (B) thin-films fabricated by solution shearing method. The scale bar denotes 1-2 μm and the arrow shows the shearing direction.

The *d*-spacings for both compounds are shorter than the computed molecular lengths (~57.0 Å) with fully extended (all-trans conformation) alkyl chains. This indicates that significant alkyl chain interdigitation and/or molecular tilting from the substrate normal are likely to occur in thin-film phases. Considering that the alkyl chains remain the same for both semiconductors, the larger *d*-spacing observed for **2OD-TTIFDM** reflects more vertically oriented molecular π-cores relative to the dielectric surface, probably as a result of stronger intermolecular interactions between D-A-D π-cores (*vide supra*). **2OD-TTIFDM** thin-film exhibited much stronger (001) diffraction peak intensity (×7 for the same film thickness) with smaller FWHM (full width at half maximum) (~0.20° *vs.* ~0.35°) when compared with that of **2OD-TTIFDK**. This shows that **2OD-TTIFDM** thin-films have higher crystallinity with larger mean crystallite size.[72] Broad diffraction peaks observed at $2\theta \sim 22^{\circ}$ (010) were ascribed to π-π stacking interactions with distances of ~4.1 Å between molecular backbones, which is somewhat larger than the typical π-π stackings observed for oligo-/polythiophenes (3.4-3.9 Å).[48,73,74] This points to relatively weaker π-π stacking interactions for the current semiconductors and it can be attributed to the presence of sterically bulky, swallow-tailed 2-octyldodecyl substituents, which may preclude the π-cores from approaching each other effectively. AFM characterizations provide more information on the morphological aspects of the current films, and, therefore, allow us to better understand the correlations with the electrical performances. Uniform morphologies have been observed for both films thanks to surface roughness below 4-5 nm for 10×10 μm scan areas. Although **2OD-TTIFDK** films exhibited small highly-interconnected isotropic spherulites (~100-200 nm diameter sizes), **2OD-TTIFDM** films revealed two-dimensional micron-size (~1-2 μm) plate-like grains of terraced islands with step-heights of ~3.9 nm, which corresponds to the *d*-spacing measured from the XRD characterization (~3.7 nm). The observed highly crystalline and edge-on π-oriented microstructure, and layer-by-layer grown 2-D morphology of **2OD-TTIFDM** film favors efficient charge-transport in OFETs. Furthermore, when these favorable microstructural/morphological features are compared with those of **2OD-TTIFDK**-based thin-film, it seems to significantly enhance the field-effect electron mobility (×6) with minimal influence on the field-effect hole mobility. This shows that thin-film morphological and microstructural characteristics may have totally different effects on electron and hole charge-transport characteristics of molecular solids.

2.4 CONCLUSION

Two new solution-processable ambipolar small molecules, **2OD-TTIFDK** and **2OD-TTIFDM**, have been designed, synthesized and fully characterized. The new semiconductors having strong D-A-D π-architectures employ ladder-type π-acceptors of **IFDK/IFDM** and α-substituted bithiophene π-donors, which results in ultralow band gaps of 1.21-1.65 eV. The HOMO/LUMO frontier orbital energies of the new molecules (-5.47/-3.61 eV for **2OD-TTIFDK** and -5.49/-4.23eV for **2OD-TTIFDM**) are found to be highly favorable for balanced ambipolar charge-transport and ambient-stability for **2OD-TTIFDM**. The resulting bottom-gate/top-contact OFET devices fabricated by solution-shearing **2OD-TTIFDM** show clear ambipolar characteristics in ambient with reasonably balanced carrier mobilites of 0.13 $cm^2/V\cdot s$ for electron and 0.01 $cm^2/V\cdot s$ for hole with I_{on}/I_{off} ratios of ~10^3-10^4. **2OD-TTIFDK**-based OFETs exhibit ambipolarity under vacuum with highly balanced (μ_e/μ_h ~ 2) electron and hole mobilities of 0.02 $cm^2/V\cdot s$ and 0.01 $cm^2/V\cdot s$, respectively with I_{on}/I_{off} ratios of ~10^5-10^6. Most importantly, complementary-like inverters were demonstrated based on the new ambipolar small molecules, which showed sharp signal switching with very high gains of up to 80. When the charge transport stability of the current semiconductors are compared, our observations show that the ambient-stability of charge-transport in ambipolar semiconductors is governed mainly by the stabilization of conducting electrons in LUMO energy level. To the best of our knowledge, the current D-A-D π-structures are among the best performing ambipolar small molecules for OFET and complementary-like inverter devices. Our findings clearly provide an efficient approach for the preparation of ultralow band-gap small molecules as ambient-stable and solution-processable ambipolar semiconductors for various organic optoelectronic technologies including CMOS-like integrated circuits.

Chapter 3

A Solution-Processable Liquid-Crystalline Semiconductor for Low-Temperature Annealed Air-Stable N-Channel Field-Effect Transistors

3.1 Introduction

The theoretical design and synthetic development of organic semiconductors having π-conjugated molecular structures have emerged in the past few decades since the first reports of organic field-effect transistors (OFETs) based on intrinsic molecular semiconductors of Lutetium complexes in the late 1980s.[1,2] Small molecules offer great benefits due to their limited π-extended core, which can be readily modified with a variety of functional groups to fine tune their optoelectronic and physicochemical properties.[3,4] In addition, the solubility, synthetic reproducibility, and final purity levels of small molecules can be superior to those of macromolecules and polymers, which is very crucial for the realization of low-cost and high-performance plastic optoelectronics.[5–9] To this end, numerous molecular semiconductors have been developed and characterized in a wide range of optoelectronic applications including OFETs,[10] organic photovoltaics (OPVs)[11], and organic light-emitting diodes (OLEDs)[12] and transistors (OLETs)[13]. It is noteworthy that, among these applications, π-conjugated small molecules have been even commercialized in active-matrix OLED displays as emissive and hole/electron transporting/blocking layers.[14] Among the molecular semiconductors studied to date, small molecules with electron-deficient π-architectures and low LUMO energy levels constitute an important class of materials for air-stable electron transport in p-n junctions, bipolar transistors, and organic complementary-like circuitry (CMOS).[15,16] In addition, π-deficient small molecules can function as non-fullerene electron acceptors for use in bulk-heterojunction organic solar cells.[17]

In optoelectronic devices, with regard to the charge carrier injection from environmentally stable metallic electrodes such as Au and Pt (φ ~ -5.0 - -5.9 eV), inorganic oxides such as indium tin oxide (ITO) (φ ~ -4.2- -4.9 eV), and polymeric conductors such as poly(3,4-ethylenedioxy)thiophene/poly(styrenesulfonate) (PEDOT/PSS) (φ ~ -5.0 eV), the electronic energy levels of typical π-building blocks (benzene, thiophene, naphthalene, etc.) are suitable only for hole injection/transport (*p*-channel semiconductor).[18] Therefore, most of the initially developed semiconductors in this field exhibited mainly *p*-channel charge-transport.[16] Although later studies have revealed that majority charge-carrier sign can be inverted from *p*-channel to *n*-channel by functionalizing π-cores with electron-withdrawing groups,[19] air-stable and solution-processable *n*-channel molecular semiconductors are still scarce. Introducing lipophilic alkyl chains ($-C_nH_{2n+1}$) to rigid π-cores has been shown to provide semiconductors good solubility in organic solvents for convenient chemical purification/device fabrication, while still promoting a good molecular ordering in thin-film phase.[20] In addition, flexible alkyl substituents attached to rigid molecular π-backbones may provide thermotropic liquid crystalline characteristics to the semiconductor molecules, which can be used to further optimize their thin-film microstructure and morphology via thermal processes.[21]

To this end, some of us have previously reported a solution-processable *n*-channel molecular semiconductor, **β-DD-TIFDMT** (Figure 3.1.1), based on a donor-acceptor-donor (D-A-D) π-architecture employing a ladder-type indenofluorenebis(dicyanovinylene) (**IFDM**) central acceptor unit and *β*-substituted thiophene terminal donor units. This semiconductor was found to have a low LUMO energy level of -4.32 eV, and the corresponding OFETs based on spin-coated semiconductor films showed air-stable electron mobilities (μ_e's) of up to ~0.1-0.2 $cm^2/V \cdot s$.[20] This π-architecture was one of the early examples of non-quinodial, air-stable *n*-channel semiconductors employing dicyanovinylene ($C=C(CN)_2$) functionality, which has also guided the realization of numerous air-stable semiconductors in the past decade.[22] However, this good mobility was achieved only after annealing spin-coated semiconductor thin-films at 150-200 °C, and μ_e's were found to be ~10^{-3} $cm^2/V\cdot s$ when devices were annealed below 100 °C. For the organic semiconductor thin-film fabrication procedure to be compatible with flexible plastic substrates and underlying organic layers in multilayer devices, low temperature ($T_{annealing}$ < 50-60 °C) post-deposition annealing conditions are always more desirable. Thus, motivated with the earlier promising semiconductor performance of this molecular π-core and to realize good solution-processed μ_e's in air from low-temperature annealed devices, we have envisioned modifying the π-core substitution from *β*- to *α,ω*-positions and introducing branching on the alkyl substituents. The main goals here are to further fine-tune semiconductor physicochemical properties, optoelectronic characteristics, and thin-film microstructure/morphology, which can help us to better understand the effect of substitution on charge-transport properties of this promising D-A-D π-molecular system. In addition, the current design may enhance π-π stacking interactions by minimizing the donor-acceptor dihedral angles between **IFDM** and thiophene units, and can lead to favorable charge-transporting microstructure/morphology at low annealing temperatures (T < 50-60 °C). The formation of a low LUMO energy level on a π-extended core, along with solution-processibility and good electron-transport ability will also pave the way for the new compound to be used as non-fullerene acceptors in BHJ photovoltaic cells. To this end, we have repositioned the 3,3'-alkyl substituents to the 5,5'-positions of the terminal thiophene units, and branching were introduced at 2-positions to yield 2-ethylhexyl ($-CH_2CH(C_2H_5)C_4H_9$) and 2-octyldodecyl ($-CH_2CH(C_8H_{17})C_{10}H_{21}$) alkyl substituents. This approach is expected to benefit the extension of π-conjugation along the molecular backbone while controlling the π-π stacking/donor-acceptor interactions. This way, both molecular solubility in organic solvents and charge-transport ability in thin-film can be well-maintained. To realize this delicate balance has been a conundrum in the past decade for the design of solution-processable, high-mobility *n*-channel semiconductors. In addition, the presence of both rigid π-unit and highly flexible, branched alkyl chains in a symmetric rod-like architecture may result in mesogenic (liquid-crystalline) behavior. Liquid-crystalline (LC) semiconductors can be quite advantageous for charge-transport in optoelectronic devices since they enable the formation of highly ordered nanostructures via molecular self-assembly. If the molecular orientation in the LC phase is matched with the charge-transport direction of a particular optoelectronic device architecture (e.g., "face-on" for OPV/OLED and "edge-on" for OFET)[23], device performances can be further enhanced. On the other hand, since the number of high-mobility organic semiconductors exhibiting liquid-crystalline behavior has been limited in OFETs,[24] the realization of new "thermotropic" LC semiconductors is very valuable to tune thin-film microstructure/morphology via post-deposition thermal annealing processes, which can be used to study and elucidate the crucial relationships between chemical structure, thin film microstructure/morphology and charge-transport.[25]

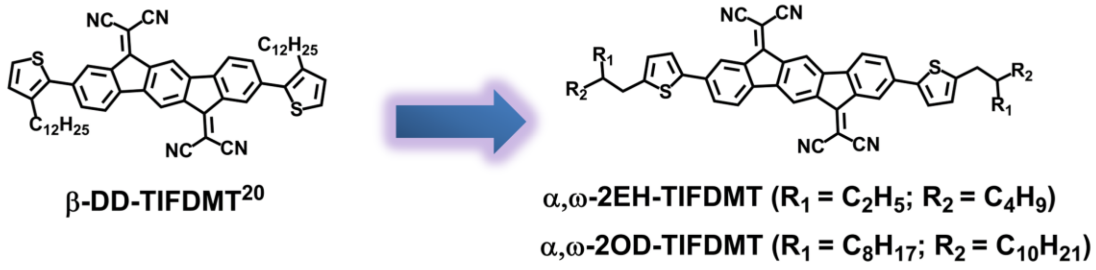

Figure 3.1.1 The chemical structures of **β-DD-TIFDMT**[20], **α,ω-2EH-TIFDMT**, and **α,ω-2OD-TIFDMT** developed in this study.

In this study, we report the design, synthesis, and characterization of two new highly electron-deficient D-A-D type small molecules **α,ω-2EH-TIFDMT** and **α,ω-2OD-TIFDMT** (Figure 3.1.1). While 2-ethylhexyl substitution was found to be inefficient for required solubility, 2-octyldodecyl substitution render **α,ω-2OD-TIFDMT** freely soluble in various solvents such as chloroform, THF, and toluene at room temperature. The chemical characterizations were performed with $^1H/^{13}C$ NMR, MALDI-TOF, elemental analysis, and attenuated total reflection infrared spectroscopy (ATR–FTIR) to prove the chemical structures and final purity levels. Differential scanning calorimetry (DSC) and thermogravimetric analysis (TGA) (T_{onset} = 380 °C) were performed along with melting point apparatus ($T_{c.p.}$ = 230-231 °C) to characterize the thermal properties of the new semiconductor. **α,ω-2OD-TIFDMT** was found to exhibit a liquid-crystalline behavior over a broad temperature range (ΔT = 90-130 °C) with a characteristic fan-shaped texture of a hexagonal columnar phase. UV-Vis absorption and cyclic-voltammetry characterizations showed that **α,ω-2OD-TIFDMT** has low HOMO and LUMO energy levels of -5.64 eV and -4.19 eV, respectively, with a narrow solid-state optical band gap (1.35 eV). The high solubility of **α,ω-2OD-TIFDMT**, endowed by branched α,ω-alkyl substituents, allows the fabrication of bottom-gate/top-contact OFET devices via spin-coating. The devices, which were annealed only at 50 °C, exhibit perfectly air-stable *n*-channel behavior with good electron mobilities of up to 0.11 $cm^2/V \cdot s$ and I_{on}/I_{off} ratios of 10^7-10^8. This indicates two-orders of magnitude (100×) enhancement in charge-transport, as compared to the OFETs based on low-temperature annealed parent semiconductor (**β-DD-TIFDMT**) thin-films, which reflects the result of rational alkyl chain engineering. Atomic-force microscopy (AFM) and out-of-plane θ-2θ X-ray diffraction (XRD) characterizations of these thin-films indicate the formation of highly interconnected, micron-sized (~0.5-1.0 μm sizes) plate-like grains with high crystallinity employing edge-on molecular orientations. Four orders of magnitude (10,000×) decrease in electron mobility was observed when semiconductor thin-films were annealed at LC-state.

3.2 Experimental

3.2.1 Materials and Methods

The chemicals and reagents were purchased from commercial suppliers and used directly unless otherwise noted. Traditional vacuum/nitrogen manifold system was managed, and all the reactions were performed under N_2. By using Bruker 400 spectrometer (^{1}H, 400 MHz; ^{13}C, 100 MHz), ^{1}H/^{13}C NMR spectra were obtained. Elemental analyses were carried out via Leco Truspec Micro. TGA and DSC analysis were recorded under nitrogen atmosphere via Perkin Elmer Diamond with 10 °C/min heating rate. C3 Cell Stand equipped Epsilon potentiostat/galvanostat was used for cyclic voltammetry measurements. Shimadzu UV-1800 spectrophotometer was used for UV-vis absorption measurements. By using BrukerMicroflex LT MALDI-TOF-MS device, MALDI-TOF measurements were recorded. Through Gaussian 09, the calculations of total energy and molecular geometry were performed via density functional theory (DFT) at the B3LYP/6-31G** basis set. [46] The synthesis of 2,8-dibromo-indeno[1,2-b]fluorene-6,12-dione (**IFDK-Br$_2$**). 2-trimethylstannyl-5-(2-ethylhexyl)thiophene, 2-trimethylstannyl-5-(2-octyldodecyl)thiophene, 2,8-bis(5-(2-ethylhexyl)thien-2-yl)indeno[1,2-b]fluorene-6,12-dione and 2,8-bis(5-(2-

octyldodecyl)thiophen-2-yl)indeno[1,2-b] fluorene-6,12-dione were performed according to previously reported procedure. [6]

3.2.2 Synthesis and Characterization

3.2.2.1 2,2'-(2,8-bis(5-(2-ethylhexyl)thiophen-2-yl)indeno[1,2-b]fluorene-6,12 diylidene) dimalononitrile (α,ω-2EH-TIFDMT).

2,8-bis(5-(2-ethylhexyl)thiophen-2-yl)indeno[1,2-b] fluorene-6,12-dione (1) (181.16 mg, 0.270 mmol) and malononitrile (0.25 g, 3.785 mmol) were dissolved in anhydrous chlorobenzene (30 mL) under nitrogen atmosphere. Then, pyridine (0.41 mL, 5.09 mmol) and $TiCl_4$ (0.293 mL, 2.676 mmol) were added and the reaction mixture was heated at 110 °C for 5 h under nitrogen atmosphere. When the resulting reaction mixture was cooled to room temperature for work-up, dark colored crude product precipitated from the reaction mixture. Due to its extremely low solubility in organic solvents, no further purification was performed on this crude material (0.135 g, 65% crude yield).

3.2.2.2 2,2'-(2,8-bis(5-(2-octyldodecyl)thiophen-2-yl)indeno[1,2-b]fluorene-6,12 diylidene) dimalononitrile (α,ω-2OD-TIFDMT).

To a solution of 2,8-bis(5-(2-octyldodecyl)thiophen-2-yl)indeno[1,2-b] fluorene-6,12-dione (2) (0.300 g, 0.297 mmol), malononitrile (0.275 g, 4.164 mmol), and 35 mL of chlorobenzene, pyridine (0.457 mL, 5.651 mmol) and $TiCl_4$ (0.326 mL, 2.974 mmol) were added under nitrogen. Then, and the reaction mixture was heated at 110 °C for 5 h. After the reaction was completed, the reaction mixture was quenched with water. The desired product was extracted into an organic phase by using chloroform. The crude product was obtained via solvent evaporation until dryness which was purified through flash column chromatography with chloroform to give the final product. (0.237 g, 72.2% yield). m.p. 230-231 °C. ^1H NMR (400 MHz, $CDCl_3$): δ 0.89 (m, 6H), 1.28 (s, 31H), 1.59 (s, 4H), 2.75 (d, 2H, J = 8.0 Hz), 6.73 (d, 1H, J = 4.0 Hz), 7.18 (d, 1H, J = 4.0 Hz), 7.49 (d, 1H, J = 8.0 Hz), 7.64 (t, 1H, J = 8.0 Hz), 8.29 (s, 1H), 8.42 (s, 1H). ^{13}C NMR (100 MHz, $CDCl_3$): δ 14.1, 22.6, 26.5, 29.2, 29.8, 31.9, 33.0, 34.8, 39.9, 78.3, 113.0, 117.4, 121.3, 122.8, 124.0, 126.5, 131.0, 134.7, 136.7, 138.4, 139.4, 142.7, 146.5, 159.1. MS(MALDI-TOF) m/z (M^+): calculated. for $C_{74}H_{94}N_4S_2$: 1103.69, found: 1103.12 $[M]^+$. Anal. calculated. for $C_{74}H_{94}N_4S_2$: C, 80.53; H, 8.58; N, 5.08, Found: C, 80.89; H, 8.72; N, 5.32.

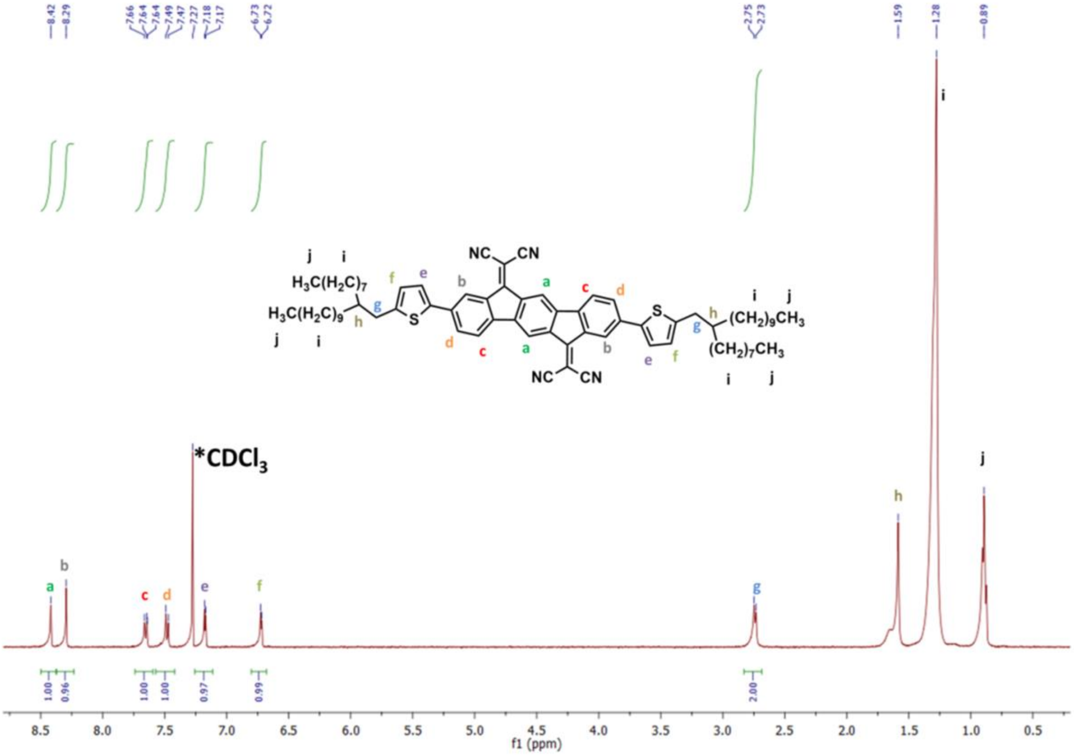

Figure 3.2.2.2.1 ^{1}H NMR spectra of **α,ω-2OD-TIFDMT** measured in $CDCl_3$.

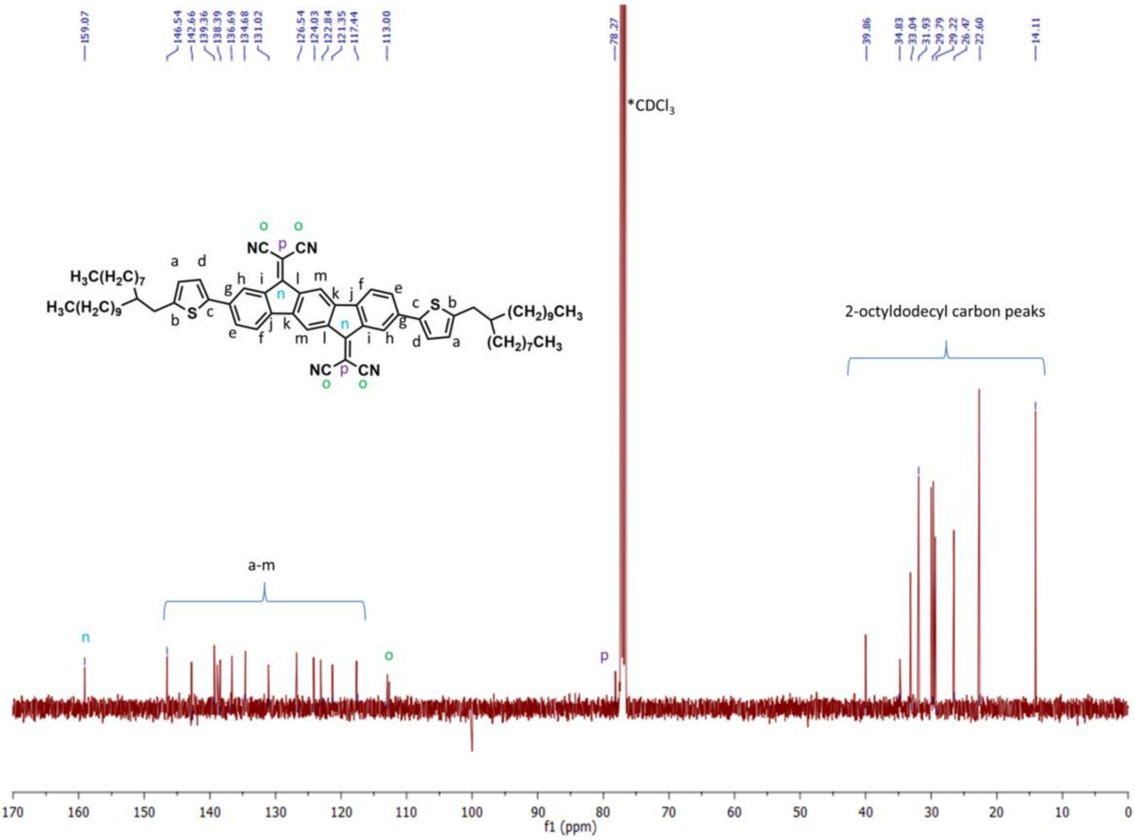

Figure 3.2.2.2.2 ^{13}C NMR spectra of α,ω-**2OD-TIFDMT** measured in $CDCl_3$.

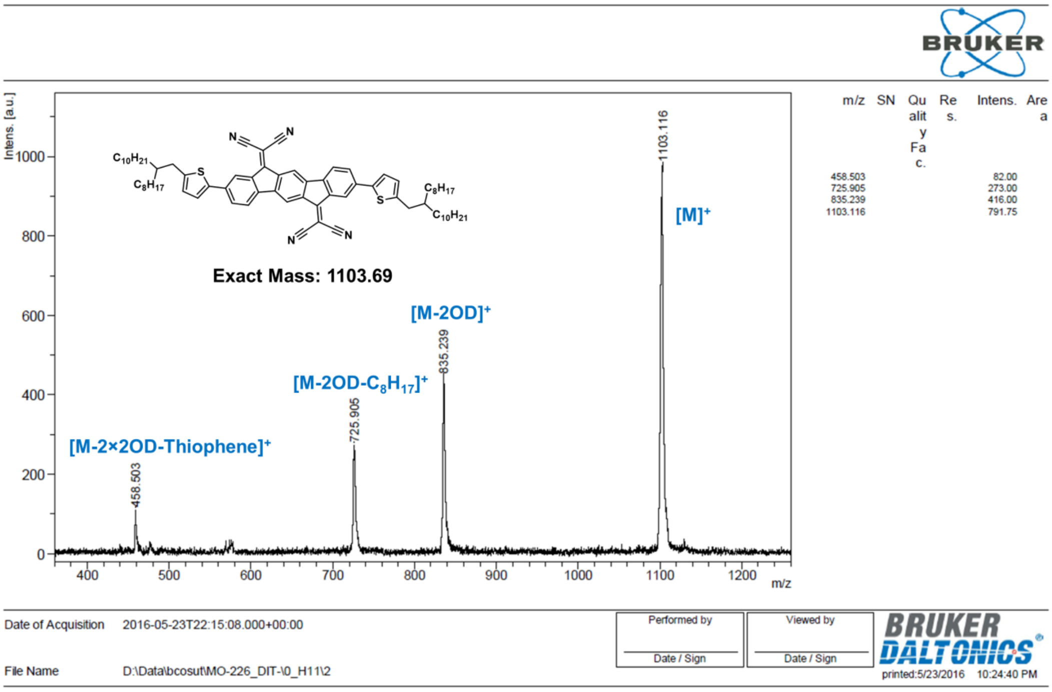

m/z	SN	Quality Fac.	Res.	Intens.	Area
458.503				82.00	
725.905				273.00	
835.239				416.00	
1103.116				791.75	

Date of Acquisition 2016-05-23T22:15:08.000+00:00

File Name D:\Data\bcosut\MO-226_DIT-\0_H11\2

Performed by
Date / Sign

Viewed by
Date / Sign

BRUKER DALTONICS

printed:5/23/2016 10:24:40 PM

Figure 3.2.2.2.3 Positive ion and linear mode MALDI TOF-MS spectrum of α,ω-**2OD-TIFDMT**.

3.2.3 Device Fabrication and Characterization

Top-contact/bottom-gate (TC/BG) OFET devices were fabricated on highly *n*-doped silicon wafers having thermally oxidized 300 nm-SiO_2 dielectric layer (capacitance per unit area (C_i) =11.4 nF/cm^2). The substrates were cleaned by sonication in acetone for 10 min and then treated with oxygen plasma cleaning for 5 min (Harrick plasma, PDC-32G, 18 W). In order to achieve favorable dielectric-semiconductor interface, the dielectric surface was treated with PS (polystyrene)-brush monolayer (M_w = 1.7 – 28 kg/mol) following the reported procedures.[38,47,48] The organic semiconductor layer (**α,ω-2OD-TIFDMT**) was deposited via spin coating on PS-brush-treated gate-dielectric substrates. For the spin-coating process, **α,ω-2OD-TIFDMT** was first dissolved in 1,2,4-trichlorobenzene and the solution was spin-coated with a slow spin rate (300 rpm for 900 sec) to form large crystallites.[37] The solution-processed substrates were annealed in a vacuum oven at different temperatures (50, 100, and 150 °C) for 30 min. The semiconductor film thickness (40-50 nm) was measured by a profilometer (DEKTAK-XT, Brucker). The source-drain electrodes were deposited by thermal evaporation (deposition rate = 0.2 Å/s) as Au layers (50 nm) to yield various channel lengths (L; 100 and 50 μm) and widths (W; 1000 and 500 μm). The electronic performances of the current OFET devices were measured in ambient wih a Keithley 4200-SCS semiconductor characterization system at room temperature. The transistor characteristics in the saturation regime such as charge carrier mobilities (μ) and threshold voltages (V_T) were extracted from the equation:

$$\mu_{sat}= (2I_{DS}L)/[WC_i(V_G - V_T)^2]$$

where I_{DS} is the drain current, L and W are the channel length and width, respectively, C_i is the areal capacitance of the gate dielectric, V_G is the gate voltage, and V_T is the threshold voltage. The surface morphology and out-of-plane crystallinity of semiconductor thin-films were characterized by atomic force microscopy (AFM, NX10, Park systems) and X-ray diffraction (XRD, Smartlab, Rigaku).

3.3 Results and Discussion

3.3.1 Synthesis and Structural/Thermal Characterizations

The synthetic routes to **α,ω-2EH-TIFDMT** and **α,ω-2OD-TIFDMT** are shown in Figure 3.3.1.1, which involves Stille cross-coupling protocols followed by Knoevenagel condensations. The synthesis of the key indeno[1,2-b]fluorene-6,12-dione π-core, **IFDK-Br$_2$**, was previously reported by our group.[6] In the cross-coupling reaction, **IFDK-Br$_2$** was reacted with the corresponding trimethyltin substituted thiophene reagent in the presence of $Pd(PPh_3)_2Cl_2$ catalyst to yield thiophene-indeno[1,2-b]fluorene-6,12-dione-thiophene compounds **1** and **2** in 48% and 34% yields, respectively. For this reaction, the best condition was determined as using highly polar dimethylformamide (DMF) solvent at 125 °C, which partly dissolves **IFDK-Br$_2$** π-core at high temperature for the cross-coupling reaction. Conversion of carbonyl (C=O) groups to dicyanovinylene ($C=C(CN)_2$) on the indeno[1,2-b]fluorene π-cores of **1** and **2** was achieved by double Knoevenagel condensation reaction using excess malononitrile reagent in the presence of $TiCl_4$ Lewis acid and pyridine base. In this reaction, different from typical Knoevenagel condensations, the desired product formation was not observed in the absence of $TiCl_4$ Lewis acid. This indicates that $TiCl_4$ is crucial to the formation of highly electron-deficient indenofluorenebis(dicyanovinylene) (**IFDM**) π-core, and it probably plays a key role in the dehydration step. While **α,ω-2EH-TIFDMT** was found to be an insoluble compound, **α,ω-2OD-TIFDMT** was freely soluble in common nonprotic organic solvents such as chloroform, THF, and toluene, which allowed convenient chromatographic purification and thin-film solution-processing (*vide infra*). This clearly reveals the difference in the lengths of alkyl substituents (2-octyldodecyl *vs* 2-ethylhexyl) on the current D-A-D π-structure. Therefore, only **α,ω-2OD-TIFDMT** was isolated in its pure form as a dark-colored microcrystalline solid in 72% yield.

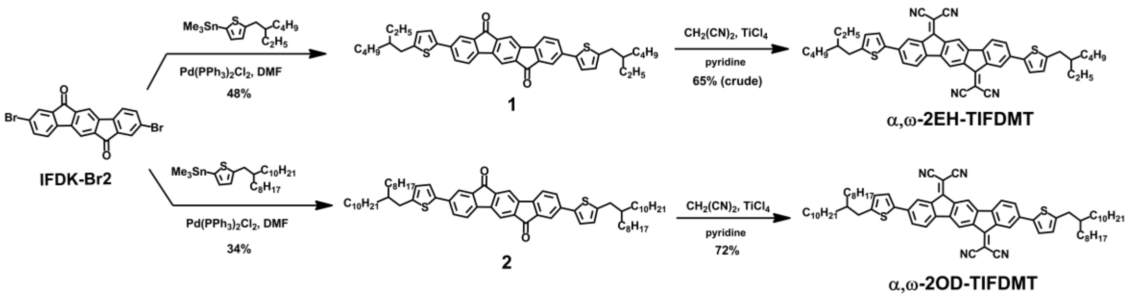

Figure 3.3.1.1 Synthesis of **α,ω-2EH-TIFDMT** and **α,ω-2OD-TIFDMT**.

All the intermediate and the final compounds' chemical structures and purities were characterized by ^{1}H and ^{13}C NMR (Figures 3.2.2.2.1-2), MALDI-TOF (Figure 3.2.2.2.3), elemental analysis, and ATR-FTIR (Figure 3.3.1.2). The ^{1}H-NMR chemical shifts of non-exchangeable aromatic protons for **α,ω-2OD-TIFDMT** were highly dependent on the concentration. As shown in Figure 3.3.1.3, increasing its concentration (from 1 mg/mL to 16 mg/mL) in $CDCl_3$ leads to high-field shifts ($\Delta\delta_{a\text{-}f}$ = 0.1-0.3 ppm) in ^{1}H-NMR spectrum, which arises from shielding effect (ring current effect) of the aromatic units between **α,ω-2OD-TIFDMT** molecules. This indicates the presence of strong self-association between **α,ω-2OD-TIFDMT** molecules in the solution phase. It is noteworthy that based on the chemical shifts measured for the current concentration changes (0.9 mM → 3.6 mM → 14.4 mM), the self-association between **α,ω-2OD-TIFDMT** molecules are expected to be, if not better, as strong as those measured for previously reported macrocyclic π-conjugated systems.[26] This is probably a result of highly favorable intermolecular interactions including donor-acceptor, dipole-dipole and π-π stacking between D-A-D π-cores.

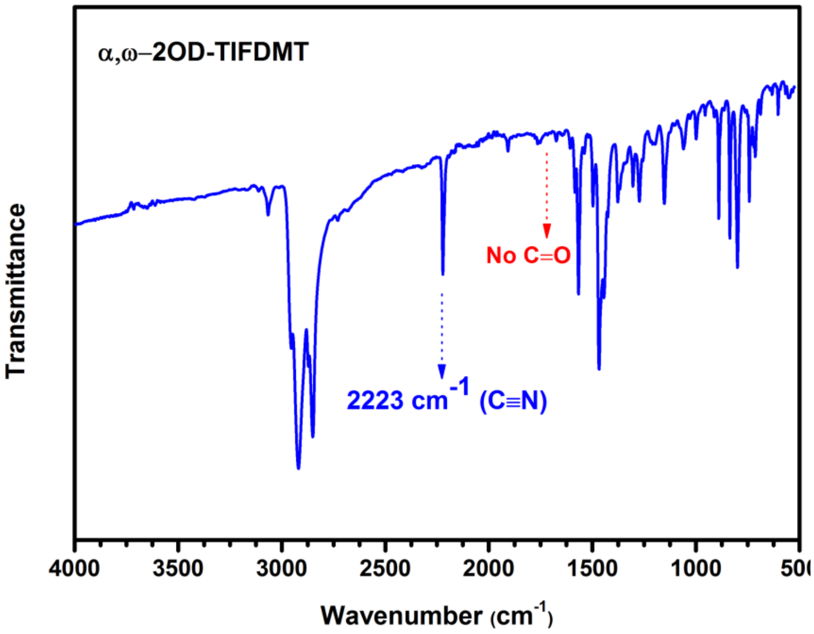

Figure 3.3.1.2 ATR-FTIR Spectra of the semiconductor **α,ω-2OD-TIFDMT** showing C≡N (2223 cm^{-1}) stretching vibrational peak with no C=O (1700 cm^{-1}) peak.

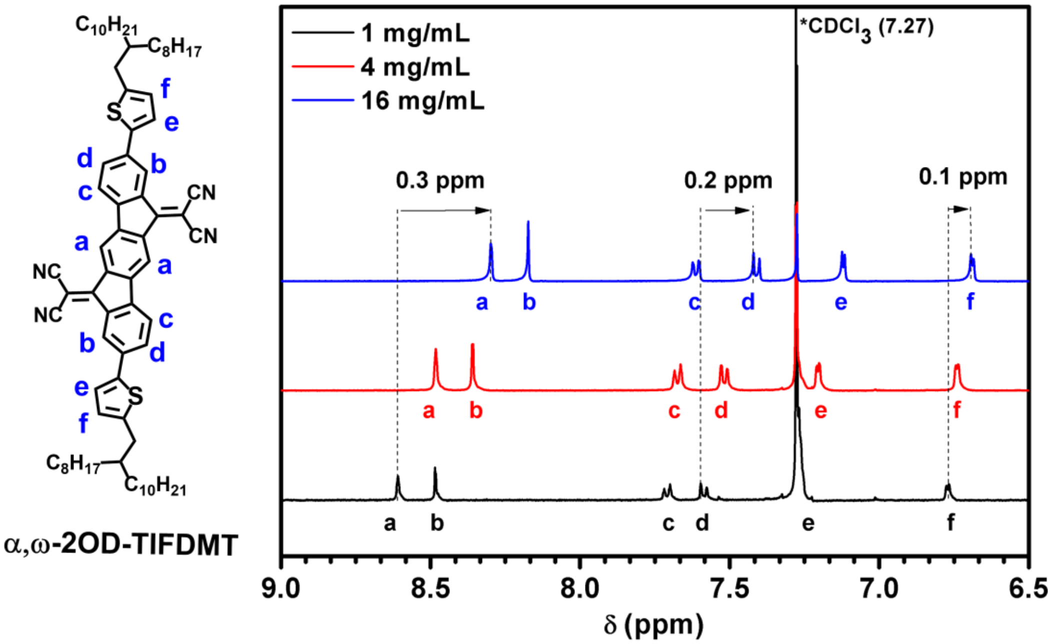

Figure 3.3.1.3 ^{1}H NMR spectra of **α,ω-2OD-TIFDMT** in CDCl$_3$ showing the chemical shifts of aromatic protons (a-f) depending on the concentration.

As shown in Figure 3.3.1.2, ATR-FTIR spectrum of **α,ω-2OD-TIFDMT** shows only “C≡N (2223 cm^{-1})” stretching vibrational peak with no “C=O (1700 cm^{-1})” peak, indicating complete conversion of carbonyl to dicyanovinylene. Thermogravimetric analysis (TGA) of **α,ω-2OD-TIFDMT** shows an excellent thermal stability for the present compound with the thermolysis onset temperature (5% weight loss in TGA, Figure 3.3.1.5-A) of 380 °C. As shown in Figure 3.3.1.5-B, differential scanning calorimetry (DSC) measurement of **α,ω-2OD-TIFDMT** exhibits several sharp endothermic peaks at 85 °C (ΔH= 19.03 J/g), 117 °C (ΔH= 13.74 J/g), and 139 °C (ΔH= 10.06 J/g) prior to the isotropic transition at 232 °C (ΔH= 6.12 J/g). This isotropic transition temperature correlates perfectly with the temperature (230-231 °C) measured with conventional melting measurement. In addition, the observed clearing temperature is in the same range with that of the β-substituted parent compound, **β-DD-TIFDMT** (m.p. 232-233 °C),[27] which indicates that two opposing structural effects are mostly balanced between two semiconductors: the steric bulkiness of the flexible alkyl substituents (2-octyldodecyl > *n*-dodecyl) and the π-rigidity/co-planarity of the molecular backbone (Figure 3.3.1.4, dihedral angle ($\theta_{Ph\text{-}Th}$) = 22°**(α,ω-2OD-TIFDMT)** *vs.* 48°**(β-DD-TIFDMT)**). Upon cooling, two exothermic peaks at 225 °C (ΔH= -5.29 J/g) and 86 °C (ΔH= -12.54 J/g) were recorded. These observed DSC characteristics are indicative of a typical liquid-crystalline (LC) material,[28,29] and **α,ω-2OD-TIFDMT** powder was further examined under a polarized optical microscope (POM) to observe the formation of mesomorphic features as a function of temperature. Typical pseudo focal-conic fan-shaped texture of a hexagonal columnar (Col_h) liquid crystal phase was observed in the second heating cycle when the temperature was raised above 139 °C (Figure 3.3.1.5-C (d)).[30] Therefore, the endothermic peak at 139 °C with an enthalpy of 10.06 J/g is assigned to crystal-to-mesophase transition. The XRD pattern (Figure 3.3.1.6-A) of **α,ω-2OD-TIFDMT** in the LC state further confirms the Col_h phase by showing distinct diffraction peaks ((100), (110), (200), and (210)) corresponding to the lattice parameter of a = 25.81 Å.[31,32] Considering that the total length of **T-IFDM-T** π-core size (18.9 Å, Figure 3.3.1.4) from the energy-minimized molecular geometry and the measured alkyl-chain dimension (4.33 Å) from powder-XRD corresponds to d_{100} in the LC-phase, we propose a possible model for the molecular organization within the columns of **α,ω-2OD-TIFDMT**, which includes the formation of molecular discs by coupling molecular dimers via strong intermolecular interactions (Figure 3.3.1.6-B).[30] In addition, intra-columnar distance of 3.52 Å was measured from the XRD spectra, which corresponds to π-π stacking distances between molecular discs. This indicates the formation of favorable charge-transport network along the column for optoelectronic devices. On the other hand, the earlier DSC peaks at 85 °C and 117 °C did not result in formation of any LC phase (Figure 3.3.1.5-C (a-c)); therefore, they are attributed to crystal-to-crystal transitions.[21] The mesophase (Figure 3.3.1.5-C (d,e)) was found to be stable over a wide temperature range of ~90 °C until the mesophase-to-isotropic liquid (Figure 3.3.1.5-C (f)) transition occurs at 232 °C. In the cooling cycle, mesophase remained stable again over a broad temperature range from 225 °C to 86 °C, which can be attributed to the presence of high degree of molecular ordering as a result of favorable intermolecular interactions (*vide supra*). During the cooling process of the LC phase, another important feature of the current semiconductor was observed that both edge-on (homogeneous) and face-on (homeotropic) molecular alignments exist on the hydrophilic glass substrate.[23] This was clearly evident in the optical images taken on the same substrate during cooling (Figure 3.3.1.7). The presence of peripheral swallow-tailed alkyl substituents (2-octyldodecyl) on the thiophene donor units, which are attached directly to the highly π-rigid **IFDM** acceptor core, makes the current molecular design favorable for columnar liquid crystals. Similar columnar phases have been observed in the literature with alkyl-substituted rod-like π-conjugated molecular systems. [24,30,33]

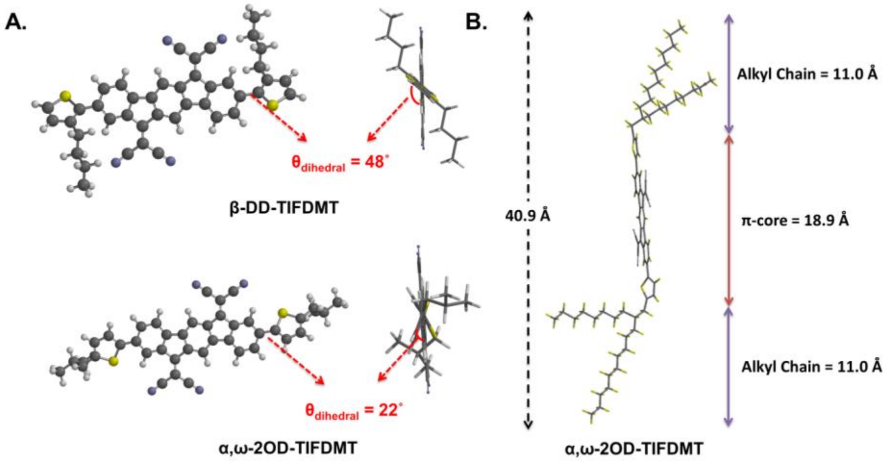

Figure 3.3.1.4 (A) Inter-ring dihedral angles and π-core planarities of **α,ω-2OD-TIFDMT** and **β-DD-TIFDMT** semiconductors. (B) Computed molecular dimensions for **α,ω-2OD-TIFDMT** (DFT, B3LYP/6-31G**).

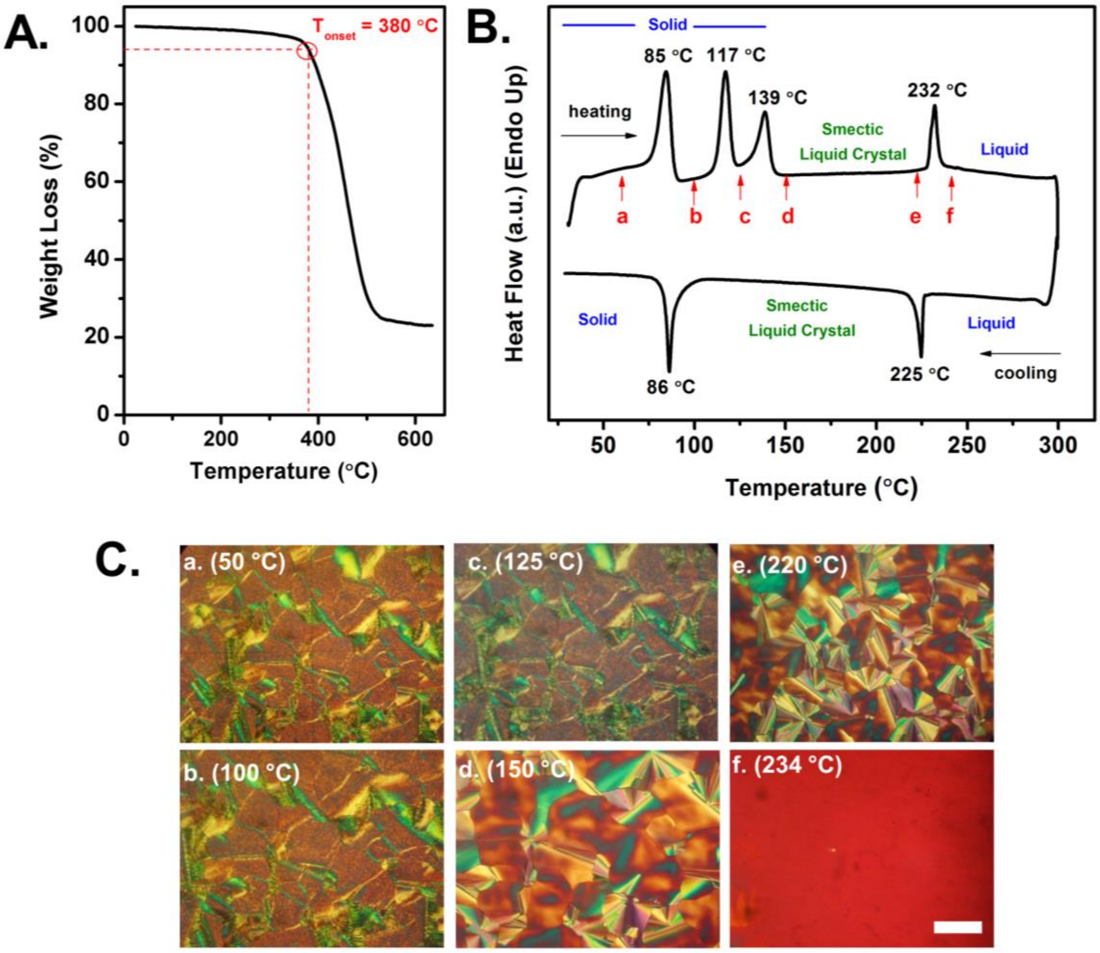

Figure 3.3.1.5 (A) TGA and (B) DSC measurements of **α,ω-2OD-TIFDMT** with heating rate of 10 °C/min under N_2. (C) Optical images taken under 90° cross-polarization conditions as a function of temperature (a-f). Scale bar denotes ~100 µm.

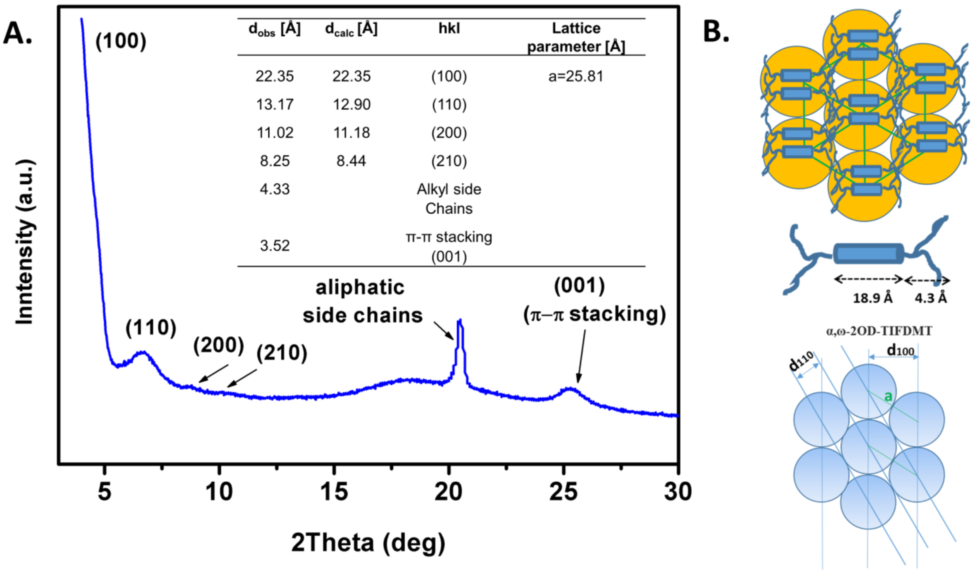

d_{obs} [Å]	d_{calc} [Å]	hkl	Lattice parameter [Å]
22.35	22.35	(100)	a=25.81
13.17	12.90	(110)	
11.02	11.18	(200)	
8.25	8.44	(210)	
4.33		Alkyl side Chains	
3.52		π-π stacking (001)	

Figure 3.3.1.6 (A) X-ray powder diffraction pattern of α,ω-2OD-TIFDMT at 160 °C and d-spacings/lattice parameters indicating a Colh phase. (B) Proposed organization structure of hexagonal columnar phase.

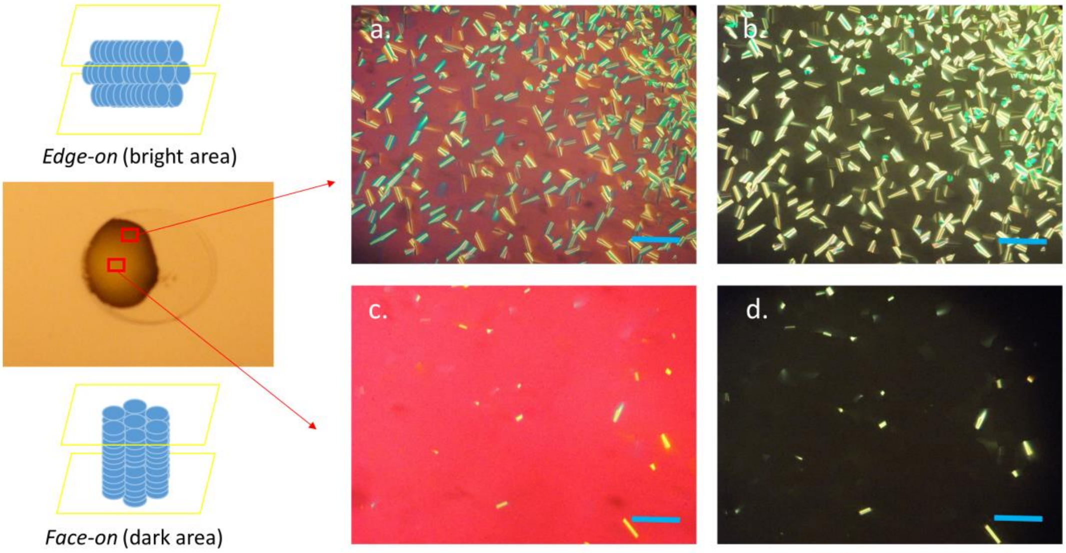

Figure 3.3.1.7 Orientation of α,ω-2OD-TIFDMT upon slow cooling (5 °C/min) from isotropic melt between two glass slides. (a,b) edge-on alignment; (c, d) face-on alignment (b and d without λ retarder plate). Scale bar denotes 100 μm.

3.3.2 Optical and Electrochemical Properties

Molecular electronic structure of **α,ω-2OD-TIFDMT** was evaluated by UV-vis absorption spectroscopy, cyclic voltammetry, and computational modelling (DFT, B3LYP/6-31G**). As shown in Figure 4A, two main absorption peaks are observed in dichloromethane solution at 353 nm and 721 nm, which corresponds to π-π* transition of indeno[1,2-b]fluorene-thiophene backbone and symmetry forbidden n-π* transition of carbonyl groups, respectively.[34] When **α,ω-2OD-TIFDMT** is spin-coated as a thin-film on glass substrate, the absorption maxima are shifted to longer wavelengths by 36-103 nm and vibronic features with peak intervals of 0.15-0.20 eV (aromatic C=C bond stretches) appears. This may reflect molecular π-backbone planarization and intermolecular interaction in the thin-film state as compared to the solution phase. In addition, the optical band gap estimated from the low-energy band edge is lowered from 1.45 eV (in solution) to 1.35 eV (solid-state). Thin-film absorption spectra of **α,ω-2OD-TIFDMT** was found to span a wide spectral range of 300-900 nm, which is consistent with its dark color in the solid-state. Note that this also offers potential for use in photovoltaic applications by harvesting wide spectral range of the solar spectrum.

Electrochemical characterization reveals four reversible reduction peaks (Figure 4B) with the first half-wave potential located at -0.21 V (*vs* Ag/AgCl), which indicates that **α,ω-2OD-TIFDMT** has very stable n-doping/dedoping characteristics with potential electron-transporting nature.

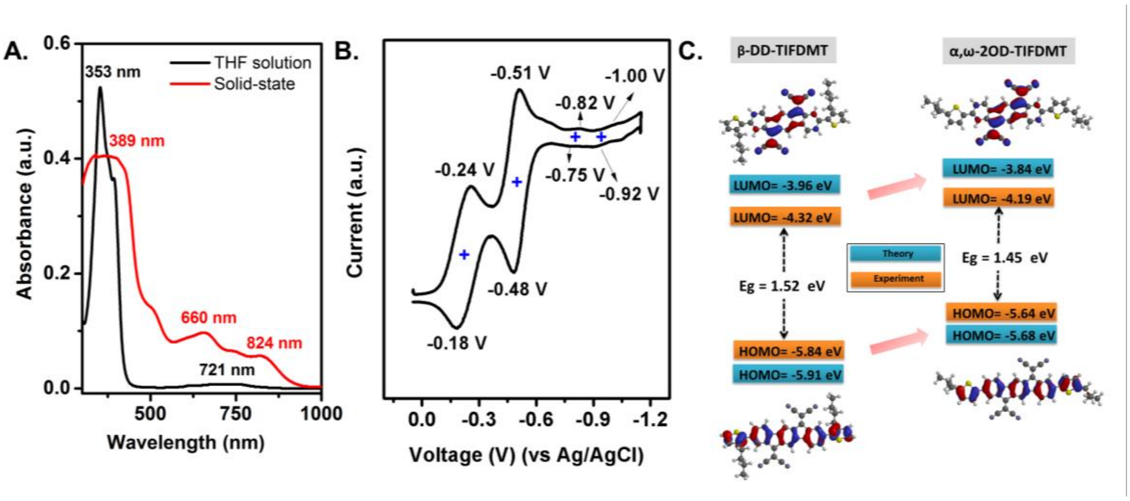

Figure 3.3.2.1 (A) Optical absorption in dichloromethane solution and as thin-films of **α,ω-2OD-TIFDMT**, (B) cyclic voltammogram of **α,ω-2OD-TIFDMT** in dichloromethane (0.1M $Bu_4N^+PF_6^-$, scan rate = 50 $mV\cdot s^{-1}$), and (C) calculated (in blue, DFT, B3LYP/6-31G**) and experimental (in orange) HOMO and LUMO energy levels with topographical orbital representations of **β-DD-TIFDMT**[24] and **α,ω-2OD-TIFDMT**.

The HOMO and LUMO energy levels are estimated as –5.64 eV and -4.19 eV, respectively, which are both higher than those of the reference compound, **β-DD-TIFDMT**.[27] This follows the same trends as the theoretical values (DFT, B3LYP/6-31G**) and is attributed to the repositioning of *β*-substitution to *α,ω*-positions, which enhances the co-planarity of D-A-D π-core (Figure S5, dihedral angle ($\theta_{Ph\text{-}Th}$) = 48° → 22°) and increases HOMO (ΔE = 0.23 eV) and LUMO (ΔE = 0.12 eV) energies with a larger magnitude in the former (Figure 4C). Since HOMO is delocalized over the whole aromatic framework as compared to LUMO, which is localized on the π-acceptor part, co-planarization electronically affects HOMO more than LUMO. The low LUMO energy level of the current semiconductor is in the same range as those of previously reported air-stable *n*-channel semiconductors.[16,35] Furthermore, finely tuned LUMO energy level (increased) and optical band gap (reduced) of **α,ω-2OD-TIFDMT**, as compared to **β-DD-TIFDMT**, can be advantageous for high open-circuit voltage and enhanced solar spectrum absorption when used in bulk-heterojunction solar cells as non-fullerene acceptor.[36]

3.3.3 Field-Effect Transistor Fabrication and Characterization

Based on the good solubility and favorable molecular energetics, field-effect transistors (OFETs) with a top-contact/bottom-gate (TC/BG) device configuration were fabricated by spin-coating semiconductor layer (40-50 nm) under ambient conditions. The spin-coating process was performed by using the semiconductor formulation in a high boiling-point solvent (1,2,4-trichlorobenzene, b.p. = 214 °C) and spinning at a slow spin rate (300 rpm for 900 sec) to form large crystallites.[37] The semiconductor thin-films were thermally annealed at different temperatures (50, 100, and 150 °C) for 30 min before depositing the top source-drain gold electrodes, which was found to have substantial effects on the corresponding OFET performances. Because the semiconductor layer is in direct contact with air in this device geometry, it provides valuable information about intrinsic air-stability of the semiconductor layer during device operation without the help of any encapsulation. Highly *n*-doped Si with a 300 nm thermally grown SiO_2 was used as the "gate-dielectric" platform, and the dielectric surface was functionalized with PS(polystyrene)-brush to reduce surface energy and to induce favorable semiconductor morphology/microstructure at the semiconductor-dielectric interface.[38] All transistors exhibited typical *n*-channel field-effect characteristics in ambient conditions. Representative transfer/output curves are shown in Figure 5. For the devices annealed only at 50 °C, an average electron mobility of 0.07-0.11 $cm^2/V \cdot s$, I_{on}/I_{off} ratio of 10^7-10^8, and threshold voltage of ~19 V are achieved based on 10 individual devices. This indicates a significant improvement in charge-transport performance of the new semiconductor with two orders of magnitude (100×) enhancement in electron mobility, when compared with TC/BG OFETs based on low-temperature (T < 100 °C) annealed **β-DD-TIFDMT** films.[27] The devices are found to be perfectly stable in air reflecting the sufficiently low LUMO energy level of **α,ω-2OD-TIFDMT** that stabilizes charge-transporting electrons against the ambient redox couple (O_2/H_2O).[39] The devices stored in ambient without excluding light showed only a very small degree of degradation in transfer characteristics with less than one order of magnitude decrease in the on-current (I_{on}) after 8 weeks of storage (Figure S8). The excellent stability of the off-current (I_{off} ~10^{-13}-10^{-12} A) indicates negligible chemical doping of the semiconductor film in ambient. This can be ascribed to perfectly balanced LUMO energy level (-4.19 eV) of **α,ω-2OD-TIFDMT**, which is low enough to induce ambient-stability for electron-transport, but at the same time high enough to avoid any undesired chemical doping.[40] The good electron mobility and ambient-stability of the current semiconductor thin-films offer important advantages for **α,ω-2OD-TIFDMT** to be used in p-n junctions, bipolar transistors, and organic complementary-like circuitry (CMOS).[16] As shown in Figure 5A, when the devices are annealed at 100 °C and 150 °C, lower electron mobilites of 0.04-0.06 $cm^2/V{\cdot}s$ (I_{on}/I_{off} = 10^7-10^8) and 2×10^{-5} $cm^2/V{\cdot}s$ (I_{on}/I_{off} = 10^4-10^5) were obtained, respectively. This is in sharp contrast with the OFETs fabricated with the parent semiconductor, **β-DD-TIFDMT**, that thermal annealing of its film gradually increases μ_e from ~10^{-3} $cm^2/V{\cdot}s$ to 0.16 $cm^2/V{\cdot}s$ as a result of microstructural rearrangement and increase in grain size.[27] The observed mobility trend with the new liquid-crystalline semiconductor's OFET performance correlates with the microstructural and morphological changes in thin-film phase as discussed in the next section.

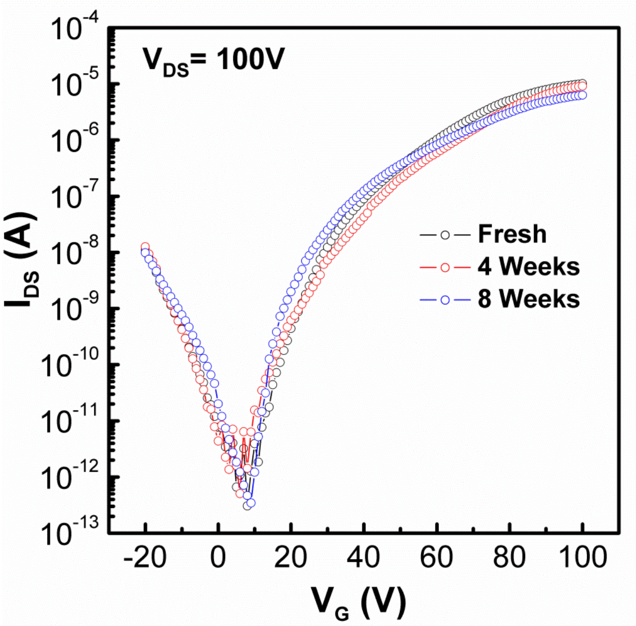

Figure 3.3.3.1 Transfer curves of **α,ω-2OD-TIFDMT**-based OFET devices measured after fabrication (fresh), after 4 weeks (red), and after 8 weeks (blue) of storage in ambient.

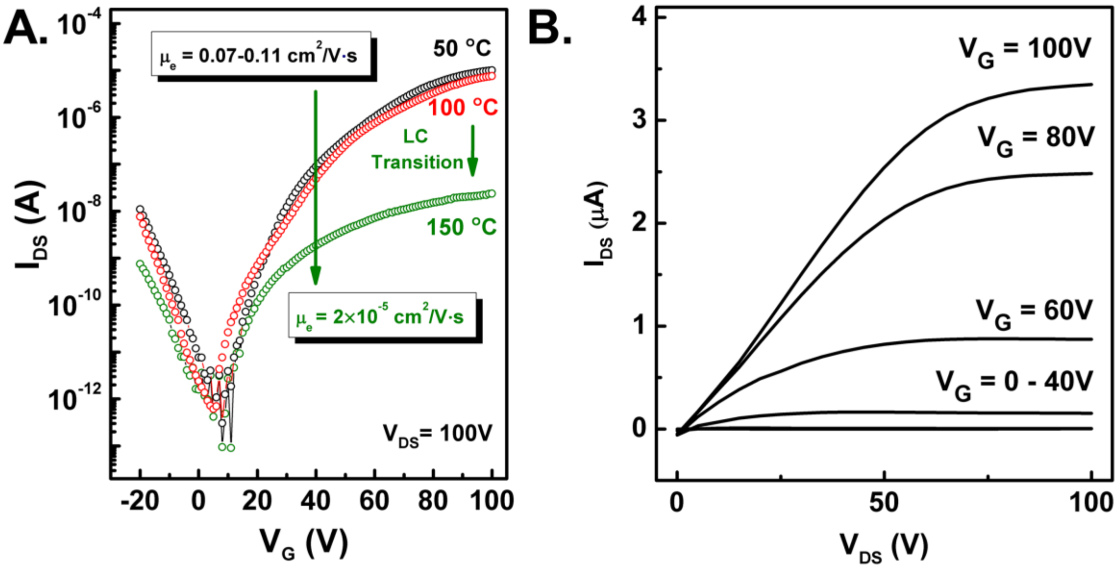

Figure 3.3.3.2 (A) Transfer curves of the top-contact/bottom-gate OFETs on solution-processed thin-films of **α,ω-2OD-TIFDMT** annealed at 50, 100, and 150 °C. (B) Output curve of the OFET devices annealed at 50 °C.

3.3.4 Thin-Film Microstructure and Morphology

Morphological and microstructural characterizations of the semiconductor thin-films were carried out by atomic force microscopy (AFM) and out-of-plane θ-2θ X-ray diffraction (XRD) techniques. As shown in Figure 6A, the thin-films annealed at 50 °C reveals the formation of highly interconnected, micrometer-sized (~0.5-1.0 µm sizes) plate-like grains of terraced islands with step heights of ∼3.9 nm (Figure 7A). This correlates well with the *d*-spacing (3.79 nm) measured along the lamellar layers based on the out-of-plane XRD scan. When the films are annealed at 100 °C, the morphology changed to larger sized (>1.0-2.0 µm) grains with sharp edges and loose interconnectivity (Figure 6B). The step-height profile (Figure 7B) obtained from the AFM image indicates the formation of cracks between crystalline grains as deep as ~25-40 nm, which is almost reaching the surface of the underlying substrate. This temperature is right above the first endothermic transition (85 °C) observed in the DSC scan, and it probably results in molecular rearrangements in the crystalline grains to yield larger grains at the cost of deteriorating interconnectivity. This is also obvious in the XRD scan (Figure 6B) that some additional diffraction peaks appear in the higher angle (7-15°) region, which probably belongs to a secondary crystalline phase. Finally, when the films are annealed at 150 °C in the liquid-crystalline state, the film morphology completely changes to continuous two-dimensional lamellar layers with step-heights of ~3.9 nm (Figure 7C), which uniformly covers a 10×10 μm^2 scan area.

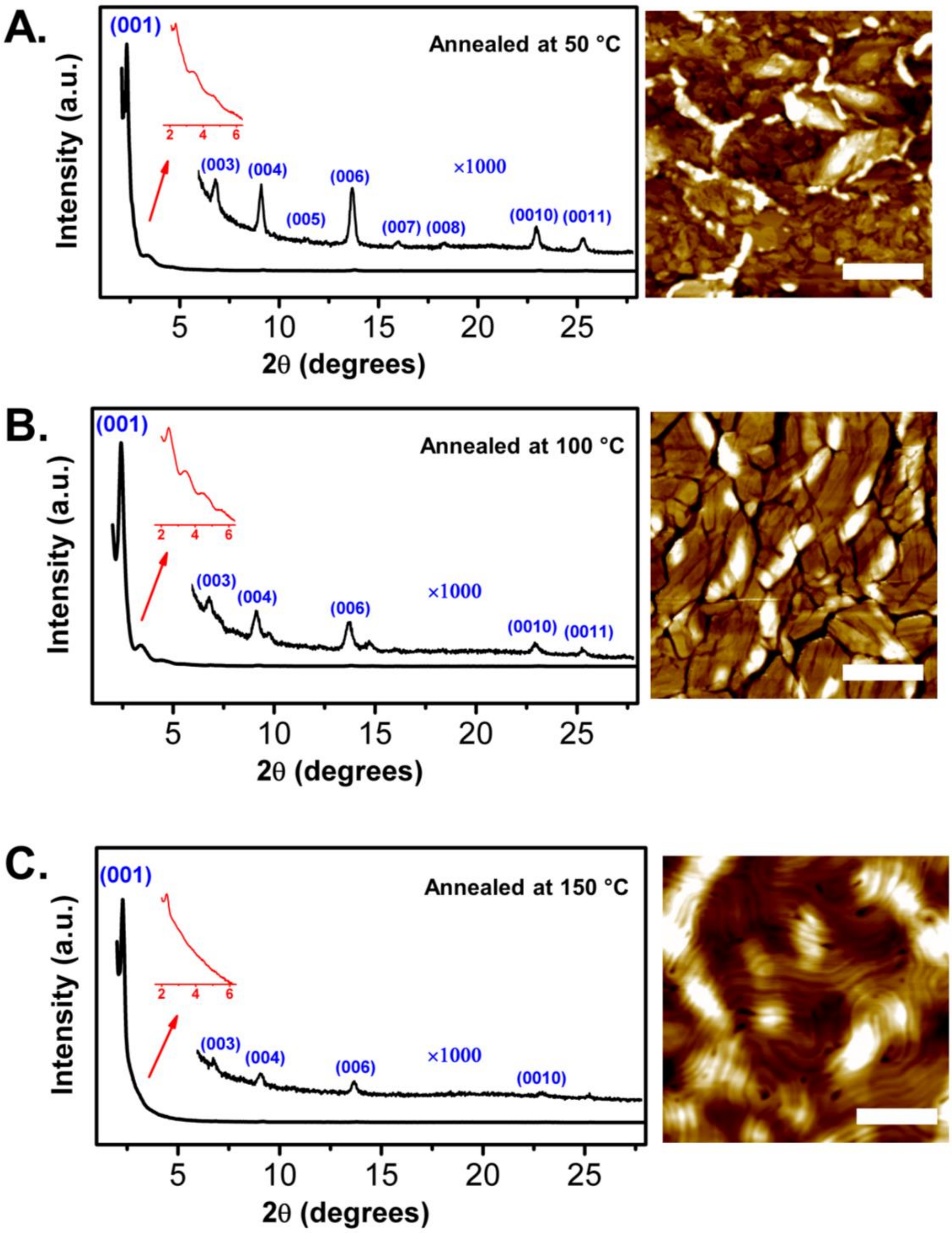

Figure 3.3.4.1 XRD patterns and AFM images of spin-coated **α,ω-2OD-TIFDMT** thin-films annealed at different temperatures: 50 °C (A), 100 °C (B), and 150 °C (C). The scale bar denotes 2.5 μm. The insets depict close-up of the Laue oscillations around the (001) diffraction peak.

θ-2*θ* X-ray diffraction (XRD) characterizations of all thin-films exhibit the formation of highly crystalline texture with a single set of Bragg diffraction peaks up to the eleventh order (00 11). This is indicative of long-range molecular ordering throughout the film thickness in the out-of-plane direction. Based on the first (001) diffractions observed at 2θ = 2.34° (for 50 °C annealing), 2θ = 2.42° (for 100 °C annealing) and 2θ = 2.28° (for 150 °C annealing), lamellar *d*-spacings of 37.9 Å, 36.6 Å, 38.7 Å were measured in the out-of-plane direction, respectively. When these *d*-spacings are compared with the computed (energy minimized geometry by DFT, B3LYP/6-31G**) molecular length (Figure S5B, 40.9 Å) for the fully extended alkyl substituents, it is very likely that, in all thin-films regardless of the annealing temperature, the molecules are mostly adopting edge-on orientation with a small degree of alkyl-chain interdigitation and/or molecular tilting from the substrate normal. For 50 °C and 100 °C annealed thin-films, Laue oscillations were observed around the first-order (001) diffraction peaks indicating that the crystallite spacings are perfectly uniform throughout the thickness of the semiconductor layer.[41] The observed favorable microstructure and morphology of the semiconductor thin-film at 50 °C is a result of strong intermolecular interactions between properly designed molecular structures of **α,ω-2OD-TIFDMT**, and clearly explains the observed good electron mobility in ambient conditions at a relatively low annealing temperature. This clearly explains the two orders of magnitude increase in mobility (100×) compared to **β-DD-TIFDMT**. It is noteworthy that the observed densely packed film morphology should benefit the formation of physical barrier against the diffusion of ambient redox species (O_2 and H_2O), and contribute to device ambient-stability of the current semiconductor thin-films. Although the crystalline grains get larger and molecular edge-on orientation is maintained when the thin-films are annealed at 100 °C, the observed two-fold (2×) decrease in electron mobility should originate from the deterioration in the connectivity of these grains. Finally, it’s very surprising that, despite the favorable lamellar morphology and the crystalline microstructure (with edge-on molecular orientation), extremely low electron mobilities of 2×10^{-5} $cm^2/V\cdot s$ were observed when semiconductor thin-films were annealed at 150 °C. This is in contrast to the mainstream observations with semiconductor thin-films that typically surface morphology and bulk crystallinity well explains the OFET performances. Therefore, it is very likely that **α,ω-2OD-TIFDMT** molecules adopt somewhat different and unfavorable microstructure/morphology in the bottom few layers at the semiconductor-dielectric interface, when compared with those of the bulk thin-film. Although the exact nature of the semiconductor's microstructure/morphology at this interface requires further advanced analysis, it should be related to a molecular orientation remnant from the LC-phase. Note that, for semiconductor thin-films, the charge transport process occurs mostly through the first few molecular layers at the dielectric-semiconductor interface.[42] Considering the significant drop in charge-transport, although the majority of the semiconductor thin-film shows highly ordered "edge-on" orientation, we can speculate that molecules at the interface probably adopt "face-on" orientation. This kind of orientational changes across the semiconductor thin-film has been previously observed in semiconductor films in OFETs[43]. In our case, it's most likely related to completely different crystallization behaviors of the molecules on the hydrophobic self-assembled polymer surface versus in the bulk semiconductor film, while cooling from LC-phase at 150 °C. This difference is caused by the fact that kinetic/thermodynamic parameters (surface energy, nearby electronic/structural properties, dielectric of the medium, etc.) governing the crystallization process are totally different on the hydrophobic self-assembled polymer surface and in the bulk semiconductor film. In the literature, the effect of thermal treatments in the LC phase on the charge-transport properties of the corresponding OFETs has been controversial. [44,45] To this end, our new columnar liquid crystalline semiconductor, **α,ω-2OD-TIFDMT**, shows an important example that thermal annealing at LC-state causes drastic decrease in the electron mobility, which is consistent with some earlier results on similar alkyl substituted small molecules with fused π-conjugated cores.[21]

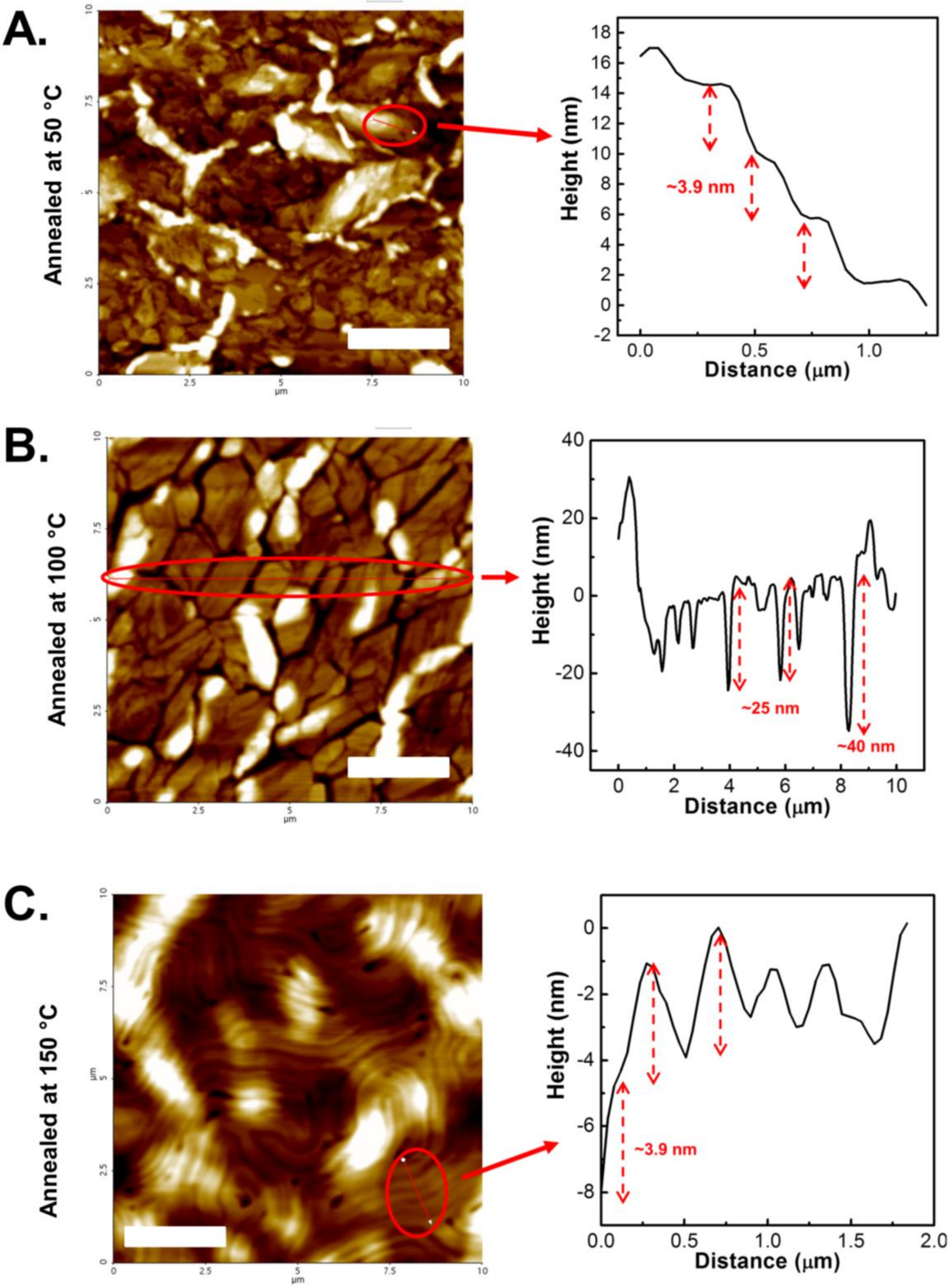

Figure 3.3.4.2 Step-height profiles of terraced or lamellar regions in the AFM topographic images of spin-coated **α,ω-2OD-TIFDMT** thin-films annealed at 50 °C (A), 100 °C (B), and 150 °C (C). The scale bar denotes 2.5 μm.

3.4 Conclusion

We have designed, synthesized and fully characterized a new highly soluble and air-stable liquid-crystalline *n*-channel semiconductor **α,ω-2OD-TIFDMT**, which exhibits a low LUMO energy level of -4.19 eV and a narrow solid-state optical band gap of 1.35 eV. Density functional theory (DFT) calculations clearly explain the electronic and geometric structure trends occurred as a result of repositioning *β*-substituents to *α,ω*-positions. The new semiconductor exhibits excellent thermal stability (T_{onset} = 380 °C) and multiple endothermic transitions with an isotropic transition temperature of 232 °C. Typical pseudo focal-conic fan-shaped texture of a hexagonal columnar liquid crystal phase was observed over a wide temperature range of ~139-232 °C. The thin-films of **α,ω-2OD-TIFDMT** were prepared by a convenient spin-coating process, which forms large (~0.5-1.0 µm sizes) and highly crystalline plate-like grains with good interconnectivity. The microstructure consists of mostly edge-on oriented molecules with π-π stacking interactions along the charge-transport direction. Solution-processed bottom-gate/top-contact (BG/TC) OFETs fabricated with the low-temperature (50 °C) annealed semiconductor film demonstrate good electron mobilities of up to 0.11 $cm^2/V{\cdot}s$ and high I_{on}/I_{off} ratios of 10^7-10^8 with excellent ambient stability. This indicates two orders of magnitude (100×) enhancement in electron mobility for low-temperature annealing, when compared with the reference beta-subtituted semiconductor **β-DD-TIFDMT**. The devices stored in ambient conditions for several weeks exhibited negligible degradation in transfer characteristics while keeping the low I_{off}, which reflects sufficiently low LUMO energy level stabilizing electrons against the ambient redox couple (O_2/H_2O) during charge-transport. Thermal annealing at LC state has yielded much lower (~10^4×) electron mobilities, which was attributed to unfavorable changes in the semiconductor-dielectric interface during cooling from LC phase. The current alkyl chain engineering approach provides crucial structural guidelines for the realization of good carrier mobility at a relatively low annealing temperature for use in OFETs. We believe that the finely tuned optoelectronic and charge-transporting properties of the new semiconductor offer key advantages for use in organic photovoltaics as non-fullerene acceptor material, and further studies are underway. Our findings prove that this new small molecule holds great promise as an air-stable and solution-processable semiconductor for the development of *n*-channel OFETs on low-temperature annealed flexible plastic substrates.

Chapter 4

Conclusions and Future Recommendation

4.1 Conclusions

Novel ambipolar semiconductors yields ultra-low solid-state band gaps of 1.21–1.65 eV with favorable HOMO and LUMO energy levels of -5.47 – -3.61 for 2OD-TTIFDK and -5.49 eV – -4.23 eV for 2OD-TTIFDM, for balanced ambipolarity. Specifically, the sufficiently low LUMO of dicyanovinylene-functionalized molecule, 2OD-TTIFDM, enables ambient-stable electron-transport, while properly aligned HOMO level facilitates hole injection/transport. Top-contact/bottom-gate OFETs fabricated via solution-shearing of 2OD-TTIFDM yield perfectly ambient-stable ambipolar devices with relatively balanced electron and hole mobilities of 0.13 $cm^2/V\cdot s$ and 0.01 $cm^2/V\cdot s$, respectively, and I_{on}/I_{off} ratios of $10^3 – 10^4$. On the other hand, the carbonyl-functionalized molecule, 2OD-TTIFDK, exhibits highly balanced ambipolarity (μ_e/μ_h ~ 2) under vacuum with electron and hole mobilities of 0.02 $cm^2/V\cdot s$ and 0.01 $cm^2/V\cdot s$, respectively and I_{on}/I_{off} ratios of $10^5 – 10^6$. We have also successfully demonstrated the application of the new ambipolar transistors to complementary-like inverters, which is the building block of integrated circuits for data processing. The new inverters exhibit high voltage gains of 30 in ambient for 2OD-TTIFDM and 223 in vacuum for 2OD-TTIFDK. Our findings indicate that ambient stability for ambipolar semiconductors is a function of energetic stabilization via functional group modification, and it is not related to the bulk chemical structure since the π-skeleton stays the same for both small molecules. The theoretical calculations explain the differences in molecular energetics and provide insights into the current functionalization strategies. Our results clearly indicate that IFDM π-core is a proper-sized, favorable acceptor unit for building efficient soluble ambipolar small molecules to operate in ambient. Considering the processing, ambient-stability, charge-transport and inverter characteristics, to the best of our knowledge, the current D-A-D π-structures are among the best performing ambipolar small molecules for OFET and complementary-like inverter devices. Our findings clearly provide a new approach for the preparation of ultra-low band-gap small molecules as ambient-stable and solution-processable ambipolar semiconductors for various organic optoelectronic technologies including CMOS-like integrated circuits.

In novel *n*-type semiconductors case, 2-ethylhexyl substitution was found to be inefficient for required solubility, but 2-octyldodecyl substitution render α,ω-2OD-TIFDMT freely soluble in various solvents at room temperature. α,ω-2OD-TIFDMT was found to exhibit a liquid-crystalline behavior over a broad temperature range (ΔT = 90-130 °C) with a characteristic fan-shaped texture of a hexagonal columnar phase. UV-Vis absorption and cyclic-voltammetry characterizations showed that α,ω-2OD-TIFDMT has low HOMO and LUMO energy levels of -5.64 eV and -4.19 eV, respectively, with a narrow solid-state optical band gap (1.35 eV). The high solubility of α,ω-2OD-TIFDMT, endowed by branched α,ω-alkyl substituents, allows the fabrication of bottom-gate/top-contact OFET devices via spin-coating. The devices, which were annealed only at 50 °C, exhibit perfectly air-stable *n*-channel behavior with good electron mobilities of up to 0.11 $cm^2/V\cdot s$ and I_{on}/I_{off} ratios of 10^7-10^8. This indicates two-orders of magnitude (100×) enhancement in charge-transport, as compared to the OFETs based on low-temperature annealed parent semiconductor (β-DD-TIFDMT) thin-films, which reflects the result of rational alkyl chain engineering. Atomic-force microscopy (AFM) and out-of-plane θ-2θ X-ray diffraction (XRD) characterizations of these thin-films indicate the formation of highly interconnected, micron-sized (~0.5-1.0 µm sizes) plate-like grains with high crystallinity employing edge-on molecular orientations. Four orders of magnitude (10,000×) decrease in electron mobility was observed when semiconductor thin-films were annealed at LC-state, which is attributed to the dielectric-semiconductor interface. These remarkable findings demonstrate that this new small molecule is a promising semiconductor material for the development of *n*-channel OFETs on flexible plastic substrates and LC-state annealing in columnar liquid crystals can be deteriorating for transistor-type charge transport.

4.2 Future Recommendation

For the future works, by using thiazole instead of thiophene or bithiophene donor units, electron mobilities (μ_e) can reach to >1 $cm^2/V\cdot s$. Thiazole offers great advantages when compared with other donor units including, low LUMO energy level, and large dipole moment. Considering all these properties, designing and synthesizing of novel thiazole-based semiconductors looks promising for *n*-channel semiconductors. Moreover, it is very important to better understand relation between structure and property.

Device performances can be optimized by using various device structures (i.e. bottom gate top contact (BG-TC), and top-gate coplanar or staggered) dielectric materials (i.e. Al_2O_3, and Polyvinyl alcohol (PVA)) and film depositing techniques (i.e. solution-shearing, and drop-casting)

Further studies can be performed about microstructural and morphological characteristics of different crystallization behaviors of the molecules on the hydrophobic self-assembled polymer surface versus in the bulk semiconductor film.

BIBLIOGRAPHY

Chapter 1

1 R. F. Pierret, *New York*, 1996, 792.
2 C. Reese and Z. Bao, *Mater. Today*, 2007, **10**, 20–27.
3 J. L. Brédas, D. Beljonne, V. Coropceanu and J. Cornil, *Chem. Rev.*, 2004, **104**, 4971–5003.
4 http://www.bitrebels.com/technology/nokias-awesome-view-on-the-future-nanotech-concept-phone/[the last access: 12-Nov-2016]
5 http://insane.insa-rennes.fr/the-geek-corner-2/flexible-oled-display-the-future-of-mobile-phones/[the last access: 14-Nov-2016]
6 http://www.chemiereport.at/organische-halbleiter-basf-und-rieke-metals-starten
7 H. E. Katz, Z. Bao and S. L. Gilat, *Acc. Chem. Res.*, 2001, **34**, 359–369.
8 L. Zhang, A. Fonari, Y. Liu, A. L. M. Hoyt, H. Lee, D. Granger, S. Parkin, T. P. Russell, J. E. Anthony, J. L. Brédas, V. Coropceanu and A. L. Briseno, *J. Am. Chem. Soc.*, 2014, **136**, 9248–9251.
9 H. Hu, K. Jiang, J.-H. Kim, G. Yang, Z. Li, T. Ma, G. Lu, Y. Qu, H. Ade and H. Yan, *J. Mater. Chem. A*, 2016, **4**, 5039–5043.
10 L. Vaccaro, A. Marrocchi, D. Lanari, S. Santoro and A. Facchetti, *Chem. Sci.*, 2016.
11 Fridman, *J. Polym. Sci. - Polym. Chem. Ed.*, 1974, **12**, 11–20.
12 C. K. Chiang, C. R. Fincher, Y. W. Park, A. J. Heeger, H. Shirakawa, E. J. Louis, S. C. Gau and A. G. MacDiarmid, *Phys. Rev. Lett.*, 1977, **39**, 1098–1101.
13 F. M. Li, A. Nathan, Y. Wu and B. S. Ong, *Organic Thin Film Transistor Integration: A Hybrid Approach*, 2011.
14 C. D. Dimitrakopoulos and P. R. L. Malenfant, *Adv. Mater.*, 2002, **14**, 99–117.
15 M. C. J. M. Vissenberg and M. Matters, *Phys. Rev. B*, 1998, **57**, 13.
16 H. Klauk, *Organic electronics: materials, manufacturing, and applications,* 2006.
17 A. Heeger, A. G. MacDiarmid and H. Shirakawa, *Stock. Sweden R. Swedish Acad. Sci.*, 2000, 1–16.
18 H. Sirringhaus, P. J. Brown, R. H. Friend, M. M. Nielsen, K. Bechgaard, B. M. W. Langeveld-Voss, a. J. H. Spiering, R. a. J. Janssen, E. W. Meijer, P. Herwig and D. M. de Leeuw, *Nature*, 1999, **401**, 685–688.
19 A. Tsumura, H. Koezuka and T. Ando, *Appl. Phys. Lett.*, 1986, **49**, 1210–1212.
20 K. Takimiya, H. Ebata, K. Sakamoto, T. Izawa, T. Otsubo and Y. Kunugi, *J. Am. Chem. Soc.*, 2006, **128**, 12604–12605.
21 T. Lei, J. H. Dou and J. Pei, *Adv. Mater.*, 2012, **24**, 6457–6461.
22 L. Bürgi, M. Turbiez, R. Pfeiffer, F. Bienewald, H. J. Kirner and C. Winnewisser, *Adv. Mater.*, 2008, **20**, 2217–2224.
23 J. Fan, J. D. Yuen, W. Cui, J. Seifter, A. R. Mohebbi, M. Wang, H. Zhou, A.

Heeger and F. Wudl, *Adv. Mater.*, 2012, **24**, 6164–6168.
24 Q. Wu, M. Wang, X. Qiao, Y. Xiong, Y. Huang, X. Gao and H. Li, *Macromolecules*, 2013, **46**, 3887–3894.
25 R. Hajlaoui, G. Horowitz, F. Garnier, A. Arce-Brouchet, L. Laigre, K. A. El, F. Demanze and F. Kouki, *Adv. Mater. (Weinheim, Ger.)*, 1997, **9**, 389–391.
26 A. Dodabalapur, L. Torsi and H. E. Katz, *Science (80-.).*, 1995, **268**, 270–271.
27 M. M. Payne, S. R. Parkin, J. E. Anthony, C. C. Kuo and T. N. Jackson, *J. Am. Chem. Soc.*, 2005, **127**, 4986–4987.
28 H. Ebata, T. Izawa, E. Miyazaki, K. Takimiya, M. Ikeda, H. Kuwabara and T. Yui, *J. Am. Chem. Soc.*, 2007, **129**, 15732–15733.
29 H. Cho, S. Lee, N. S. Cho, G. E. Jabbour, J. Kwak, D. H. Hwang and C. Lee, *ACS Appl. Mater. Interfaces*, 2013, **5**, 3855–3860.
30 A. Dadvand, A. G. Moiseev, K. Sawabe, W. H. Sun, B. Djukic, I. Chung, T. Takenobu, F. Rosei and D. F. Perepichka, *Angew. Chemie - Int. Ed.*, 2012, **51**, 3837–3841.
31 A. Babel and S. A. Jenekhe, *J. Am. Chem. Soc.*, 2003, **125**, 13656–13657.
32 J. A. Letizia, M. R. Salata, C. M. Tribout, A. Facchetti, M. A. Ratner and T. J. Marks, *J. Am. Chem. Soc.*, 2008, **130**, 9679–9694.
33 X. Zhan, Z. Tan, B. Domercq, Z. An, X. Zhang, S. Barlow, Y. Li, D. Zhu, B. Kippelen and S. R. Marder, *J. Am. Chem. Soc.*, 2007, **129**, 7246–7247.
34 Y.-J. Hwang, N. M. Murari and S. a. Jenekhe, *Polym. Chem.*, 2013, **4**, 3187.
35 T. Lei, J. Dou, X. Cao, J. Wang and J. Pei, 2013, 2–5.
36 C. Kanimozhi, N. Yaacobi-Gross, K. W. Chou, A. Amassian, T. D. Anthopoulos and S. Patil, *J. Am. Chem. Soc.*, 2012, **134**, 16532–16535.
37 G. Guillaud, M. Al Sadoun, M. Maitrot, J. Simon and M. Bouvet, *Chem. Phys. Lett.*, 1990, **167**, 503–506.
38 Z. Bao, A. J. Lovinger and J. Brown, 1998, **7863**, 207–208.
39 A. Facchetti, Y. Deng, A. Wang, Y. Koide, H. Sirringhaus, T. J. Marks and R. H. Friend, *Angew. Chemie Int. Ed.*, 2000, **39**, 4547–4551.
40 P. H. Wöbkenberg, D. D. C. Bradley, D. Kronholm, J. C. Hummelen, D. M. de Leeuw, M. Cölle and T. D. Anthopoulos, *Synth. Met.*, 2008, **158**, 468–472.
41 H. E. Katz, J. Johnson, A. J. Lovinger and W. Li, *J. Am. Chem. Soc.*, 2000, **122**, 7787–7792.
42 R. Capelli, S. Toffanin, G. Generali, H. Usta, A. Facchetti and M. Muccini, *Nat. Mater.*, 2010, **9**, 496–503.
43 J. S. Swensen, C. Soci and A. J. Heeger, *Appl. Phys. Lett.*, 2005, **87**, 1–3.
44 G. Generali, F. Dinelli, R. Capelli, S. Toffanin and M. Muccini, *J. Phys. D. Appl. Phys.*, 2011, **44**, 224018.
45 J. Zaumseil, R. H. Friend and H. Sirringhaus, *Nat. Mater.*, 2006, **5**, 69–74.
46 M. Muccini, *Nat. Mater.*, 2006, **5**, 605–613.
47 M. Heeney, W. Zhang, D. J. Crouch, M. L. Chabinyc, S. Gordeyev, R. Hamilton, S. J. Higgins, I. McCulloch, P. J. Skabara, D. Sparrowe and S. Tierney, *Chem. Commun. (Camb).*, 2007, 5061–5063.
48 K. Oyaizu, T. Iwasaki, Y. Tsukahara and E. Tsuchida, *Macromolecules*, 2004, **37**, 1257–1270.
49 F. S. Kim, X. Guo, M. D. Watson and S. A. Jenekhe, *Adv. Mater.*, 2010, **22**, 478–482.
50 T. T. Steckler, X. Zhang, J. Hwang, R. Honeyager, S. Ohira, X.-H. Zhang, A. Grant, S. Ellinger, S. A. Odom, D. Sweat, D. B. Tanner, A. G. Rinzler, S. Barlow, J.-L. Brédas, B. Kippelen, S. R. Marder and J. R. Reynolds, *J. Am.*

Chem. Soc., 2009, **131**, 2824–2826.

51 T. Lei, J. H. Dou, Z. J. Ma, C. H. Yao, C. J. Liu, J. Y. Wang and J. Pei, *J. Am. Chem. Soc.*, 2012, **134**, 20025–20028.

52 J. Fan, J. D. Yuen, M. Wang, J. Seifter, J. H. Seo, A. R. Mohebbi, D. Zakhidov, A. Heeger and F. Wudl, *Adv. Mater.*, 2012, **24**, 2186–2190.

53 J. D. Yuen, J. Fan, J. Seifter, B. Lim, R. Hufschmid, A. J. Heeger and F. Wudl, *J. Am. Chem. Soc.*, 2011, **133**, 20799–20807.

54 M. L. Tang, A. D. Reichardt, N. Miyaki, R. M. Stoltenberg and Z. Bao, *J. Am. Chem. Soc.*, 2008, **130**, 6064–6065.

55 H. Nakanotani, M. Saito, H. Nakamura and C. Adachi, *Appl. Phys. Lett.*, 2009, **95**, 2007–2010.

56 L. Wang, X. Zhang, H. Tian, Y. Lu, Y. Geng and F. Wang, *Chem. Commun. (Camb).*, 2013, **49**, 11272–4.

57 T. Nishinaga, T. Ohmae, K. Aita, M. Takase, M. Iyoda, T. Arai and Y. Kunugi, *Chem. Commun. (Camb).*, 2013, **49**, 5354–6.

58 J. C. Ribierre, S. Watanabe, M. Matsumoto, T. Muto and T. Aoyama, *Appl. Phys. Lett.*, 2010, **96**, 98–101.

59 H. N. Tsao, W. Pisula, Z. Liu, W. Osikowicz, W. R. Salaneck and K. Müllen, *Adv. Mater.*, 2008, **20**, 2715–2719.

Chapter 2

1 K. Zhou, H. Dong, H.-L. Zhang and W. Hu, *Phys. Chem. Chem. Phys.*, 2014, **16**, 22448–57.

2 H. Usta, W. C. Sheets, M. Denti, G. Generali, R. Capelli, S. Lu, X. Yu, M. Muccini and A. Facchetti, *Chem. Mater.*, 2014, **26**, 6542–6556.

3 J. Zaumseil, R. H. Friend and H. Sirringhaus, *Nat. Mater.*, 2006, **5**, 69–74.

4 R. Capelli, S. Toffanin, G. Generali, H. Usta, A. Facchetti and M. Muccini, *Nat. Mater.*, 2010, **9**, 496–503.

5 M. Durso, C. Bettini, A. Zanelli, M. Gazzano, M. G. Lobello, F. De Angelis, V. Biondo, D. Gentili, R. Capelli, M. Cavallini, S. Toffanin, M. Muccini and M. Melucci, *Org. Electron.*, 2013, **14**, 3089–3097.

6 J. Lee, M. Jang, S. Myeon Lee, D. Yoo, T. J. Shin, J. H. Oh and C. Yang, *ACS Appl. Mater. Interfaces*, 2014, **6**, 20390–20399.

7 A. D. Scaccabarozzi and N. Stingelin, *J. Mater. Chem. A*, 2014, **2**, 10818.

8 S. C. Martens, U. Zschieschang, H. Wadepohl, H. Klauk and L. H. Gade, *Chem. - A Eur. J.*, 2012, **18**, 3498–3509.

9 L. Chua, J. Zaumseil, J. Chang, E. C.-W. Ou, P. K.-H. Ho, H. Sirringhaus and R. H. Friend, *Nature*, 2005, **434**, 194–9.

10 K. J. Baeg, J. Kim, D. Khim, M. Caironi, D. Y. Kim, I. K. You, J. R. Quinn, A. Facchetti and Y. Y. Noh, *ACS Appl. Mater. Interfaces*, 2011, **3**, 3205–3214.

11 C. Rost, D. J. Gundlach, S. Karg and W. Rieß, *J. Appl. Phys.*, 2004, **95**, 5782–5787.

12 J. Cornil, J.-L. Brédas, J. Zaumseil and H. Sirringhaus, *Adv. Mater.*, 2007, **19**, 1791–1799.

13 X. Xu, T. Xiao, X. Gu, X. Yang, S. V. Kershaw, N. Zhao, J. Xu and Q. Miao, *ACS Appl. Mater. Interfaces*, 2015, **7**, 28019–28026.

14 S. S. Cheng, P. Y. Huang, M. Ramesh, H. C. Chang, L. M. Chen, C. M. Yeh, C. L. Fung, M. C. Wu, C. C. Liu, C. Kim, H. C. Lin, M. C. Chen and C. W. Chu, *Adv. Funct. Mater.*, 2014, **24**, 2057–2063.

15 J. Zaumseil and H. Sirringhaus, *Chem. Rev.*, 2007, **107**, 1296–1323.

16 R. P. Ortiz, H. Herrera, C. Seoane, J. L. Segura, A. Facchetti and T. J. Marks, *Chem. - A Eur. J.*, 2012, **18**, 532–543.

17 A. Riaño, P. Mayorga Burrezo, M. J. Mancheño, A. Timalsina, J. Smith, A. Facchetti, T. J. Marks, J. T. López Navarrete, J. L. Segura, J. Casado and R. Ponce Ortiz, *J. Mater. Chem. C*, 2014, **2**, 6376–86.

18 J. Lee, A. R. Han, H. Yu, T. J. Shin, C. Yang and J. H. Oh, *J. Am. Chem. Soc.*, 2013, **135**, 9540–9547.

19 J. Li, Y. Zhao, H. S. Tan, Y. Guo, C.-A. Di, G. Yu, Y. Liu, M. Lin, S. H. Lim, Y. Zhou, H. Su and B. S. Ong, *Sci. Rep.*, 2012, **2**, 754.

20 S. Fabiano, H. Usta, R. Forchheimer, X. Crispin, A. Facchetti and M. Berggren, *Adv. Mater.*, 2014, **26**, 7438–7443.

21 I. Meager, M. Nikolka, B. C. Schroeder, C. B. Nielsen, M. Planells, H. Bronstein, J. W. Rumer, D. I. James, R. S. Ashraf, A. Sadhanala, P. Hayoz, J. C. Flores, H. Sirringhaus and I. McCulloch, *Adv. Funct. Mater.*, 2014, **24**, 7109–7115.

22 T. Ma, K. Jiang, S. Chen, H. Hu, H. Lin, Z. Li, J. Zhao, Y. Liu, Y. M. Chang, C. C. Hsiao and H. Yan, *Adv. Energy Mater.*, 2015, **5**, 2–7.

23 V. Figa, C. Chiappara, F. Ferrante, M. P. Casaletto, F. Principato, S. Cataldo, Z. Chen, H. Usta, A. Facchetti and B. Pignataro, *J. Mater. Chem. C*, 2015, **3**, 5985–5994.

24 D. T. Chase, A. G. Fix, S. J. Kang, B. D. Rose, C. D. Weber, Y. Zhong, L. N. Zakharov, M. C. Lonergan, C. Nuckolls and M. M. Haley, *J. Am. Chem. Soc.*, 2012, **134**, 10349–10352.

25 J. Guo, D. Liu, J. Zhang, J. Zhang, Q. Miao and Z. Xie, *Chem. Commun.*, 2015, **51**, 12004–12007.

26 J. Kan, Y. Chen, D. Qi, Y. Liu and J. Jiang, *Adv. Mater.*, 2012, **24**, 1755–1758.

27 H. E. Katz, Z. Bao and S. L. Gilat, *Acc. Chem. Res.*, 2001, **34**, 359–369.

28 L. Zhang, A. Fonari, Y. Liu, A.-L. M. Hoyt, H. Lee, D. Granger, S. Parkin, T. P. Russell, J. E. Anthony, J.-L. Brédas, V. Coropceanu and A. L. Briseno, *J. Am. Chem. Soc.*, 2014, **136**, 9248–9251.

29 H. Hu, K. Jiang, J.-H. Kim, G. Yang, Z. Li, T. Ma, G. Lu, Y. Qu, H. Ade and H. Yan, *J. Mater. Chem. A*, 2016, 5039–5043.

30 L. Vaccaro, A. Marrocchi, D. Lanari, S. Santoro and A. Facchetti, *Chem. Sci.*, 2016.

31 U. Sen, H. Usta, O. Acar, M. Citir, A. Canlier, A. Bozkurt and A. Ata, *Macromol. Chem. Phys.*, 2015, **216**, 106–112.

32 B. Servet, G. Horowitz, S. Ries, O. Lagorsse, P. Alnot, A. Yassar, F. Deloffre, P. Srivastava, R. Hajlaoui, P. Lang and F. Garnier, *Chem. Mater.*, 1994, 1809–1815.

33 S. Allard, M. Forster, B. Souharce, H. Thiem and U. Scherf, *Angew. Chemie - Int. Ed.*, 2008, **47**, 4070–4098.

34 H. Ebata, T. Izawa, E. Miyazaki, K. Takimiya, M. Ikeda, H. Kuwabara and T. Yui, *J. Am. Chem. Soc.*, 2007, **129**, 15732–15733.

35 L. Zhang, N. S. Colella, B. P. Cherniawski, S. C. B. Mannsfeld and A. L. Briseno, *ACS Appl. Mater. Interfaces*, 2014, **6**, 5327–5343.

36 M.-C. Chen, S. Vegiraju, C.-M. Huang, P.-Y. Huang, K. Prabakaran, S. L. Yau, W.-C. Chen, W.-T. Peng, I. Chao, C. Kim and Y.-T. Tao, *J. Mater. Chem. C*, 2014, **2**, 8892–8902.

37 N. D. Treat, J. A. Nekuda Malik, O. Reid, L. Yu, C. G. Shuttle, G. Rumbles, C. J. Hawker, M. L. Chabinyc, P. Smith and N. Stingelin, *Nat. Mater.*, 2013, **12**, 628–633.

38 M. Sawamoto, M. J. Kang, E. Miyazaki, H. Sugino, I. Osaka and K. Takimiya, *ACS Appl. Mater. Interfaces*, 2016, **8**, 3810–3824.

39 P.-Y. Huang, L.-H. Chen, Y.-Y. Chen, W.-J. Chang, J.-J. Wang, K.-H. Lii, J.-Y. Yan, J.-C. Ho, C.-C. Lee, C. Kim and M.-C. Chen, *Chem. - A Eur. J.*, 2013, **19**, 3721–3728.

40 Y. Yuan, G. Giri, A. L. Ayzner, A. P. Zoombelt, S. C. B. Mannsfeld, J. Chen, D. Nordlund, M. F. Toney, J. Huang and Z. Bao, *Nat. Commun.*, 2014, **5**, 3005.

41 J. Li, X. Qiao, Y. Xiong, W. Hong, X. Gao and H. Li, *J. Mater. Chem. C*, 2013, **1**, 5128.

42 R. Ponce Ortiz, H. Herrera, M. J. Mancheño, C. Seoane, J. L. Segura, P. Mayorga Burrezo, J. Casado, J. T. López Navarrete, A. Facchetti and T. J. Marks, *Chem. - A Eur. J.*, 2013, **19**, 12458–12467.

43 L. Wang, X. Zhang, H. Tian, Y. Lu, Y. Geng and F. Wang, *Chem. Commun. (Camb).*, 2013, **49**, 11272–4.

44 J. Bai, Y. Liu, S. Oh, W. Lei, B. Yin, S. Park and Y. Kan, *RSC Adv.*, 2015, **5**, 53412–53418.

45 G. Lin, Y. Qin, J. Zhang, Y.-S. Guan, H. Xu, W. Xu and D. Zhu, *J. Mater. Chem.*

C, 2016, **4**, 4470–4477.

46 Z. Fang, A. A. Eshbaugh and K. S. Schanze, *J. Am. Chem. Soc.*, 2011, **133**, 3063–3069.

47 G. E. Rudebusch, G. L. Espejo, J. L. Zafra, M. Peña-Alvarez, S. N. Spisak, K. Fukuda, Z. Wei, M. Nakano, M. A. Petrukhina, J. Casado and M. M. Haley, *J. Am. Chem. Soc.*, 2016, **138**, 12648–12654.

48 H. Usta, C. Risko, Z. Wang, H. Huang, M. K. Deliomeroglu, A. Zhukhovitskiy, A. Facchetti and T. J. Marks, *J. Am. Chem. Soc.*, 2009, **131**, 5586–5608.

49 M. Ozdemir, D. Choi, G. Kwon, Y. Zorlu, H. Kim, M.-G. Kim, S. Seo, U. Sen, M. Citir, C. Kim and H. Usta, *RSC Adv.*, 2016, **6**, 212–226.

50 D. J. Frisch, M. J.; Trucks, G.W.; Schlegel, H. B.; Scuseria, G. E.; Robb, M. A.; Cheeseman, J. R.; Scalmani, G.; Barone, V.;Mennucci, B.; Petersson, G. A.; Nakatsuji, H.; Caricato, M.; Li, X.; Hratchian, H. P.; Izmaylov, A. F.; Bloino, J.; Zheng, G.; Sonnenber, *Gaussian, Inc. Wallingford CT*, 2009, 2–3.

51 C. Kim, A. Facchetti and T. J. Marks, *Adv. Mater.*, 2007, **19**, 2561–2566.

52 B. Kim, D. Y. Ryu, V. Pryamitsyn and V. Ganesan, *Macromolecules*, 2009, **42**, 7919–7923.

53 S. H. Park, H. S. Lee, J.-D. Kim, D. W. Breiby, E. Kim, Y. D. Park, D. Y. Ryu, D. R. Lee and J. H. Cho, *J. Mater. Chem.*, 2011, **21**, 15580.

54 G. Giri, E. Verploegen, S. C. Mannsfeld, S. Atahan-Evrenk, H. Kim do, S. Y. Lee, H. A. Becerril, A. Aspuru-Guzik, M. F. Toney and Z. Bao, *Nature*, 2011, **480**, 504.

55 D. S. Rampon, F. S. Rodembusch, J. M. F. M. Schneider, I. H. Bechtold, P. F. B. Gonçalves, A. A. Merlo and P. H. Schneider, *J. Mater. Chem.*, 2010, **20**, 715–722.

56 J. Peng, F. Zhai, X. Guo, X. Jiang and Y. Ma, *RSC Adv.*, 2014, **4**, 13078.

57 H. Usta, C. Newman, Z. Chen and A. Facchetti, *Adv. Mater.*, 2012, **24**, 3678–3684.

58 W. W. H. Wong, T. Birendra Singh, D. Vak, W. Pisula, C. Yan, X. Feng, E. L. Williams, K. L. Chan, Q. Mao, D. J. Jones, M. Chang-Qi, K. Müllen, P. Bäuerle and A. B. Holmes, *Adv. Funct. Mater.*, 2010, **20**, 927–928.

59 L. Oldridge, M. Kastler and K. Müllen, *Chem. Commun. (Camb).*, 2006, 885–887.

60 F. Uckert, S. Setayesh and K. Müllen, *Macromolecules*, 1999, **32**, 4519–4524.

61 Y. Diao, B. C.-K. Tee, G. Giri, J. Xu, D. H. Kim, H. a Becerril, R. M. Stoltenberg, T. H. Lee, G. Xue, S. C. B. Mannsfeld and Z. Bao, *Nat. Mater.*, 2013, **12**, 665–71.

62 M. Gsänger, E. Kirchner, M. Stolte, C. Burschka, V. Stepanenko, J. Pflaum and F. Würthner, *J. Am. Chem. Soc.*, 2014, **136**, 2351–2362.

63 T. D. Anthopoulos, G. C. Anyfantis, G. C. Papavassiliou and D. M. De Leeuw, *Appl. Phys. Lett.*, 2007, **90**, 9–12.

64 Y. Zhou, S.-T. Han, P. Sonar, X. Ma, J. Chen, Z. Zheng and V. A. L. Roy, *Sci. Rep.*, 2015, **5**, 9446.

65 S.-H. Lee, D. Khim, Y. Xu, J. Kim, W.-T. Park, D.-Y. Kim and Y.-Y. Noh, *Sci. Rep.*, 2015, **5**, 10407.

66 T. B. Singh, P. Senkarabacak, N. S. Sariciftci, A. Tanda, C. Lackner, R. Hagelauer and G. Horowitz, *Appl. Phys. Lett.*, 2006, **89**, 1–3.

67 T. D. Anthopoulos, D. M. De Leeuw, E. Cantatore, S. Setayesh, E. J. Meijer, C. Tanase, J. C. Hummelen and P. W. M. Blom, *Appl. Phys. Lett.*, 2004, **85**, 4205–4207.

68 J.-Y. Hu, M. Nakano, I. Osaka and K. Takimiya, *J. Mater. Chem. C*, 2015, **3**, 4244–4249.

69 J. Kim, K. J. Baeg, D. Khim, D. T. James, J. S. Kim, B. Lim, J. M. Yun, H. G. Jeong, P. S. K. Amegadze, Y. Y. Noh and D. Y. Kim, *Chem. Mater.*, 2013, **25**, 1572–1583.

70 H. Xu, Y. C. Zhou, X. Y. Zhou, K. Liu, L. Y. Cao, Y. Ai, Z. P. Fan and H. L. Zhang, *Adv. Funct. Mater.*, 2014, **24**, 2907–2915.

71 J. B. Kim, C. Fuentes-Hernandez, S. J. Kim, S. Choi and B. Kippelen, *Org. Electron. physics, Mater. Appl.*, 2010, **11**, 1074–1078.

72 A. L. Patterson, *Phys. Rev.*, 1939, **56**, 978–982.

73 N. S. Colella, L. Zhang, T. McCarthy-Ward, S. C. B. Mannsfeld, H. H. Winter, M. Heeney, J. J. Watkins and A. L. Briseno, *Phys. Chem. Chem. Phys.*, 2014, 3–7.

74 D. Niedzialek, V. Lemaur, D. Dudenko, J. Shu, M. R. Hansen, J. W. Andreasen, W. Pisula, K. Müllen, J. Cornil and D. Beljonne, *Adv. Mater.*, 2013, **25**, 1939–1947.

Chapter 3

1 M. Madru, G. Guillaud, M. A. Sadoun, M. Maitrot, C. Clarisse, M. L. Contellec, J.-J. André and J. Simon, *Chem. Phys. Lett.*, 1987, **142**, 103–105.

2 R. Madru, G. Guillaud, M. Al Sadoun, M. Maitrot, J.-J. André, J. Simon and R. Even, *Chem. Phys. Lett.*, 1988, **145**, 343–346.

3 H. E. Katz, Z. Bao and S. L. Gilat, *Acc. Chem. Res.*, 2001, **34**, 359–369.

4 L. Zhang, A. Fonari, Y. Liu, A. L. M. Hoyt, H. Lee, D. Granger, S. Parkin, T. P. Russell, J. E. Anthony, J. L. Brédas, V. Coropceanu and A. L. Briseno, *J. Am. Chem. Soc.*, 2014, **136**, 9248–9251.

5 M. Ozdemir, D. Choi, G. Kwon, Y. Zorlu, B. Cosut, H. Kim, A. Facchetti, C. Kim and H. Usta, *ACS Appl. Mater. Interfaces*, 2016, **8**, 14077–14087.

6 M. Ozdemir, D. Choi, G. Kwon, Y. Zorlu, H. Kim, M.-G. Kim, S. Seo, U. Sen, M. Citir, C. Kim and H. Usta, *RSC Adv.*, 2016, **6**, 212–226.

7 C. Wang, Y. Qin, Y. Sun, Y. S. Guan, W. Xu and D. Zhu, *ACS Appl. Mater. Interfaces*, 2015, **7**, 15978–15987.

8 V. Figa, C. Chiappara, F. Ferrante, M. P. Casaletto, F. Principato, S. Cataldo, Z. Chen, H. Usta, A. Facchetti and B. Pignataro, *J. Mater. Chem. C*, 2015, **3**, 5985–5994.

9 U. Sen, H. Usta, O. Acar, M. Citir, A. Canlier, A. Bozkurt and A. Ata, *Macromol. Chem. Phys.*, 2015, **216**, 106–112.

10 R. P. Ortiz, H. Herrera, C. Seoane, J. L. Segura, A. Facchetti and T. J. Marks, *Chem. - A Eur. J.*, 2012, **18**, 532–543.

11 W. W. H. Wong, T. Birendra Singh, D. Vak, W. Pisula, C. Yan, X. Feng, E. L. Williams, K. L. Chan, Q. Mao, D. J. Jones, M. Chang-Qi, K. Müllen, P. Bäuerle and A. B. Holmes, *Adv. Funct. Mater.*, 2010, **20**, 927–928.

12 L. Duan, L. Hou, T.-W. Lee, J. Qiao, D. Zhang, G. Dong, L. Wang and Y. Qiu, *J. Mater. Chem.*, 2010, **20**, 6392.

13 H. Usta, W. C. Sheets, M. Denti, G. Generali, R. Capelli, S. Lu, X. Yu, M. Muccini and A. Facchetti, *Chem. Mater.*, 2014, **26**, 6542–6556.

14 J. K. Borchardt, *Mater. Today*, 2004, **7**, 42–46.

15 S. Fabiano, H. Usta, R. Forchheimer, X. Crispin, A. Facchetti and M. Berggren, *Adv. Mater.*, 2014, **26**, 7438–7443.

16 H. Usta, A. Facchetti and T. J. Marks, *Acc. Chem. Res.*, 2011, **44**, 501–510.

17 C. B. Nielsen, S. Holliday, H.-Y. Chen, S. J. Cryer and I. McCulloch, *Acc. Chem. Res.*, 2015, **48**, 2803–2812.

18 N. Azum, L. A. Taib, Y. M. Al Angari, A. M. Asiri, M. Denti, W. Zhao, H. Usta and A. Facchetti, *Thin Solid Films*, 2016, **616**, 320–327.

19 A. Facchetti, M.-H. Yoon, C. L. Stern, H. E. Katz and T. J. Marks, *Angew. Chemie Int. Ed.*, 2003, **42**, 3900–3903.

20 H. Usta, A. Facchetti and T. J. Marks, *J. Am. Chem. Soc.*, 2008, **130**, 8580–8581.

21 W.-L. Liau, T.-H. Lee, J.-T. Chen and C.-S. Hsu, *J. Mater. Chem. C*, 2016, **4**, 2284–2288.

22 Z. Zhao, Z. Wang, Y. Hu, X. Yang, H. Li, X. Gao and D. Zhu, *J. Org. Chem.*, 2013, **78**, 12214–12219.

23 B. R. Kaafarani, *Chem. Mater.*, 2011, **23**, 378–396.

24 M. Funahashi and A. Sonoda, *Phys. Chem. Chem. Phys.*, 2014, **16**, 7754–63.

25 H. Iino, T. Usui and J.-I. Hanna, *Nat. Commun.*, 2015, **6**, 6828.

26 Y. Takaki, R. Ozawa, T. Kajitani, T. Fukushima, M. Mitsui and K. Kobayashi, *Chem. - A Eur. J.*, 2016, **22**, 16760–16764.

27 H. Usta, C. Risko, Z. Wang, H. Huang, M. K. Deliomeroglu, A. Zhukhovitskiy, A. Facchetti and T. J. Marks, *J. Am. Chem. Soc.*, 2009, **131**, 5586–5608.

28 D. S. Rampon, F. S. Rodembusch, J. M. F. M. Schneider, I. H. Bechtold, P. F. B. Gonçalves, A. A. Merlo and P. H. Schneider, *J. Mater. Chem.*, 2010, **20**, 715–722.

29 K. Sun, Z. Xiao, S. Lu, W. Zajaczkowski, W. Pisula, E. Hanssen, J. M. White, R. M. Williamson, J. Subbiah, J. Ouyang, A. B. Holmes, W. W. H. Wong and D. J. Jones, *Nat. Commun.*, 2015, **6**, 6013.

30 S.-J. Yoon, J. H. Kim, K. S. Kim, J. W. Chung, B. Heinrich, F. Mathevet, P. Kim, B. Donnio, A.-J. Attias, D. Kim and S. Y. Park, *Adv. Funct. Mater.*, 2012, **22**, 61–69.

31 H. L. Ni, H. Monobe, P. Hu, B. Q. Wang, Y. Shimizu and K. Q. Zhao, *Liq. Cryst.*, 2013, **40**, 411–420.

32 S. Laschat, A. Baro, N. Steinke, F. Giesselmann, C. Hägele, G. Scalia, R. Judele, E. Kapatsina, S. Sauer, A. Schreivogel and M. Tosoni, *Angew. Chemie - Int. Ed.*, 2007, **46**, 4832–4887.

33 R. K. Gupta, S. K. Pathak, B. Pradhan, D. S. Shankar Rao, S. Krishna Prasad and A. S. Achalkumar, *Soft Matter*, 2015, **11**, 3629–3636.

34 L. Oldridge, M. Kastler and K. Müllen, *Chem. Commun. (Camb).*, 2006, 885–887.

35 A. Riaño, P. Mayorga Burrezo, M. J. Mancheño, A. Timalsina, J. Smith, A. Facchetti, T. J. Marks, J. T. López Navarrete, J. L. Segura, J. Casado and R. Ponce Ortiz, *J. Mater. Chem. C*, 2014, **2**, 6376–86.

36 L. Zhang, N. S. Colella, B. P. Cherniawski, S. C. B. Mannsfeld and A. L. Briseno, 2014, **6**, 5327–5343.

37 K. Wei Chou, H. Ullah Khan, M. R. Niazi, B. Yan, R. Li, M. M. Payne, J. E. Anthony, D.-M. Smilgies and A. Amassian, *J. Mater. Chem. C*, 2014, **2**, 5681.

38 S. H. Park, H. S. Lee, J.-D. Kim, D. W. Breiby, E. Kim, Y. D. Park, D. Y. Ryu, D. R. Lee and J. H. Cho, *J. Mater. Chem.*, 2011, **21**, 15580–15586.

39 H. Usta, C. Newman, Z. Chen and A. Facchetti, *Adv. Mater.*, 2012, **24**, 3678–3684.

40 D. M. de Leeuw, M. M. J. Simenon, A. R. Brown and R. E. F. Einerhand, *Synth. Met.*, 1997, **87**, 53–59.

41 B. A. Jones, A. Facchetti, M. R. Wasielewski and T. J. Marks, 2007, **56**, 15259–15278.

42 H. Zhang, X. Guo, J. Hui, S. Hu, W. Xu and D. Zhu, *Nano Lett.*, 2011, **11**, 4939–4946.

43 G. Kim, S.-J. Kang, G. K. Dutta, Y.-K. Han, T. J. Shin, Y.-Y. Noh and C. Yang, *J. Am. Chem. Soc.*, 2014, **136**, 9477–9483.

44 I. McCulloch, M. Heeney, C. Bailey, K. Genevicius, I. MacDonald, M. Shkunov, D. Sparrowe, S. Tierney, R. Wagner, W. Zhang, M. L. Chabinyc, R. J. Kline, M. D. McGehee and M. F. Toney, *Nat. Mater.*, 2006, **5**, 328–333.

45 S. Sergeyev, W. Pisula and Y. H. Geerts, *Chem. Soc. Rev.*, 2007, **36**, 1902.

46 M. J. Frisch, G. W. Trucks, H. B. Schlegel, G. E. Scuseria, M. A. Robb, J. R. Cheeseman, G. Scalmani, V. Barone, B. Mennucci, G. A. Petersson, H. Nakatsuji, M. Caricato, X. Li, H. P. Hratchian, A. F. Izmaylov, J. Bloino, G. Zheng, J. L. Sonnenberg, M. Hada, M. Ehara, K. Toyota, R. Fukuda, J.

Hasegawa, M. Ishida, T. Nakajima, Y. Honda, O. Kitao, H. Nakai, T. Vreven, J. A. M. Jr, J. E. Peralta, F. Ogliaro, M. Bearpark, J. J. Heyd, E. Brothers, K. N. Kudin, V. N. Staroverov, T. Keith, R. Kobayashi, J. Normand, K. Raghavachari, A. Rendell, J. C. Burant, S. S. Iyengar, J. Tomasi, M. Cossi, N. Rega, J. M. Millam, M. Klene, J. E. Knox, J. B. Cross, V. Bakken, C. Adamo, J. Jaramillo, R. Gomperts, R. E. Stratmann, O. Yazyev, A. J. Austin, R. Cammi, C. Pomelli, J. W. Ochterski, R. L. Martin, K. Morokuma, V. G. Zakrzewski, G. A. Voth, P. Salvador, J. J. Dannenberg, S. Dapprich, A. D. Daniels, O. Farkas, J. B. Foresman, J. V. Ortiz, J. Cioslowski and D. J. Fox, 2010.

47 C. Kim, A. Facchetti and T. J. Marks, *Adv. Mater.*, 2007, **19**, 2561–2566.

48 B. Kim, D. Y. Ryu, V. Pryamitsyn and V. Ganesan, *Macromolecules*, 2009, **42**, 7919–7923.